Monitoring Chloride Dynamics to Unveil Brain Physiology

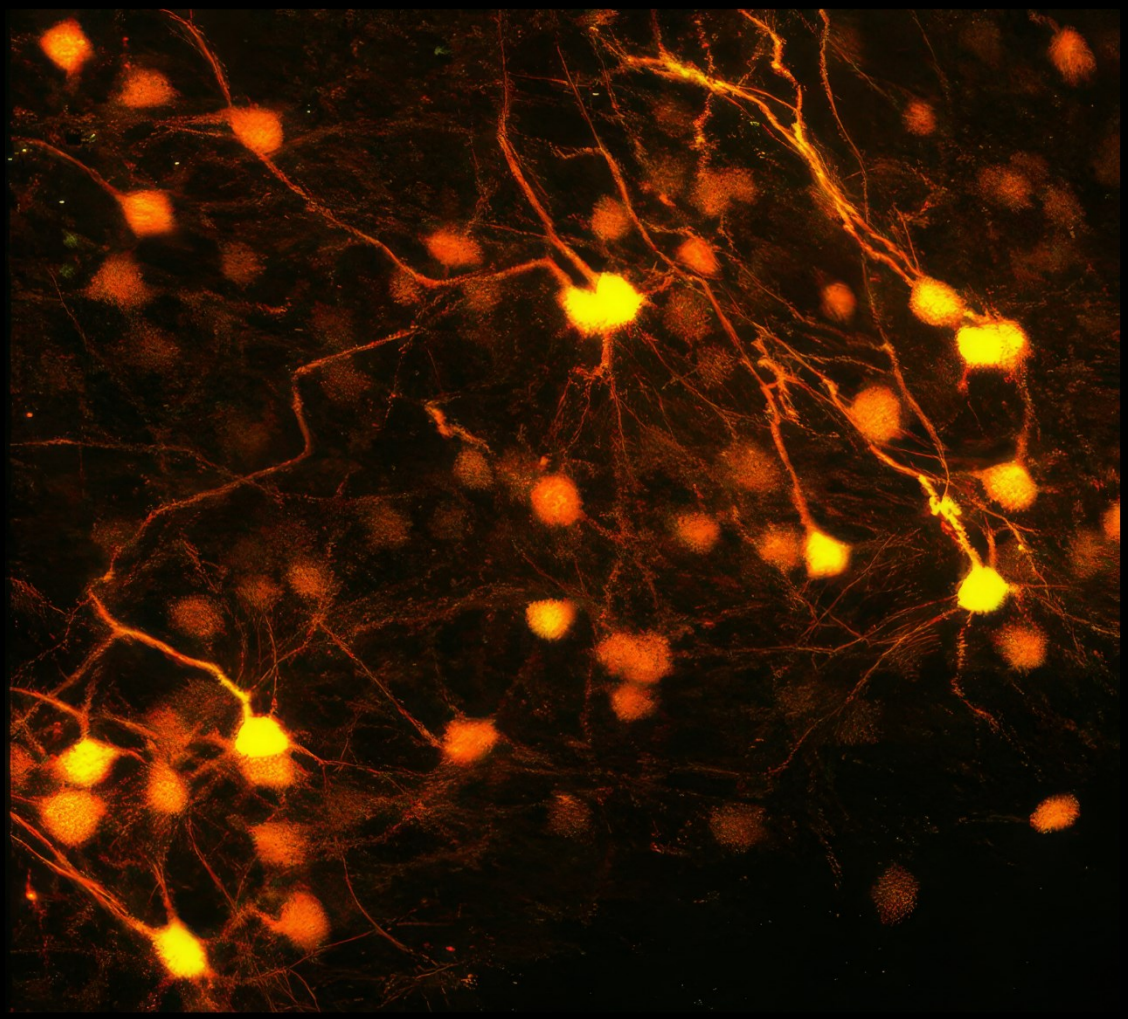

PhD Thesis in Nanoscience —

Biophysics Curriculum

Giacomo Pasquini

SCUOLA
NORMALE
SUPERIORE

SCUOLA
NORMALE
SUPERIORE

Classe di Scienze

Corso di perfezionamento in
Nanoscienze

XXXVII ciclo

Monitoring Chloride Dynamics to Unveil Brain Physiology

Settore Scientifico Disciplinare **BIO/09**

Candidato
dr. Giacomo PASQUINI

Relatori

Prof. Gian Michele Ratto

Dr. Gabriele Nardi

Anno accademico 2024/2025

Table of Contents

1. Abstract

Chloride ions (Cl^-) are key regulators of neuronal excitability and inhibitory signalling. Despite their central role in GABAergic transmission, the mechanisms controlling intracellular chloride concentration ($[Cl^-]_i$) and its temporal dynamics remain poorly understood. This thesis investigates how $[Cl^-]_i$ varies across physiological and behavioural states, how these fluctuations are regulated, and their functional consequences for brain activity.

During my PhD, I focused on improving the quantitative and dynamic measurement of $[Cl^-]_i$ *in vivo*. I first employed LSSmClopHensor, a dual pH/Cl^- fluorescent sensor, to measure absolute changes in neuronal $[Cl^-]_i$ under different conditions. I then contributed to the development and characterization of iClima, a genetically encoded chloride sensor optimized for stable and accurate measurements both *in vitro* and *in vivo*. Compared with previous indicators, iClima exhibits reduced pH sensitivity within the physiological range and enhanced chloride affinity, enabling detection of subtle $[Cl^-]_i$ fluctuations that were previously inaccessible.

Using LSSmClopHensor in combination with electrophysiological recordings and behavioural paradigms, I investigated the mechanisms underlying diurnal $[Cl^-]_i$ fluctuations and their coupling to sleep–wake history. I found that seizure susceptibility follows a diurnal pattern, peaking when intracellular chloride is high, and that reducing $[Cl^-]_i$ prevents seizure occurrence, linking chloride dynamics to network excitability and epileptiform activity. iClima enabled chloride imaging in human cell lines, revealing circadian oscillations of $[Cl^-]_i$ and suggesting that rhythmic ionic regulation is a conserved cellular feature. During epileptic events, iClima captured rapid chloride accumulation and subsequent recovery, providing unprecedented temporal resolution of chloride dynamics. Furthermore, iClima allowed the visualization of physiological chloride responses in cortical pyramidal neurons following visual stimulation and movement, reflecting inhibitory synaptic activity—signals that were undetectable with previous sensors. This represents, to date, the first demonstration of this type.

Together, these results demonstrate that chloride is not merely a passive ion but an active regulator of neuronal physiology. Understanding chloride dynamics is essential to comprehend how cells regulate their function and adapt to changing conditions. iClima represents a major advancement in optical tools for chloride imaging, offering the sensitivity and stability necessary to quantify chloride fluctuations even at subcellular resolution. Yet, the exploration of chloride physiology is still at its dawn: the next generation of optical tools will uncover how this chloride shapes cellular functions, from basic signalling to the brain's electrical and biochemical language.

2. Introduction

2.1 Chloride: a problematic measurement

As the most abundant anion in the body, chloride plays a crucial role in physiology in all cell types. Chloride ion (Cl^-) has extensively been studied as a homeostatic ion. Indeed, the plasma and extracellular Cl^- concentration ($[Cl^-]_o$) maintain body fluid ionic content, volume homeostasis, and blood pressure. $[Cl^-]_{out}$ is, therefore, maintained quite constant, except for some disease states. Unlike $[Cl^-]_o$, intracellular Cl^- concentration ($[Cl^-]_i$) varies considerably between cell types and in response to cell stimulation. Resting $[Cl^-]_i$ in epithelial cells is as high as 60 mM, while in neurons and skeletal muscle, it ranges from 10 mM to 30 mM (Lüscher et al., 2020). While being important for the homeostasis of all the cell types, Cl^- has gained attention largely due to its physiological role in synaptic inhibition in the central nervous system (CNS). As being the main driver of fast synaptic inhibitory responses induced by γ-aminobutyric acid (GABA) and glycine, Cl^- has a role in hyperpolarizing cell, thus affecting the most important biophysical neural feature: their excitability.

Beyond that, the idea that chloride is not only a passive component, but rather a signalling ion is getting relevant in the scientific field (Lüscher et al., 2020). This thought was first developed with the discovery of the direct chloride regulation of the WNK [With No lysine (K)] kinases pathway (Piala et al., 2014). Other observations support this this hypothesis, like the role of chloride in modulating gene expression (Okabe et al., 2003) or its regulation of channel activity (Bekar & Walz, 2002). Besides, the landscape of $[Cl^-]_i$ could be less static than was historically thought. Recent studies highlighted how $[Cl^-]_i$ is highly variegated and continuously changing (Alfonsa et al., 2023; Pracucci et al., 2021). This might be true not only at the level of individual neurons but also within subcellular domains as distinct dendritic branches. The existence of Cl^- microdomains would add a new layer of complexity to dendritic computation. In this scenario, the landscape of $[Cl^-]_i$ can only be evaluated by temporally resolved optical imaging in different cellular compartments (Lodovichi et al., 2022).

For all this reasons, measuring $[Cl^-]_i$ had always been an important goal. Historically, $[Cl^-]_i$ has been assessed with patch clamp. By recording chloride-mediated current under voltage-clamp condition, the chloride reversal potential is determined and used to calculate $[Cl^-]_i$ by using the Nernst equation. Although this technique continues to offer valuable insights in the field, it does have limitations: (a) the estimation of intracellular chloride based on the reversal potential is not entirely accurate, as GABAergic currents also include a bicarbonate component; (b) chloride levels inside the cell can be influenced by the composition of the pipette solution, unless a perforated patch configuration is used. This approach, however, typically involves higher and more variable access resistance; (c) determining the reversal potential of GABAergic currents *in vivo* is highly demanding and technically complex; (d) the technique is limited to a small number of cells and only

under relatively stable, non-dynamic conditions (Arosio & Ratto, 2014). The limited knowledge of specific chloride-binding sites in biological systems initially hindered progress in the study of intracellular chloride dynamics. As a result, early investigations relied on chemical sensors to monitor chloride levels. The discovery that yellow fluorescent protein (YFP) possesses a halide-binding site marked a turning point, enabling the development of genetically encoded chloride indicators and significantly advancing this field. Below, an overview of the main techniques that have been employed over the years to study intracellular chloride is provided.

2.1.1 Chemical sensors

The earliest attempts to monitor $[Cl^-]_i$ relied on synthetic fluorescent dyes, particularly quinolinium-based probes such as SPQ (6-methoxy-N-(3-sulfopropyl)quinolinium) (Illsley & Verkman, 1987), MQAE (N-(ethoxycarbonylmethyl)-6-methoxyquinolinium) (Verkman et al., 1989), and MEQ (6-methoxy-N-ethylquinolinium) (Krapf et al., 1988), a derivative of the fluorophore 6-methoxyquinoline (MQ) (**Figure 1**a). These dyes operate via dynamic collisional quenching: when excited, the fluorophore returns to its ground state through non-radiative energy transfer upon collision with chloride ions, leading to decreased fluorescence intensity in high $[Cl^-]$ environments (Zajac et al., 2020). These indicators were advantageous because they are insensitive to pH and bicarbonate, exhibited rapid kinetics in the microsecond range, and provided direct, real-time fluorescence responses to changes in $[Cl^-]_i$. However, they were also limited by major drawbacks. Primarily, they were non-ratiometric, meaning the fluorescence signal was affected not only by $[Cl^-]_i$ but also by dye loading efficiency making quantitative interpretation difficult (Inglefield & Schwartz-Bloom, 1999). Additional limitations included photobleaching, self-quenching at high dye concentrations (Geddes et al., 2001; Kaneko et al., 2004), and limited membrane permeability, as in the case of MEQ, which required chemical reduction to a permeable form (diHMEQ) prior to cellular uptake (Ashton et al., 2015).

To improve quantitative reliability, efforts were made to develop ratiometric chloride indicators by chemically coupling a Cl^--sensitive part to a Cl^--insensitive reference fluorophore. A foundational example is bis-DMXPQ, which links SPQ to 6-aminoquinolinium (AQ) via a rigid spacer, enabling ratiometric readout (Jayaraman et al., 1999). Similar probes were constructed by pairing MQ with various Cl^--insensitive chromophores, such as aminofluorescein (AF), dansyl (DS), and naphthalic anhydride (NA), providing spectral separation for normalization. Despite this innovation, these ratiometric sensors often suffered from low signal-to-noise ratios, self-quenching, and batch variability, due to challenges in controlling conjugation stoichiometry (Biwersi et al., 1994). To improve this, a more advanced strategy to address these issues was introduced with Clensor, a DNA-based ratiometric indicator that integrates a Cl^--sensitive dye (BAC) on one DNA strand and a reference fluorophore (Alexa Fluor 647) on the complementary strand (**Figure 1**b). This design ensures a defined 1:1 stoichiometry and allows quantitative $[Cl^-]_i$ mapping over the full physiological range (Saha et al., 2015). Of course, the small-molecule conjugates still suffer from photobleaching of the photolabile BAC dye.

However, chemical chloride indicators suffer from important limitations, including the inability to be genetically targeted to specific cell types or subcellular compartments, susceptibility to photobleaching, variability in dye loading and distribution, and, in most cases, the lack of ratiometric readout, which hampers accurate quantification (Arosio & Ratto, 2014).

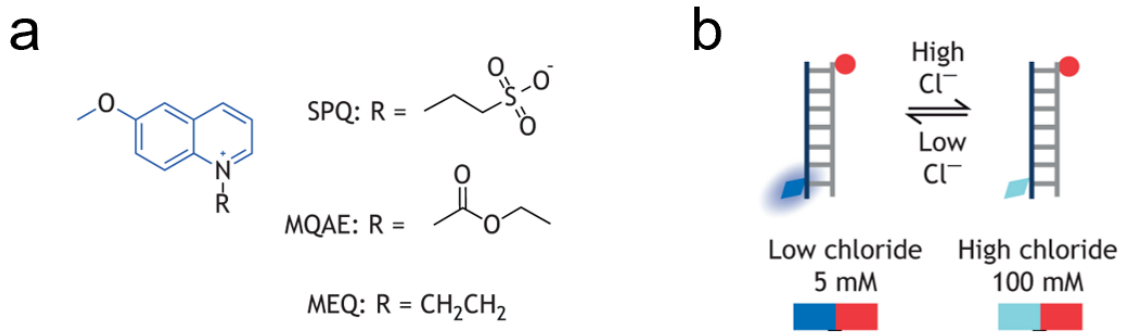

Figure 1: Structure of chemical chloride sensors. a) Examples of small-molecule sensors based on the quinoline core (blue). Ratiometric reporters conjugate the Cl^--sensitive MQ (blue) to a Cl^--insensitive fluorophore (R). **b)** Clensor uses the stoichiometry between complementary nucleic acid strands conjugated to the Cl−-sensitive BAC (blue diamond) and Cl−-insensitive AF647 (red circle) to obtain a ratiometric readout (AF647/BAC, or red/blue). Figure adapted form Zajac et al., 2020.

2.1.2 Genetically encoded sensors

The discovery that the fluorescence of YFP is sensitive to halide ions marked a pivotal moment in chloride imaging. In particular, Wachter & James Remington (1999) observed that YFP's fluorescence was quenched in the presence of chloride and nitrate, opening the way for the development of genetically encoded chloride sensors (GECS) suitable for *in vivo* imaging. The initial sensor was YFP-H148Q, a mutant with improved halide binding due to the introduction of a halide-binding site near the chromophore. This variant significantly increased chloride affinity, lowering the dissociation constant for chloride (K_d) from ~777 mM in wild-type YFP to ~154 mM (Wachter et al., 2000). Further optimization led to YFP-H148Q-I152L, which brought the K_d down to 88 mM, a value approaching the physiological intracellular chloride range (4–60 mM), making it usable for studying chloride dynamics in neurons (Galietta et al., 2001). Although these first-generation indicators were not ratiometric, they offered superior photostability, longer excitation wavelengths, and genetic targetability, allowing for cell-type specific and subcellular localization, clear advantages over small-molecule dyes (Arosio & Ratto, 2014).

A key limitation of early GECS was the lack of a chloride-insensitive reference signal, which made quantification prone to artifacts. This was addressed by the development of Clomeleon, a ratiometric FRET-based sensor composed of cyan fluorescent protein (CFP) as donor and a chloride-sensitive YFP variant ("Topaz") as acceptor, linked by a flexible

peptide (Kuner & Augustine, 2000). Upon chloride binding, YFP fluorescence was quenched, reducing FRET efficiency. The emission ratio of YFP to CFP allowed a ratiometric readout. However, Clomeleon suffers from suboptimal chloride affinity: its K_d ranges from 87 to 167 mM, depending on pH, making it unsuitable for precise quantification in physiological $[Cl^-]_i$ (Kuner & Augustine, 2000). Additionally, it showed a strong dependence on intracellular pH, limiting its utility. To improve this, a library of Clomeleon variants was screened, leading to SuperClomeleon, which showed a markedly better affinity ($K_d \approx 21$ mM at pH 7.1) and improved signal-to-noise ratio thanks to a brighter donor (Cerulean) and optimized linker length (Grimley et al., 2013).

All YFP-based GECS suffer from some degree of pH sensitivity. The chloride binding site is positioned close to the chromophore, and this proximity causes a coupling between chromophore protonation and chloride binding. When the pH is low, the chromophore exists predominantly in its protonated form, which interacts more readily with chloride ions, increasing quenching efficiency. Therefore, the apparent K_d for chloride decreases at lower pH, reflecting this enhanced binding, and rises at higher pH values, where the chromophore is predominantly deprotonated (Arosio & Ratto, 2014; Grimley et al., 2013). For example, SuperClomeleon shows an acid dissociation constant (pK_a) of ~6.4, meaning that even small variations in physiological pH (e.g., from 7.0 to 7.2) can cause substantial errors in $[Cl^-]_i$ estimation. This represents a critical limitation, especially in dynamic physiological or pathological contexts where pH fluctuates (e.g., seizures or ischemia).

To address the issue of pH interference, Arosio et al., (2010) developed ClopHensor, a dual sensor that combines a chloride-sensitive variant of EGFP (E^2GFP-T203Y) with a red chloride- and pH-insensitive reference fluorophore (DsRed-monomer). ClopHensor allows simultaneous measurement of intracellular chloride and pH, using excitation at multiple wavelengths (458, 488, 560 nm) and two emission channels. This configuration provides the ability to internally calibrate K_d values for each measurement based on the pH, thereby distinguishing the Cl^- and pH components. Further improvements led to LSSmClopHensor, where the red fluorophore is replaced by LSSmKate2, a long-Stokes-shift protein. This variant allows better separation of excitation/emission spectra and enhanced performance in two-photon microscopy and in vivo imaging (Paredes et al., 2016).

Recently, turn-on GECS (e.g., phiYFP, lanYFP-derived mNeonGreen) have also emerged. These proteins increase their fluorescence upon Cl^- binding, contrary to traditional quenching-based mechanisms (Clavel et al., 2016; Tutol, Kam, et al., 2019; Tutol, Peng, et al., 2019). While still under development, they may offer higher dynamic range, more robust signal interpretation, together with a slower bleaching rate when low chloride is present. Moreover, continued research in this field could lead to the identification of novel chloride-binding sites, such as the one described in WNK kinases (Piala et al., 2014). These discoveries may inspire the rational design of next-generation chloride sensors with improved specificity and functionality. Efforts also continue to produce sensors with improved pH-independence, subcellular targeting, and response kinetics suitable for monitoring fast Cl^- transients during synaptic activity (Lodovichi et al., 2022).

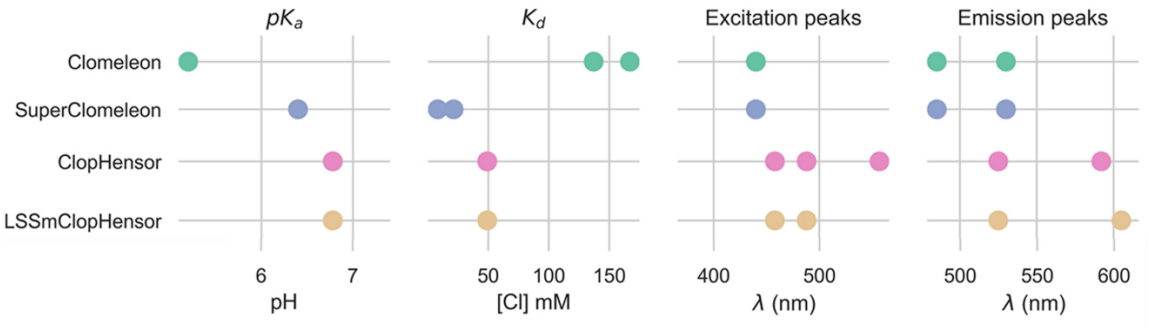

Figure 2: Features of some published GECS. Representation of the properties of ratiometric GECS. Thermodynamic parameters refer to recombinant protein characterization *in vitro*; chloride K_d refers to physiological pH and multiple points indicate multiple published values. The presence of multiple points in the excitation or emission peaks reflects whether the sensor is ratiometric in excitation or emission, or the presence of additional channels for intrinsic pH correction. Adapted from Lodovichi et al., 2022.

2.1.3 LSSmClopHensor

LSSmClopHensor is a genetically encoded sensor of pH and Chloride. It is composed by two fluorescent proteins that are translated together thanks to the presence of a protein-linker sequence (**Figure 3**a). This allows the correct 1:1 stoichiometry of the two proteins thus consenting the ratiometric analysis of the two. The sensor is composed by a chloride sensitive green fluorescent protein, the E^2GFP, and a chloride insensitive red fluorescent protein, the LSSmKate2. The latter's choice was justified by the large distance between excitation and emission maxima that could allow the ratiometric operation using a single excitation wavelength that is optimal for both the green and the red protein (Paredes et al., 2016). However, as described in the previous section, the green fluorescent protein results to be both dependent on pH and Cl^-. In particular, previous studies on E^2GFP have shown that changes in pH affect its excitation spectrum (**Figure 3**b), while chloride ions suppress its fluorescence through a process known as static quenching (**Figure 3**c-d).

The chromophore can be both in a protonated or unprotonated form and, as reported above, this let the chloride K_d depends on pH. LSSmClopHensor was reported to have a pK_a of 6.67 ± 0.05 at 36°C and an apparent K_d of 56.47 mM at pH 7.2.

The protonated and deprotonated forms of the chromophore have a shifted excitation spectrum, and the measured spectrum is the weighted sum of their contributions. The two spectra intersect in the so-called isosbestic point. At that specific wavelength, the excitation coefficients of the two states are equal, and therefore the overall excitation efficiency remains constant regardless of the relative population of the states. Specifically, the protonated form of the E^2GFP chromophore absorbs (and is excited) maximally at 830 nm and the deprotonated form at 960 nm, their excitation spectra intersect at ~910 nm (at 2-photon, **Figure 3**b). At this wavelength the excitation coefficients are identical, and therefore the total excitation is independent of the protonation state. Consequently, the isosbestic point provides a reference that is insensitive to shifts in the protonation equilibrium, making it a powerful internal control in ratiometric sensors. In LSSmClopHensor, performing the imaging at the isosbestic point is the best alternative to minimize the effect of pH shift. Indeed, when a pH shift occurs while imaging at the

isosbestic point, the change in the emitted green fluorescence is just attributable to a shift in the apparent K_d, without the additional change of the shit of the excitation spectrum. Thus, imaging at the isosbestic point enhance the accuracy of quantitative imaging (Arosio et al., 2010).

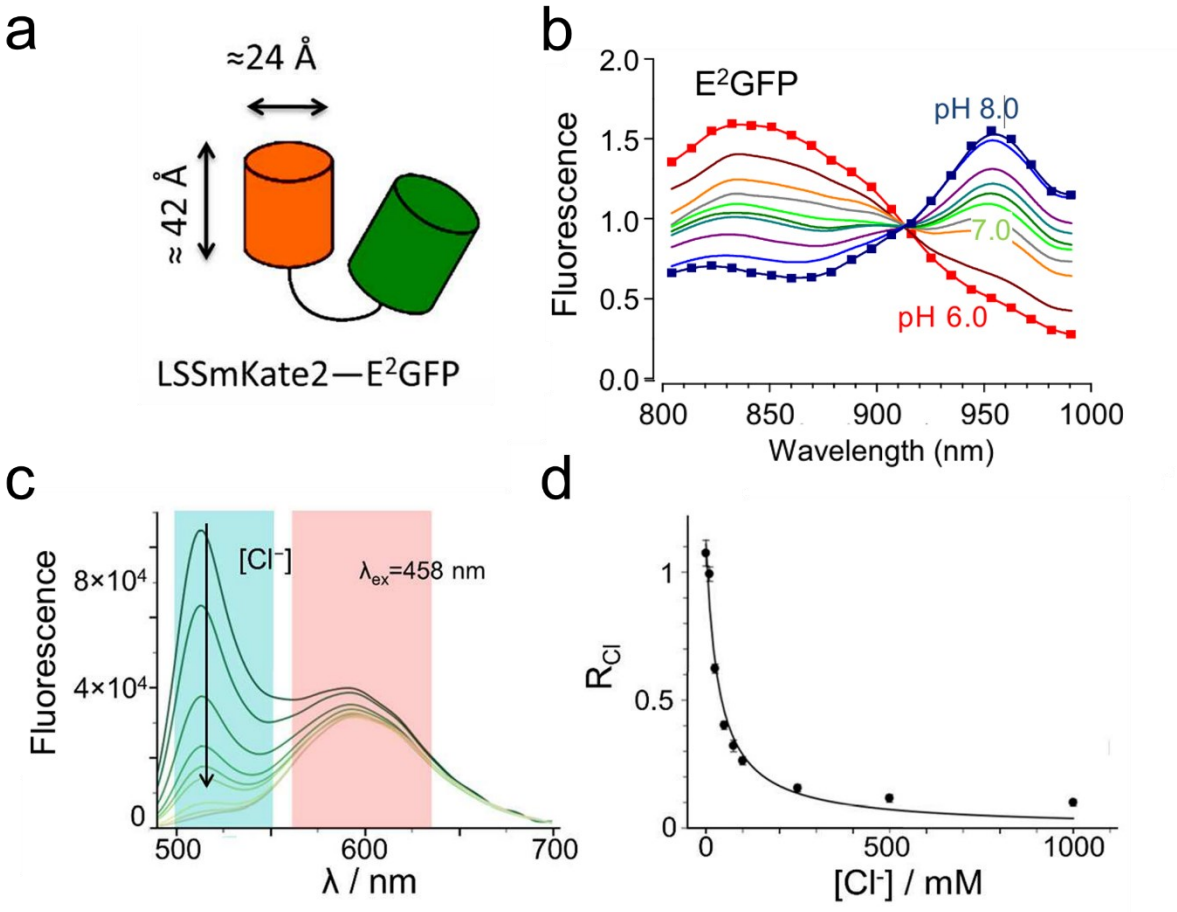

Figure 3: Characteristics of LSSmClopHensor. a) Schematic representation of LSSmClopHensor. **b)** Excitation spectra of the E^2GFP at different levels of pH at 24°C. Data have been corrected for Bleedthrough and normalized using the peak of the LSSmKate2 emission. The non-labelled spectra of E^2GFP have been obtained at pH 6.4, 6.8, 6.9, 7.1, 7.2, 7.4, and 7.6. **c)** LSSmClopHensor emission spectra at the [Cl] values of 0, 10, 25, 50, 75, 100, 250, 500 and 1000 mM; excitation wavelength set at 458 nm, the isosbestic point, pH = 6.5 and temperature at 37°C. The arrow indicates increases in the [Cl]. **d)** Chloride ratio values (green/red) corresponding to the data and spectral ranges reported in c. Figure adapted from Paredes et al., 2016 and Sulis Sato et al., 2017.

2.1.4 Different ways of measuring intracellular chloride

Chloride indicators can be used in two distinct modalities, which differ both in technical demands and in the type of information obtained. The more straightforward approach is to monitor the temporal profile of chloride transients in a semi-quantitative fashion, for instance during neuronal signalling when GABAergic receptors are activated. A more elaborate strategy, however, involves determining the absolute $[Cl^-]_i$. This requires rigorous calibration, in which measured fluorescent signals are compared against

reference datasets obtained across defined ranges of $[Cl^-]_i$ and pH (Lodovichi et al., 2022; Sulis Sato et al., 2017).

2.1.4.1 Measuring chloride relative changes

The most straightforward approach of measuring chloride relative changes is suitable when the main goal is to follow changes in $[Cl^-]_i$ over time, assuming that intracellular pH remains relatively stable. Under these conditions, it is often adequate to measure the relative variation in fluorescence intensity as a function of time. This strategy is very similar to calcium imaging, where transient dynamics are typically expressed as the fractional change in fluorescence relative to the baseline signal (Lodovichi et al., 2022). These measurements result very useful when knowing the exact concentration of the ion is not important. In particular, you can measure at the relative percentage ratio variation compared to the baseline as follows:

(Eq. 1) $$\Delta R/R = \left(\frac{R(t) - R_b}{R_b}\right) \times 100$$

Where R(t) is the Green over Red ratio at each timepoint; and R_b is the Green over Red ratio in the baseline time frame. In particular, $\Delta R/R$ is related to chloride concentration as follows:

(Eq. 2) $$\Delta R/R = -\frac{\Delta Cl}{(Cl + K_{d(pH)})}$$

Meaning that the change in $\Delta R/R$ is proportional to the change in chloride concentration. Thus, $\Delta R/R$ is a semi-quantitative estimate of time- resolved Cl^- changes even if the acquisition system allows only a single excitation wavelength. This remains true just in the case that no changes are expected in intracellular pH, because in this way the only determinant of fluorescence variation would be chloride. This analytical approach may be exploited in a variety of contexts where it is important to evaluate the time course of Cl^- changes by means of confocal microscopy, wide field microscopy or even by means of intravital optic fibers. It is possible that in the future more study will exploit this imaging modality, especially if a pH-insensitive Cl^- sensor will be generated (Lodovichi et al., 2022). Of course, applying this kind of calculation to data acquired at the isosbestic point minimizes the influence of pH changes, even in pH-sensitive sensors because it deletes the influence of pH in the excitation spectra. In this way, only the influence of the apparent K_d on pH remains.

2.1.4.2 Measuring chloride absolute concentration

Measuring absolute chloride concentration was the most used method historically despite being quite time consuming. Calculating absolute chloride values requires rigorous

calibrations, to which we can compare the measured data. This method relies on the fact that chloride sensor of the kind of LSSmClopHensor have a chromophore that can be in two protonated states as follows:

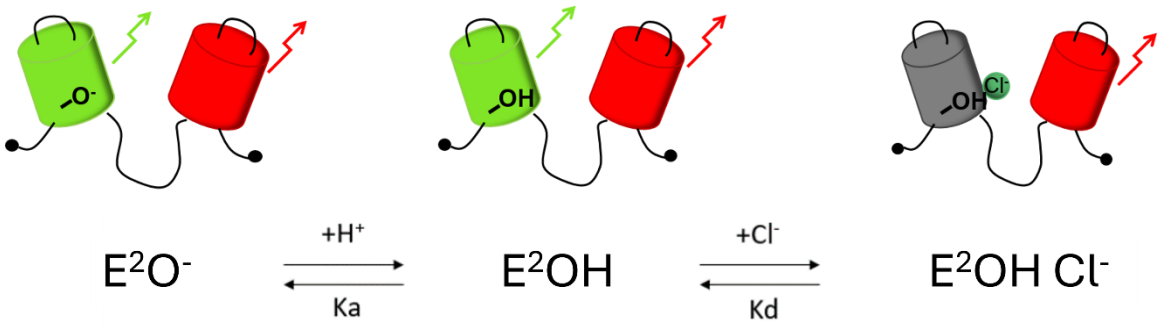

Figure 4: Simplified equilibrium of LSSmClopHensor species. Above, schematic representation of the equilibrium between the possible LSSmClopHensor states. Below, the biochemical equilibrium that is established in presence of protons and Cl^- ions.

Where K_a and K_d are the acidic dissociation constant and the dissociation constant for Cl^- respectively. As reported above, Cl^- can better access its interaction site when the chromophore is protonated. In this way, the apparent chloride K_d depends on pH, because chloride binds only to protonated E^2GFP. Thus, calibrations are crucial to determine the K_a and K_d of the sensor, so that to measure the absolute chloride concentration. Theoretically, one can calculate $[Cl]$ form a sensor of the kind of LSSmClopHensor as in (Sulis Sato et al., 2017), following this equation:

(Eq. 3)
$$[Cl] = K_d^{Cl}(pH)\left(\frac{R_0}{R(Cl)} - 1\right)$$

Where $K_d^{Cl}(pH)$ (often referred as K_d') is the apparent Cl affinity at the cell's pH; R_0 is the ratio between the fluorescence measured in the Green and Red channels in zero chloride when excited at the isosbestic point; and R(Cl) is the fluorescence ratio measured during the experiment. As explained, K_d is the dissociation constant of the protonated form of the sensor, as illustrated by the equilibrium in **Figure 4**. Trivially enough, a single molecule of the sensor can just be in a protonated or unprotonated form. However, while imaging we collect fluorescence from a pool of molecules inside the point spread function (PSF), where the protonated and deprotonated forms of the sensor coexist with proportions depending on the pH and the pK_a. Consequently, within a PSF, a fraction of the sensor molecules will be in the protonated, Cl^--sensitive form, while the remaining fraction will be deprotonated and therefore insensitive to chloride. The overall green fluorescence signal thus represents the sum of two components: the unprotonated (Cl^--insensitive) sensors, which cannot be quenched, and the fraction of protonated, Cl^--sensitive sensors that quenches in the presence of chloride (that is, the basis of K_d the definition). Measuring fluorescence at the isosbestic excitation wavelength, we cannot tell apart the deprotonated from the protonated unquenched species, which both sum up in the green channel. To measure quenching, we compare the green/red fluorescence ratio in presence of Cl^- with the green/red ratio in absence of Cl^-. However, the green signal is

influenced by both protonated and unprotonated species, so that the presence of additional green fluorescence coming from the unprotonated (and therefore unquenchable) form makes the sensor appear less sensitive to chloride. As a result, K_d' (the apparent K_d) that can be measured is shifted toward higher chloride concentrations compared to the true value. Notable, the fraction of deprotonated, non-quenchable protein depends on pH, which is the reason why K_d' is a function on pH. In principle, the true K_d could only be measured under conditions where the pH is extremely lower than the pK_a, so that all the sensor molecules are protonated. $K_d^{Cl}(pH)$ (or K_d') can be defined as follows:

(Eq. 4) $$K_d^{Cl}(pH) = K_d\,(10^{pH-pKa} + 1)$$

Then calculating [Cl] is defined as:

(Eq. 5) $$[Cl] = K_d\,(10^{pH-pKa} + 1)\left(\frac{R_0}{R(Cl)} - 1\right)$$

The equation explains that, in order to calculate the absolute chloride concentration, we need to know the pH of the cells, and few parameters of the sensor: pK_a, K_d and R_0. K_d and the R_0 can be extracted by fitting the R(Cl) obtained during the process of calibrations with the following equation:

(Eq. 6) $$R(\mathrm{Cl}) = \frac{R_0}{1 + \frac{[\mathrm{Cl}]}{K_d}}$$

In practice, obtaining chloride estimates form an experimental data requires to calculate the R(Cl). However, the measured green and red signals cannot be used directly, but they require a series of corrections to account for optical and spectral artifacts that would otherwise bias the measurement. These corrections must be applied in a specific order, which reflects the hierarchy of effects acting on the recorded signal:

1) **Dark subtraction**
   to correct for the baseline offset introduced by the detector's electronic noise. This step removes the background signal measured in the absence of excitation light, ensuring that only the true fluorescence emission contributes to the recorded intensity values.

2) **Detectors gain correction**
   to compensate for variations in the relative sensitivity of the green and red detectors (e.g. photomultiplier tubes) between the day of the experiment and the day of calibrations.

3) **Depth-dependent emission-path extinction correction**
   to correct for scattering and absorption of emitted photons.

4) **Spectral bleed-through (BT) correction**
   to remove signal contamination between channels due to the overlap of the emission spectra and thus the imperfect spectral separation operated by the emission filters.

5) **Compensation for excitation intensity**
   To deal with possible differential excitation intensities of the different excitation wavelengths.

Notably, these corrections are particularly important in the context of *in vivo* experiments, where the tissue introduces strong light scattering and absorption. Without proper correction, the measured R(Cl) would largely reflect these optical artifacts rather than genuine chloride-dependent changes, resulting in inaccurate estimates of intracellular chloride concentration. By contrast, in *in vitro* measurements, such as those performed during calibrations, some corrections may be less critical. For example, emission extinction is minimized, while there is still the need of BT correction (Sulis Sato et al., 2017).

The very first correction that must be applied to the data is the dark subtraction. The baseline offset of the detectors, known as the dark signal, can be estimated by acquiring several frames while the sample is not illuminated, that is, with the laser turned off. For each detector, the average value of these dark frames is calculated, representing the intrinsic noise contribution of the system. This average value is then subtracted from all the subsequent images to remove noise and obtain a more accurate and reliable representation of the actual signal.

After that, the signal needs to compensate for any relative gain change of the photomultiplier tubes (PMTs) between the day of calibration and the day of the experiment. Over time, the relative sensitivity of the two PMTs (green vs. red channel) may drift, which would introduce a systematic error into the ratiometric measurements if left uncorrected. To compensate for this effect, a reference measurement is performed using a uniform solution of a fluorophore with a known and stable emission spectrum, for example Rhodamine 6G at a concentration of 10 µM. A small imaging chamber is filled with this solution, and imaging is performed at a fixed depth (e.g., z=100 µm) under identical excitation and detection settings. This procedure is carried out both on the calibration day and on the experimental day. From each measurement, the ratio of green to red intensities is extracted, and a conversion factor (F_{PMT}) is then defined as:

$$F_{PMT} \stackrel{\text{def}}{=} \frac{(G/R)_{Cal}}{(G/R)_{Exp}}$$

Where $(G/R)_{Cal}$ and $(G/R)_{Exp}$ represent the ratio measured on the calibration and experimental day respectively. F_{PMT} quantifies how much the relative gain of the green channel has changed with respect to the red channel during time. The green signal from the experiment is then corrected as:

$$G^{Corr} = G^{Exp} F_{PMT}$$

For instance, if the green PMT deteriorates faster than the red, F_{PMT} becomes higher than 1, and correct the green experimental value. This correction ensures that all subsequent

analyses are performed on data that are normalized for PMT gain variations, thereby eliminating a significant potential source of systematic error.

Another essential preprocessing step is the correction for emission extinction of the emitted photons. Imaging deeper into the tissue leads to differential attenuation of the detected fluorescence in the two spectral channels, resulting in a systematic distortion of the ratiometric signal. This correction must be applied before bleed-through subtraction, because the relative attenuation of green and red emission with depth would otherwise bias the estimation of cross-talk. The depth dependence needs to be empirically determined, and for our setup it was previously calculated using YFP-expressing neurons as in (Sulis Sato et al., 2017):

$$\gamma(z) = \begin{cases} 1, & z < 32\ \mu m \\ 0.974 + 8.17\ 10^{-4}\ z, & z \geq 32\ \mu m \end{cases}$$

Then, the fluorescence is corrected as:

(Eq. 7) $$G(z) = G^{Corr}(z)\,\gamma(z) \qquad R(z) = R(z)$$

That is, only the green signal is scaled by the depth-dependent factor, while the red signal is left unchanged. The exact coefficients may vary across different optical configurations due to different spectral bandwidths of the emission filters or change when using different objectives.

Fluorescence emitted by one fluorophore (e.g., E^2GFP) is partly detected in the other channel (e.g., red channel) due to overlap of the emission spectra. This artifact is defined as bleed-through and directly affects the signal recorded by the detectors. If we define the channel 1 (Ch1) as the green detection channel, and channel 2 (Ch2) as the red detection channel, the BT coefficients are:

(Eq. 8) $$\alpha \stackrel{\text{def}}{=} \frac{R_{Ch1}}{R_{Ch2}}$$

(Eq. 9) $$\beta \stackrel{\text{def}}{=} \frac{G_{Ch2}}{G_{Ch1}}$$

Where α indicates the amount of red that bleeds through the green channel, and β the amount of green that bleeds through the red channel, while R and G here indicate the fluorescence emitted from the red and green protein, respectively. These two parameters can be experimentally quantified using single-fluorophore controls. Importantly, α and β needs to be re-defined for different setups, as they depend on emission filters and relative gain of the detectors. The overall fluorescence detected will then be:

(Eq. 10) $$\begin{cases} Ch1 = G^* + \alpha R^* \\ Ch2 = \beta G^* + R^* \end{cases}$$

Where G^* indicates the signal due to the photons emitted by the green protein and detected in Ch1, while R^* indicates red emitted photons detected in the Ch2. When *in vivo*

imaging is performed, Ch1 and Ch2 represent the green and red values obtained with Eq.7. Thus, the G^* and R^* are corrected for the BT as follow:

(Eq. 11) $$G^* = \frac{Ch1 - \alpha\, Ch2}{1 + \alpha\beta}$$

(Eq. 12) $$R^* = \frac{Ch2 - \beta\, Ch1}{1 + \alpha\beta}$$

Lastly, the excitation correction needs to be performed. After performing calibrations, the reference excitation spectra of the red protein under controlled conditions was obtained ($S_R^{Cal}(\lambda)$). To correct for depth-dependent excitation scattering in the experimental data and for non-constant excitation intensities, the red excitation spectra recorded on the experimental day ($S_R^{Exp}(\lambda)$) is compared with the calibration spectra, as follows:

(Eq. 13) $$f(\lambda) = \frac{S_R^{Cal}(\lambda)}{S_R^{Exp}(\lambda)}$$

where $f(\lambda)$ being a wavelength-dependent conversion factor. The red spectra is not affected by pH and Cl^-. Thus, any divergence between the red spectra obtained in the experimental day and the calibration day must be caused by a wavelength-dependent loss of excitation. In this way, we can apply the conversion factor to the green and red experimentally obtained spectra as follows:

$$G'(\lambda) = G^*(\lambda)\, f(\lambda)$$

$$R'(\lambda) = R^*(\lambda)\, f(\lambda)$$

It is worth noting that $R^*(\lambda)$ equals $S_R^{Exp}(\lambda)$, thus $R'(\lambda)$ becomes the red spectra of the calibration day (i.e. $S_R^{Cal}(\lambda)$), but the green spectra follows the same kind of correction.

Alternatively, after BT correction, one can rely on the Green/Red spectra for both pH and chloride computation, instead of relying on the individual green and red spectra. This is convenient because the ratio is already intrinsically corrected for excitation intensities.

Only after having applied these corrections, it is possible to fit the pH, and eventually calculate chloride. To determine the intracellular pH, the measured green emission spectrum of each cell is expressed as a linear combination of two reference spectra (acquired during pH calibrations): one at acidic pH (e.g., pH 6, G_{pHa}) and one at basic pH (e.g., pH 8, G_{pHb}). Conceptually, the measured green spectrum ($G'_{pH}(\lambda)$) is fitted to:

(Eq. 14) $$G'_{pH}(\lambda) = \delta\, G_{pHa} + \varepsilon\, G_{pHb}$$

Where δ and ε are the coefficients that minimize the residual error between the measured and reconstructed spectra. Again, instead of green spectra, one can fit the Green/Red spectra as well. The ε and δ coefficients are obtained analytically by solving the linear system defined by the two reference spectra as follows:

$$D = \left(\sum_{\lambda} G_{pHb}^2(\lambda)\right)\left(\sum_{\lambda} G_{pHa}^2(\lambda)\right) - \left(\sum_{\lambda} G_{pHa}(\lambda)G_{pHb}(\lambda)\right)^2$$

$$\varepsilon = \frac{\left(\sum_{\lambda} \mathrm{G}_{\mathrm{pHa}}^2(\lambda)\right)\left(\sum_{\lambda} \mathrm{G}_{\mathrm{pHb}}(\lambda)\mathrm{G}'_{\mathrm{pH}}(\lambda)\right) - \left(\sum_{\lambda} \mathrm{G}_{\mathrm{pHa}}(\lambda)\mathrm{G}_{\mathrm{pHb}}(\lambda)\right)\left(\sum_{\lambda} \mathrm{G}_{\mathrm{pHa}}(\lambda)\mathrm{G}'_{\mathrm{pH}}(\lambda)\right)}{\mathrm{D}}$$

$$\delta = \frac{\sum_{\lambda} \mathrm{G}_{\mathrm{pHa}}(\lambda)\mathrm{G}'_{\mathrm{pH}}(\lambda) - \varepsilon \sum_{\lambda} \mathrm{G}_{\mathrm{pHa}}(\lambda)\mathrm{G}_{\mathrm{pHb}}(\lambda)}{\sum_{\lambda} \mathrm{G}_{\mathrm{pHa}}^2(\lambda)}$$

Note that the larger the number of sampled wavelengths (λ), the more reliable the fit becomes. In fact, the summations over λ can be regarded as discrete approximations of integrals, and therefore a higher spectral resolution improves the accuracy of the reconstruction. Missing intermediate wavelengths can often be interpolated without major issues, but it is crucial not to include wavelengths outside the range used for the calibration. Using spectral regions beyond the calibrated window would introduce systematic errors and compromise the validity of the analysis. Then, the ratio ε/δ is converted to an angle θ as:

$$\theta = \arctan\left(\frac{\varepsilon}{\delta}\right)$$

During the calibration process, excitation spectra at pH_a and pH_b can be obtained. Finding θ during calibration is crucial because it allows to fit a curve with the following free parameters: pK_a, pH_a and pH_b. Thus, the value of pK_a can be obtained with the following equation (unpublished data):

(Eq. 15) $$\theta = \arctan\left(\frac{\varepsilon}{\delta}\right) = arctan\left(-\frac{10^{pHa-pH}-1}{10^{pHb-pH}-1} * \frac{10^{pHb-pKa}+1}{10^{pHa-pKa}+1}\right)$$

Equation 15 can be then rearranged in order to find the pH dependency on θ. This turns extremely useful in the experimental day, when pH needs to be calculated obtaining θ from the experimental data and knowing pK_a:

(Eq. 16) $$pH(\theta) = \log_{10} \frac{\tan\theta\ 10^{pHa+pHb} + \tan\theta\ 10^{pHb+pKa} + 10^{pHa+pHb} + 10^{pHa+pKa}}{10^{pHb} + 10^{pKa} + \tan\theta\ 10^{pKa} + \tan\theta\ 10^{pHa}}$$

After having computed the pH, the chloride measure can finally be obtained by Eq. 5.

2.2 The effect of intracellular chloride concentration in synaptic transmission

GABA is the main inhibitory neurotransmitter of the central nervous system, and its fast action is primarily mediated by the ionotropic $GABA_A$ receptor. In inhibitory synaptic transmission mediated by $GABA_A$, chloride ions play a central and dynamic role. Indeed, while textbooks often present GABA as a stable inhibitory effector in the adult cortex, the

actual effect of $GABA_A$ receptor activation is critically modulated by the chloride gradient across the neuronal membrane. In this section, we focus on how chloride concentration governs both the direction and magnitude of GABAergic currents, and thus the inhibitory (or even paradoxical excitatory) action of GABA.

When GABA binds to the $GABA_A$ receptors, a conductance opens that is permeable to both chloride and bicarbonate ions (HCO_3^-). However, $GABA_A$ is about four times more permeable to Cl^- than to HCO_3^-, meaning that the chloride equilibrium largely determines the net current (Kaila & Voipio, 1987). Thus, knowing the equilibrium potential of chloride (V_{Cl}) is important to evaluate GABA's impact on the cells (Doyon et al., 2016). V_{Cl} can be calculated by Nernst equation as follows:

(Eq. 17) $$V_{Cl} = \frac{RT}{zF} ln \frac{[Cl^-]_o}{[Cl^-]_i}$$

V_{Cl} is expressed in millivolt and depends on universal gas constant R (8.314 JK^{-1} mol^{-1}), on the absolute temperature T (Kelvin), on the ion charge *z*, on the Faraday's constant F (96.500 C mol^{-1}), and on the intracellular and extracellular concentration of the ion, respectively $[Cl^-]_i$ and $[Cl^-]_o$. Changes in $[Cl]_i$ shift V_{Cl} and thereby influence the electrochemical driving force when the $GABA_A$ conductance opens.

The net chloride current (I_{Cl}) generated upon the opening of chloride's conductance is defined as follows:

(Eq. 18) $$I_{Cl} = g_{Cl}(V_m - V_{Cl})$$

The chloride conductance (g_{Cl}) intuitively defines the capability of the cell to allow chloride ions' flux. At the microscopic level, each open $GABA_A$ receptor channel can be modelled as a resistor with resistance r_0, and its corresponding single-channel conductance is therefore $g_0 = 1/r_0$. When N such channels are open simultaneously, they behave electrically as resistors in parallel, resulting in an equivalent total conductance given by:

$$g_{Cl} = N \cdot g_0$$

Thus, the macroscopic chloride conductance (g_{Cl}) is proportional to the number of open $GABA_A$ receptors, linking microscopic channel properties to the overall chloride current measured at the cellular level. V_m represents the membrane potential of the postsynaptic cell. The term $(V_m - V_{Cl})$ is known as the electrochemical driving force and describes the force that will be acting on Cl^- ions after the chloride conductance opening. When V_{Cl} lies below V_m, $GABA_A$ receptor opening generates a positive current. Due to the negative charge owned by the Cl^- ion, a positive current corresponds to an influx of Cl^- ion into the neuron. On the other hand, if V_{Cl} lies above V_m a negative current will be induced, corresponding to an outward chloride flux (Kandel et al., 2021).

V_m and V_{Cl} are the two parameters that influence the direction of chloride currents. Still, V_m of a typical neuron at rest is fixed around -65 mV. Thus, if we want to truly understand GABA's effect, we need to address to V_{Cl}. Noteworthy, V_{Cl} is not a fixed parameter for all

the cells and depends on the intracellular concentration of chloride (Doyon et al., 2016). If $[Cl^-]_i$ is low, this produces a more negative V_{Cl} value. As a result, a higher inward chloride flux of ions is generated, and the cell is hyperpolarized. Thus, low $[Cl^-]_i$ implies cell inhibition mediated by GABA. On the contrary, as $[Cl^-]_i$ increases, V_{Cl} becomes less negative and the driving force will produce an outward chloride current, depolarizing the cell. Thus, GABA induces depolarization in cells with a high chloride load. In literature, it has been reported that the adult pyramidal $[Cl^-]_i$ is usually around 9 mM (Tyzio et al., 2006; Delpire & Staley, 2014). This low $[Cl^-]_i$ fits with the view of GABA as an inhibitory neurotransmitter. However, different pieces of evidence showed $[Cl^-]_i$ in pyramidal neurons is not static but dynamically regulated, thus modulating the strength and polarity of GABAergic signalling. Such variability, even within the inhibitory range, challenges the notion of a fixed inhibitory action of GABA and suggests a more flexible role in tuning neuronal excitability.

2.2.1 NKCC1 and KCC2 regulate neural $[Cl^-]_i$

What does account for the regulation of chloride levels in neurons? Cation-chloride cotransporters (CCCs) play a key role in intracellular Cl^- control (Kaila, 1994). These transmembrane proteins co-transport ions without the generation of any net charge movement exploiting the energy of the cation gradient generated by Na^+/K^+-ATPase. The CCC family is composed of three broad groups: Na^+–Cl^- cotransporters (NCCs), Na^+– K^+– $2Cl^-$ cotransporters (NKCCs) and K^+– Cl^- cotransporters (KCCs) (Payne et al., 2003). Two main cation-chloride cotransporters were identified that tightly controls the chloride gradient across neurons (Ben-Ari, 2002): NKCC1 is a chloride importer that raises $[Cl^-]_i$ and $[K^+]_i$ exploiting the gradient of sodium; KCC2 is instead a chloride extruder that lowers $[Cl^-]_i$ exploiting potassium gradient (**Figure 5**a). KCC1, KCC3 and KCC4 have also been found in the nervous system, with a much more limited expression in neurons (Payne et al., 2003). As NKCC1 and KCC2 are the two main chloride regulators, their activity control is crucial in determining $[Cl^-]_i$. In a “typical” pyramidal neuron NKCC1 would reach equilibrium at relatively high intracellular chloride concentrations (60–70 mM under physiological ionic gradients), thus favouring chloride uptake, whereas KCC2 would equilibrate at low intracellular chloride levels (around 4–5 mM) that promote chloride extrusion (Blaesse et al., 2009; Russell, 2000). Importantly, protein phosphorylation is likely the predominant mechanism by which the dynamic modulation of CCC function takes place (Ben-Ari et al., 2012). Notably, NKCC1 activity is enhanced by phosphorylation of Thr203/Thr207/Thr212 (Flemmer et al., 2002; Zhang et al., 2016). KCC2 activity is enhanced by phosphorylation of Ser940 and inhibited by phosphorylation of Thr1007 (Lee et al., 2007; Leonzino et al., 2016; Rinehart et al., 2009).

The activity of the chloride cotransporters NKCC1 and KCC2 is tightly regulated by the with-no-lysine kinase (WNK) signalling cascade, which acts as a central sensor and modulator of neuronal ionic homeostasis. WNK kinases are sensitive to intracellular chloride concentration and regulate cation-chloride cotransporters through phosphorylation cascades involving the downstream kinases SPAK and OSR1 (Piala et al., 2014). When intracellular chloride level is low, WNK1 and WNK3 become activated through autophosphorylation and subsequently phosphorylate SPAK and OSR1, which in

turn phosphorylate NKCC1 in Thr203/Thr207/Thr212 and KCC2 in Thr906 and Thr1007. This results in activation of NKCC1 and inhibition of KCC2, leading to a net chloride influx and an increase in intracellular chloride concentration (**Figure 5**b. Rinehart et al., 2009). Moreover, a recent work revealed that WNK1 senses Cl^- driven by inhibitory synaptic activity in mature neurons and rapidly modulates KCC2. Activation of $GABA_A$ receptors, which transiently increases intracellular chloride, confines KCC2 at the plasma membrane, whereas blockade of inhibitory transmission decreases $[Cl^-]_i$ and enhances WNK1-mediated phosphorylation of KCC2, promoting its internalization. This mechanism provides a rapid homeostatic feedback loop by which GABAergic transmission dynamically adjusts neuronal chloride gradients and thereby the polarity and strength of inhibitory signalling (Heubl et al., 2017).

At a broader cellular level, WNK kinases also act as sensors of molecular crowding and cell volume. Under hypertonic stress, WNK1 rapidly forms liquid-like condensates that activate the WNK–SPAK/OSR1 pathway, leading to differential regulation of CCCs: NKCC1 is phosphorylated and activated, whereas KCCs are phosphorylated and inhibited. These coordinated changes promote a net influx of Na^+, K^+, and Cl^- ions, driving osmotic water entry and restoring cell volume through the regulatory volume increase mechanism, a process that maintains both cell integrity and ionic homeostasis (Boyd-Shiwarski et al., 2022). Together, these findings establish the WNK–SPAK/OSR1 pathway as a fundamental signalling module that integrates cell volume, intracellular chloride concentration, and synaptic activity to finely tune the balance between NKCC1 and KCC2 function, maintaining chloride homeostasis and inhibitory neurotransmission in neurons

Pharmacological approaches allow us to modulate the activity of these transporters. In particular, furosemide and bumetanide inhibit NKCC and KCC. While furosemide has about equal potency for both NKCC and KCC, bumetanide has ~500-fold greater affinity for NKCC than for KCC, and therefore low concentrations of bumetanide can be used to inhibit NKCC quite selectively (Payne et al., 2003).

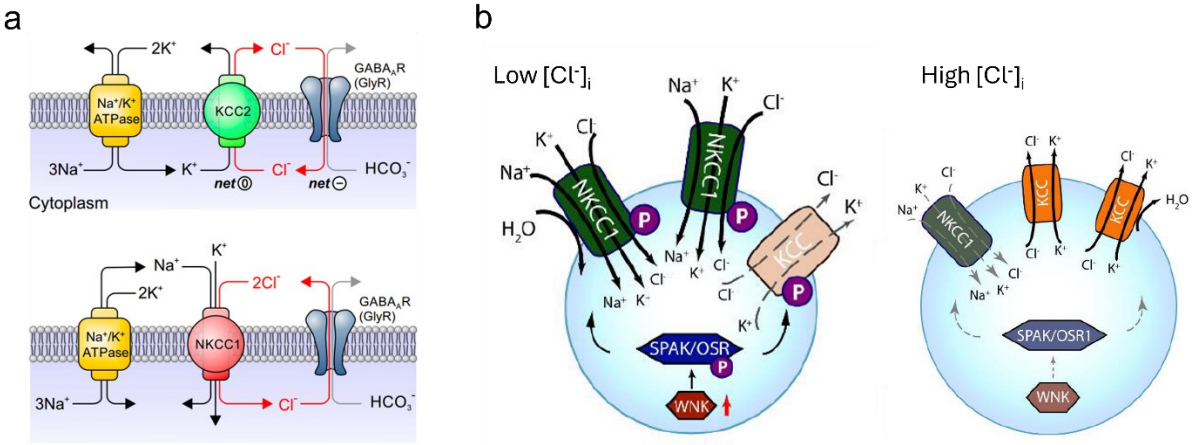

Figure 5: Mechanisms of chloride regulation. a) Schematic view of the activity of KCC2 and NKCC1 and their relationship to ATP consumption. Ion transport through these cotransporters is electroneutral. NKCC1 acts as a chloride-importer while KCC2 extrude chloride ions from the cell. Adapted from Doyon et al., 2016. **b)** In low $[Cl^-]_i$, the WNK-SPAK/OSR1 pathway is activated and phosphorylates NKCC1 and KCCs, resulting in NKCC1activation and KCCs inhibition. This subsequently leads to influx of Na^+, K^+ and Cl^- via NKCC1

along with water. On the contrary, high $[Cl^-]_i$ inhibit autophosphorylation on WNK and the WNK-SPAK/OSR1 pathway remains inactive. This results in NKCC1 inhibition and activation of KCCs, leading to KCC-mediated efflux of K^+ and Cl^- along with water. Adapted from Huang et al., 2019.

2.2.2 The dual nature of GABAergic signalling

As in adult neurons the V_{Cl} lies near the resting membrane potential, minor changes in $[Cl^-]_i$ can significantly affect the strength and even polarity of GABA's effect. The likelihood of action potential increases with depolarization and decreases with hyperpolarization. As previously described, low $[Cl^-]_i$ facilitates GABA-mediated inhibition, whereas high $[Cl^-]_i$ facilitates GABA-mediated excitation, recognized in literature as depolarizing GABA (Cherubini et al., 1991; Ben-Ari, 2002). If $[Cl^-]_i$ exceeds about 20-25 mM, the $GABA_A$ opening depolarize the membrane potential of the cell toward the threshold potential for the activation of sodium channels (Staley et al., 1995). However, another condition is present in which GABA can depolarize and still inhibit target cells. This condition was named shunting inhibition and takes place when V_{Cl} is higher than V_m but lower than the action potential threshold (≈ -40 mV) (Stein & Nicoll, 2003). Indeed, completely excitatory action of GABA can be exerted just if the V_{Cl} is higher than the firing threshold of postsynaptic cells (**Figure 6**a).

A physiological role of depolarizing GABA was found during development. Indeed, levels of $[Cl^-]_i$ are relatively high in immature neurons and start to decrease during early development. Young neurons (<P12 in mice) accumulate Cl^- through NKCC1, the dominant cation chloride cotransporter expressed at this stage, and maintain a high $[Cl^-]_i$, thus making GABAergic transmission depolarizing and excitatory (Rivera et al., 1999; Herstel et al., 2022; Yamada et al., 2004). This condition facilitates the generation of endogenous large-scale spontaneous activity characteristic of developing mammalian CNS structures, named as giant synaptic potential (Ben-Ari et al., 1989; Ben-Ari, 2001). Indeed, this activity was seen in different regions of the brain of different animal species, from reptiles to primates, suggesting that this is a conserved feature of evolution (Ben-Ari et al., 2012).

In mice, it was demonstrated that 12 days after birth there is a gradual upregulation in the expression of KCC2, with the simultaneous down-regulation of the NKCC1 (**Figure 6**b). This leads to a Cl^- extrusion and a negative shift in the V_{Cl} beyond the resting membrane potential, resulting in a switch of GABA action from excitatory to inhibitory (Fiumelli & Woodin, 2007). Even though the shift of Cl^- electrochemical gradient was a conserved phenomenon, there is considerable variation in the developmental time course of KCC2 expression among brain structures both within a species and across species (Ben-Ari, 2002). For instance, KCC2 expression in the human neocortex starts to increase at 40 weeks after conception.

Even though the role of depolarizing GABA is widely accepted in relation to development, far less is known about the possibility of physiological depolarizing activity of GABA in the adult. However, some physiological and pathological conditions were described in which GABAergic activity was observed to be depolarizing. Notably, all of them were caused by an increase of $[Cl^-]_i$ and the consequent positive shift in the V_{Cl}. Even brief synaptic

stimulation can cause long-term synaptic plasticity at GABAergic synapses manifested by a depolarization shift of the reversal potential for GABA (Balena & Woodin, 2008). In addition, activity-induced depolarizing shifts in V_{Cl} have been observed after tetanic stimulation (Kaila et al., 1997), epileptic activity (Avoli, 1996; Kapur & Coulter, 1995; Rivera et al., 2004), correlated synaptic activity (Woodin et al., 2003), repeated postsynaptic spiking (Fiumelli et al., 2005), and application of BDNF (Wardle & Poo, 2003).

The study of depolarizing GABAergic activity is complicated by the fact that different neuronal classes exhibit highly variable intracellular chloride concentrations. For instance, a peculiar behaviour was observed in neurons of the suprachiasmatic nucleus (SCN) in which $[Cl^-]_i$ was demonstrated to oscillate during the day (Wagner et al., 1997). This diurnal oscillation of SNC neurons includes high $[Cl^-]_i$ during the day and low chloride concentration at night and were found in nocturnal animals as rats. For a long time, it was thought that this peculiar chloride fluctuation was restricted to SCN. Recent discoveries pointed out at a similar regulation in other brain areas. This topic will be extensively discussed in the next chapter.

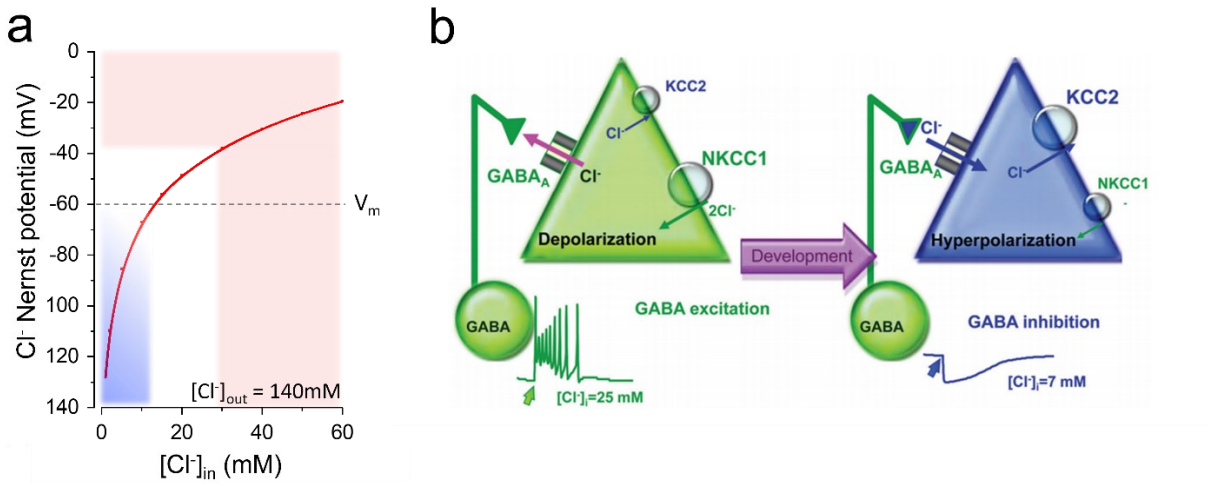

Figure 6: Chloride gradient determines GABAergic polarity a) Nernst potential for chloride ion according to its intracellular concentration value (assuming $[Cl^-]_{out}$ = 140mM). Depending on $[Cl^-]_i$, GABA can induce hyperpolarization, shunting inhibition or depolarization of the post-synaptic cell. In this simplification we don't consider the permeability of $GABA_A$ to bicarbonate, and we equate V_{cl} to $GABA_A$ reversal potential. Coloured areas depict the $[Cl^-]_i$ ranges in which a Cl^- flux mediated by $GABA_A$ opening exerts a hyperpolarizing (blue) or depolarizing (red) effect. Withe area depicts the shunting inhibition range. **b)** GABAergic activity is determined by the activity of two major chloride cotransporters. Early in the development, NKCC1 shows a higher activity, while it is later replaced by KCC2 (adapted form Ben-Ari et al., 2012).

2.2.3 Diurnal chloride fluctuations: the scientific debate

Whether intracellular ions fluctuate over the course of the day has only recently become a subject of scientific investigation. Early studies have begun to reveal that ionic homeostasis is not static but dynamically regulated across the 24-hour cycle. For instance, Feeney et al., (2016) first described circadian oscillations in intracellular magnesium and potassium in both human cells and unicellular algae, while Stangherlin et al., (2021) later demonstrated coordinated daily variations in Na^+, K^+, and Cl^- in

mammalian fibroblasts and cardiomyocytes. These findings established the principle that ion concentrations can follow a diurnal rhythm, although neither study directly examined chloride dynamics in neurons.

Whether $[Cl^-]_i$ oscillates in the mammalian cortex has been addressed only recently. Two independent studies have provided complementary data but, partly divergent, interpretations. Alfonsa et al., (2023) demonstrated that cortical pyramidal neurons exhibit diurnal shifts in the reversal potential for $GABA_A$ (E_{GABAA}) receptors, reflecting higher $[Cl^-]_i$ during the active (dark) period (**Figure 7**b). According to the study, these shifts depend on neuronal activity and NKCC1, suggesting that chloride accumulation is linked to cortical "use" and local sleep pressure rather than to intrinsic circadian timing. Also, Pracucci et al., (2023) reported *in vivo* imaging evidence of rhythmic chloride fluctuations in cortical neurons, showing, consistently with Alfonsa's findings, an increase in $[Cl^-]_i$ during the dark (active) period. However, because these oscillations persisted under constant light conditions, they interpreted them as intrinsic circadian rhythms driven by endogenous clocks rather than as a consequence of local cortical activity or sleep pressure (better explained in the result session 3.1). Despite their different viewpoints, both studies independently revealed that cortical $[Cl^-]_i$ varies over the 24-h cycle, implying that neuronal inhibition, and hence excitability, changes across the day. In particular, the higher chloride levels during the night could make neurons more excitable.

Further supporting the functional importance of these fluctuations, Alfonsa et al., (2025) demonstrated that sleep–wake-related changes in the E_{GABA} regulate glutamatergic synaptic plasticity. During the active period, this higher GABA's reversal potential facilitates long-term potentiation in cortical pyramidal neurons, linking chloride homeostasis to experience-dependent plasticity and learning.

Interestingly, the rhythm observed in cortex contrasts with that found in the suprachiasmatic nucleus, namely the brain's central circadian clock, where an opposite pattern was observed: daily shifts in GABAergic polarity in the SCN were first reported by Wagner et al., (1997), who showed that GABA transmission switches from depolarizing during the day to hyperpolarizing at night, implying rhythmic changes in intracellular chloride concentration. Building on this, more recent work using long-term *ex-vivo* imaging directly assessed intracellular chloride dynamics and confirmed a robust circadian rhythm in SCN neurons, with $[Cl^-]_i$ peaking during the day and reaching a trough at night (Klett et al., 2022). This suggests that the phase of chloride rhythms could be region-specific, reflecting the functional demands of different neuronal circuits.

Together, these studies converge on the idea that intracellular chloride is not static but dynamically regulated across the diurnal cycle. Whether this reflects an intrinsic circadian rhythm or a homeostatic response to neuronal activity remains debated. Nevertheless, the consistent observation of diurnal chloride variations across independent studies highlights the importance of studying $[Cl^-]_i$ for understanding the modulation of GABAergic inhibition, sleep–wake history, neuronal excitability, and synaptic plasticity.

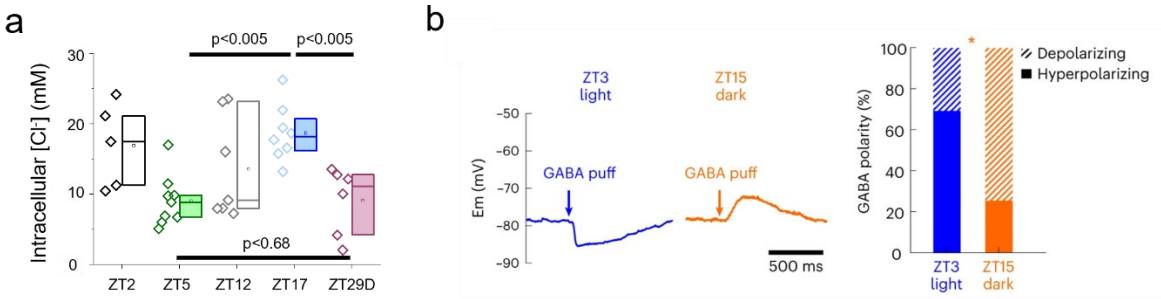

Figure 7: Intracellular chloride concentration oscillates diurnally. a) Quantification of $[Cl^-]_i$ at 5 time points. The points are the median values for individual animals. Adapted from Pracucci et al., 2023. **b)** Current-clamp recordings show $GABA_AR$ responses in a slice prepared at ZT3 or at ZT15 (*left*). The proportion of depolarizing $GABA_AR$ responses (*right*) was greater at ZT15 than at ZT3. Adapted from Alfonsa et al., 2023.

2.2.4 The interneural landscape

Cortical circuits are built upon the dynamic interplay of excitatory neurons and inhibitory interneurons (Lim et al., 2018; Tasic et al., 2016). While the majority of neocortical neurons are glutamatergic pyramidal cells (70-80%), inhibitory interneurons, which release GABA, constitute about one fourth of the neuronal population and are indispensable for local circuit regulation (DeFelipe et al., 2013). Unlike excitatory neurons, interneurons establish only local connections, sculpting the timing and gain of network activity (Tremblay et al., 2016). Despite their smaller number, these cells are remarkably diverse in terms of morphology, physiology, and gene expression, and are commonly grouped into three cardinal classes: Parvalbumin (PV), Somatostatin (SST), and 5HT3a receptor–expressing interneurons (Lim et al., 2018; Llorca & Deogracias, 2022) (**Figure 8**).

Parvalbumin-expressing (PV^+) interneurons comprise a large and functionally central fraction of cortical inhibitory cells. They are classically associated with perisomatic inhibition and are defined by electrophysiological and morphological features that enable tight control over pyramidal neuron output. PV^+ cells characteristically display fast-spiking behaviour. Morphologically and functionally, PV^+ interneurons are commonly subdivided into three principal types. Basket cells, the most abundant PV subtype, exhibit axonal arborization that densely innervate the soma and proximal dendrites of surrounding pyramidal neurons as well as other interneurons (Hu et al., 2014). The second group are the axo-axonic (Chandelier) cells. They form a distinct and highly specialized population that targets the axon initial segment of pyramidal neurons; by synapsing at this site, they exert a particularly powerful influence on spike initiation (Somogyi et al., 1982). Translaminar PV interneurons, the third PV subtype, is relatively rare but distinctive: these neurons are most prevalent in deep cortical layers (notably layers 5–6) and extend axons that traverse the full cortical thickness, innervating pyramidal cells across multiple layers. Because of this vertical reach, translaminar PV cells have been proposed to provide a form of column-spanning, generalized gain modulation across the cortical column (Bortone et al., 2014).

Somatostatin-expressing (SST^+) interneurons preferentially target the distal dendrites of pyramidal neurons, thereby regulating the integration of excitatory inputs arriving from

local and long-range sources. This dendrite-targeting specialization places SST^+ cells in a central position for controlling the input–output transformation of pyramidal neurons and for modulating synaptic plasticity. Within the SST^+ class, two principal subtypes are recognized: Martinotti cells and non-Martinotti cells. Martinotti cells form a distinctive and abundant group. Their hallmark feature is an axon that ascends toward layer I, where it branches profusely to form dense terminal arborizations (Wang et al., 2004). By innervating the distal apical dendrites of pyramidal neurons, Martinotti cells establish a strong inhibitory influence on the sites where pyramidal neurons receive long-range corticocortical and thalamocortical inputs. In addition to targeting pyramidal cells, Martinotti cells also inhibit other interneurons, including PV^+ basket cells and VIP^+ bipolar cells, thereby contributing to disinhibitory loops and to the fine regulation of local circuit excitability. Non-Martinotti SST interneurons, by contrast, lack projections to layer I. Instead, their axons arborize locally within the layer of origin or extend into immediately adjacent layers. This subtype is especially enriched in layer IV, where they form reciprocal connections with local excitatory granule cells and strongly inhibit PV^+ basket cells. In terms of electrophysiology, non-Martinotti cells typically fire at higher frequencies than Martinotti cells, though not as high as the fast-spiking PV^+ population, reflecting their intermediate inhibitory dynamics.

The third cardinal class of cortical interneurons is defined by the expression of the serotonin receptor 5HTR3a. In contrast to PV^+ and SST^+ interneurons, $5HTR3a^+$ cells are particularly enriched in superficial layers, especially in layer I and layers II/III, where they form a heterogeneous population distinguished by diverse morphologies, firing patterns, and connectivity profiles. Within this class, vasoactive intestinal peptide (VIP^+) bipolar interneurons represent the most abundant subtype. They are primarily located in layer II/III and are characterized by vertically oriented axons and adapting firing properties. Other than vasoactive intestinal peptide, these neurons typically co-express calretinin and are functionally specialized to inhibit other interneurons, most notably PV^+ basket cells and SST^+ neurons, thereby providing an effective disinhibitory control over local pyramidal cells (Pfeffer et al., 2013). A second subset of $5HTR3a^+$ interneurons also express VIP but displays alternative morphologies, contributing to the heterogeneity of this group. Layer I of the neocortex, though sparse in excitatory neurons, hosts a diverse set of $5HTR3a^+$ interneurons. Among them, Neuron-derived neurotrophic factor-positive ($NDNF^+$) neurogliaform cells are well characterized, displaying late-spiking activity and dense, locally restricted axons that target both pyramidal dendrites and nearby interneurons, thereby mediating widespread inhibition in superficial layers (Letzkus et al., 2011).

Even though all the interneurons originate front the same area of the subpallium, when they migrate to the cortex they gradually acquire their molecular, morphological, and synaptic identities that contribute to generate a very diverse group (Anderson et al., 1997). Advances in single-cell transcriptomics have further highlighted the complexity of interneuron subtypes (Ascoli et al., 2008; Bugeon et al., 2022; DeFelipe et al., 2013). Functionally, the primary role of these inhibitory interneurons is to suppress the activity of excitatory pyramidal neurons, a process predominantly mediated by $GABA_A$ receptors. Being chloride the main effector of $GABA_A$ receptors, studying chloride dynamics serve as a direct readout of inhibitory interneuron activity, linking the molecular and circuit-level diversity of interneurons to their functional impact on cortical computation.

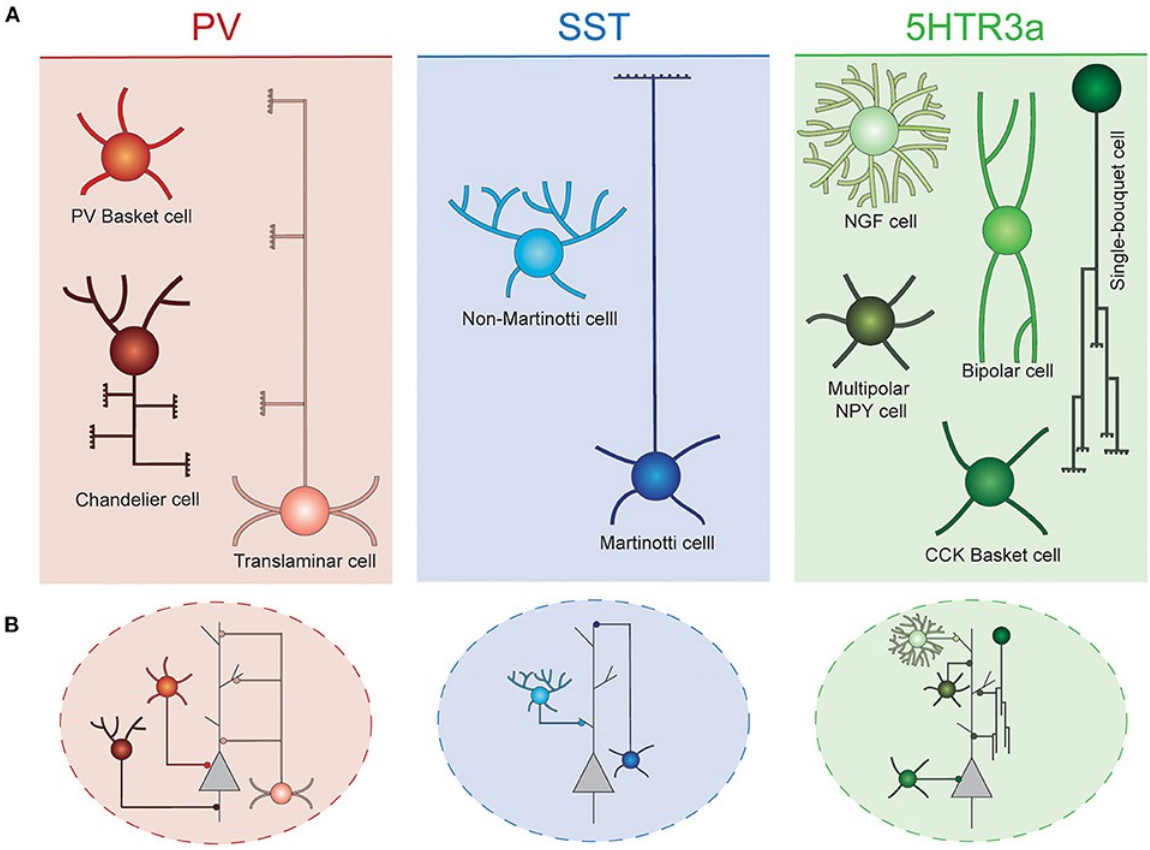

Figure 8: Interneuron diversity in the murine neocortex. a) Cortical interneurons can be classified into three main classes: PV, SST, and 5Htr3a. Each of these classes can be further subdivided into different types. **b)** Different interneuron types preferentially target specific compartments of surrounding projection neurons. Basket cells target their soma. Chandelier cells specifically innervate axon initial segments. SST and 5Htr3a cells mostly target projection neuron dendrites at different levels. PV, parvalbumin; SST, somatostatin; NGF, neurogliaform; NPY, neuropeptide Y; CCK, cholecystokinin. Adapted from Llorca & Deogracias, 2022.

2.2.5 Brain oscillations and inhibition in cortical circuits

Although they represent about 25% of cortical neurons, GABAergic interneurons dramatically determine the computational repertoire of cortical circuits by shaping when and how pyramidal cells fire (Schmidt-Wilcke et al., 2018). Inhibitory populations tune sensory responses to specific features, implement gain control, and coordinate large groups of neurons into temporally organized activity patterns that are observed as brain oscillations of the extracellular field potential (Bortone et al., 2014; Buzsáki & Wang, 2012; Liu et al., 2011; Pouille et al., 2009). Since the earliest stage of human electrophysiology, neural rhythmic activity has been classified into delta (0.5–4 Hz), theta (4–8 Hz), alpha (8–13 Hz), beta (13–30 Hz), and gamma (30–80 Hz) bands, each reflecting partially synchronized neurons within a local population. Inhibition is fundamental to these rhythms because it converts steady excitation into temporally structured windows of high and low spiking probability. The negative feedback loop of excitatory and inhibitory neurons generates alternations of excitatory and inhibitory windows at a frequency set by the synaptic delays and the kinetics of excitation and inhibition. Such an oscillatory motif occurs in cortical networks, where many of these loops interact, producing macroscopic rhythms that contribute to the spectral composition of the local field potential.

Inhibitory timing gates excitatory communication. By constraining pyramidal spiking to narrow phases of the cycle, inhibition increases the impact of coincident inputs on downstream targets and supports spike-timing-dependent plasticity, a key mechanism for Hebbian learning (Song et al., 2000). Rhythms are therefore not only incidental consequences of circuit dynamics but active mechanisms for routing information. For instance, increases in slow wave amplitude after a motor learning task localize to the trained cortical area and predict performance improvements after sleep, indicating that oscillations could contribute to consolidation processes (Huber et al., 2004). At faster timescales, oscillatory coordination has been proposed to bind distributed features and regulate effective connectivity between regions (Fries, 2015).

Multiple inhibitory subtypes contribute with distinct kinetics and targeting rules. Perisomatic inhibition from fast-spiking cells can lock the timing of spike initiation, while dendrite-targeting interneurons shape integration and gain on a slightly delayed timescale, stabilizing the cycle and sculpting stimulus dependence (Onorato et al., 2025). In primary visual cortex, visually driven low-gamma rhythms emerge during drifting grating stimulation and depend on interneuron recruitment patterns that track stimulus size and context, underscoring the causal role of inhibition in generating and sustaining the rhythm (Veit et al., 2017). In this framework, inhibitory efficacy and timing determine the amplitude, frequency, and phase structure of the oscillation, and thereby set when excitatory assemblies communicate most effectively.

2.2.5.1 The physiology of inhibitory visual responses

Inhibition plays a central role in shaping how visual signals are represented in the primary visual cortex (V1). Rather than acting as a simple brake on excitatory activity, inhibitory circuits actively sculpt the spatiotemporal profile of visual responses. By controlling the gain of pyramidal neurons, inhibition enhances contrast sensitivity, sharpens orientation tuning, and keeps cortical activity within a useful dynamic range, preventing excitatory responses from becoming saturated. Moreover, inhibitory inputs determine how cortical neurons adjust their responses according to behavioural state. Inhibitory interneurons therefore provide the framework through which visual stimuli are transformed into precise cortical activity patterns, ensuring that pyramidal neurons encode visual features with both selectivity and flexibility. In this section, I summarize some of the current knowledge about the physiology of inhibitory responses to visual stimulation.

Drifting gratings are the canonical stimulus used to characterize orientation and direction selectivity in V1. In urethane anesthetized mice, inhibitory neurons are generally less selective than excitatory neurons. Early *in vivo* calcium imaging revealed that most GABAergic neurons in layer 2/3 responded to gratings in an orientation-insensitive manner, whereas neighbouring pyramidal cells exhibited strong orientation tuning (Sohya et al., 2007). Subsequent work confirmed that PV, SST, and VIP interneurons all tend to show broader orientation and spatial frequency tuning than excitatory cells, and their responses often mirror the average tuning of the surrounding population rather than being independent from it (Kerlin et al., 2010. **Figure 9**c). The broader tuning observed in inhibitory neurons may result from variations in the strength and density of their local

synaptic inputs, as well as their extensive gap-junction coupling, compared to excitatory neurons in layer 2/3.

In awake mice, inhibitory visual responses are strongly modulated by behavioural state. During locomotion, visual responses of pyramidal cells increase in gain. Initial models proposed that this effect arose through disinhibition: during locomotion, cholinergic inputs are recruited and excite VIP interneurons, which in turn suppress SST activity. This disinhibits the dendrites of pyramidal neurons and enhances their visual responses (Fu et al., 2014; Reimer et al., 2014). However, subsequent imaging studies demonstrated that locomotion actually increases activity in PV, SST, and VIP interneurons (Dipoppa et al., 2018; Polack et al., 2013). SST neurons, in particular, show highly context-dependent responses: they are weakly responsive during locomotion in darkness, but increase their activity significantly when locomotion coincides with visual stimulation (Polack et al., 2013). These findings were further refined by (Pakan et al., 2016): using two-photon calcium imaging, the authors demonstrated that locomotion boosts the responses of PV, SST, and VIP cells during visual stimulation, whereas in darkness SST cells remain largely non-responsive (**Figure 9**d). However, there is currently no consensus in the literature, as other studies have reported differing results, leading to alternative interpretations and hypotheses (Dipoppa et al., 2018; Fu et al., 2014; Polack et al., 2013). Anyway, these observations confirmed that behavioural-state modulation of inhibition is not uniform, but depends both on interneuron subtype and on the sensory context. Crucially, the data argue against a universal disinhibitory mechanism: rather than a simple circuit in which locomotion uniformly suppresses inhibition via VIP–SST interactions, different interneuron classes are differentially engaged depending on context, suggesting a more distributed and flexible form of inhibitory modulation.

Consistent with these findings, another study has shown that most interneuron subclasses respond to gratings with relatively low orientation and direction selectivity, regardless of behavioural state (Bugeon et al., 2022). PV and SST neurons are typically excited by gratings, whereas VIP and Lamp5 interneurons show a mixture of excitation and suppression. Importantly, locomotion modulates the gain of these responses in a subtype-specific manner, but does not fundamentally alter their weak selectivity. This reinforces the idea that inhibitory activity reflects broad, population-level features of the visual input rather than precise, highly tuned coding of orientation or direction. Together, these observations indicate that locomotion does not simply disinhibit pyramidal neurons but reorganizes the balance of excitatory and inhibitory inputs in a subtype-specific fashion. Rather than a uniform release from inhibition, pyramidal neurons experience an increase in both excitation and inhibition, with neuromodulatory inputs further shaping the dynamics.

In conclusion, inhibitory interneurons cooperate to shape the inhibitory drive onto pyramidal cells. Importantly, there is a distinction between interneuron activity and the resulting inhibitory effect on pyramidal neurons. While interneuron responses are broadly tuned across orientations, the chloride influx in pyramidal cells following visual stimulation can be shaped by the specific synaptic arrangements and the spatial-temporal summation of inhibitory inputs. Moreover, the overall chloride dynamics in pyramidal neurons are expected to follow the activation patterns of interneurons (**Figure 9**b). Finally, in awake

mice, locomotion acts as an additional driver of chloride influx, which interacts with visually evoked responses, further modulating pyramidal cell activity.

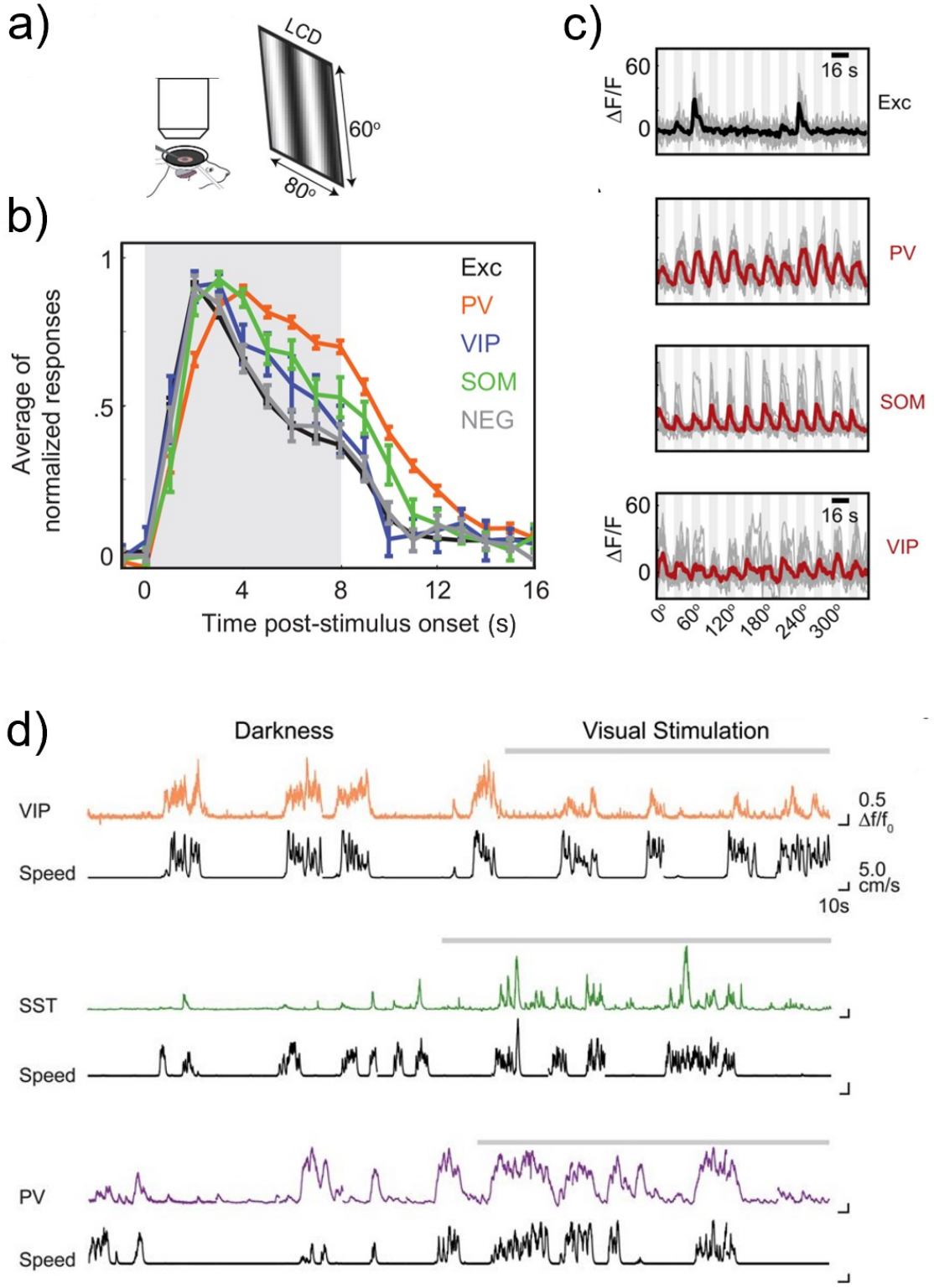

Figure 9: Modulation of inhibitory neuron's activity by visual stimuli and locomotion. a) schematic of visual stimulation. **b)** Magnitude and time course of visually evoked calcium responses of excitatory and all GABAergic subtypes of urethane anaesthetized mice. "NEG" refers to other GAD67^{+} neurons **c)** Recordings of visually evoked calcium responses in excitatory and inhibitory interneurons. Responses from PV, SOM, and VIP subtypes of GABAergic neurons, were generally unselective or weakly selective to the orientation of the stimulus. **d)** Example calcium transients (ΔF/F0, colored traces) of single VIP, SST and PV neurons, imaged

in darkness and during visual stimulation with oriented gratings (grey bar above trace), and aligned with the corresponding running speed (cm/s, black traces). Figure adapted from: Kerlin et al., 2010; Pakan et al., 2016; Sohya et al., 2007.

2.2.6 Effects of diurnal chloride fluctuations

Intracellular chloride concentration is dynamically regulated across the 24-hour cycle, and these fluctuations exert a profound influence on neuronal physiology (Alfonsa et al., 2023, 2025; Pracucci et al., 2023). In mouse V1, visually evoked gamma oscillations are strongly modulated across the day in a chloride-dependent manner. When drifting gratings are presented during the daytime rest phase (ZT5), local field potentials exhibit a prominent increase of power in the 20–30 Hz band; the same visual stimulation at night (ZT17), when baseline pyramidal $[Cl^-]_i$ is elevated, yields a markedly reduced gamma peak power. This day–night difference is significant, and pharmacological treatments confirm the causal role of chloride: treating anaesthetized mice with bumetanide at ZT17 lowers $[Cl^-]_i$ and restores the gamma peak power toward daytime values, whereas bumetanide at ZT5 has negligible effect because $[Cl^-]_i$ is already low. These results demonstrate that the diurnal elevation of neuronal chloride weakens visually evoked gamma synchronization and that reducing chloride influx via NKCC1 restores gamma rhythms toward the daytime state (Pracucci et al., 2023).

Different findings shows that wakefulness raises neuronal $[Cl^-]_i$ and shifts the reversal potential of GABA in cortical pyramidal neurons toward depolarized values. Behaviourally, this wake-related increase of $[Cl^-]_i$ associates with markers of high sleep pressure, including increased low-frequency power during wake and poorer task performance after sleep deprivation (Alfonsa et al., 2023). Moreover, the more depolarized GABA's reversal potential in the active period facilitated LTP induction at layer 5 pyramidal synapses, while the blockade of NKCC1 in the active period attenuates LTP (Alfonsa et al., 2025).

2.3 Chloride, inhibition and the clock

Chloride homeostasis is a key determinant of inhibitory synaptic transmission and neuronal excitability. Having discussed its regulatory mechanisms in previous sections, we now turn to how these processes intersect with the molecular machinery of the circadian clock. Recent evidence suggests that chloride regulation is tightly connected with the circadian system, influencing rhythmic changes in neuronal inhibition and excitability across the day–night cycle. Understanding this interplay requires a closer look at the molecular mechanisms underlying the circadian clock itself.

2.3.1 Molecular mechanisms underlying the clock

The circadian clock is a highly conserved molecular system that allows organisms to anticipate and adapt to daily environmental changes. Its intrinsic rhythmicity persists even under constant conditions, demonstrating that it is an endogenous timekeeping mechanism rather than a mere response to external cues. In mammals, the molecular clock is based on a transcriptional–translational feedback loop (TTFL) that drives rhythmic

expression of the core clock genes and their protein products with a period of approximately 24 hours (**Figure 10**a).

At the heart of this loop lie two transcription factors, CLOCK (Circadian Locomotor Output Cycles Kaput) and BMAL1 (Brain and Muscle ARNT-Like 1). In the cytoplasm, CLOCK and BMAL1 form heterodimers that translocate into the nucleus, where they bind to E-box elements (CACGTG) in the promoters of target genes, activating their transcription. Among these targets are the Period (PER1, PER2, PER3) and Cryptochrome (CRY1, CRY2) genes, whose protein products accumulate in the cytoplasm and subsequently form inhibitory PER:CRY complexes. Once these complexes enter the nucleus, they suppress the transcriptional activity of the CLOCK:BMAL1 complex, thereby repressing their own expression and closing the negative feedback loop (**Figure 10**b; Partch et al., 2014).

A secondary loop contributes to the stability and precision of the oscillation. CLOCK:BMAL1 dimers also activate the transcription of Rev-Erbα/β and Rorα/β/γ, nuclear receptors that compete for binding to RORE (ROR response element) sequences within the *Bmal1* promoter. REV-ERBs repress *Bmal1* transcription, while RORs activate it, forming an interlocking regulatory network that reinforces the core feedback cycle. Importantly, the expression of REV-ERBs and RORs peaks at different circadian phases, ensuring a temporal separation between activation and repression that helps to shape and stabilize the oscillatory dynamics of the clock. This layered architecture ensures robust oscillations in both gene expression and protein abundance, generating rhythmicity in a multitude of downstream cellular processes (Kim et al., 2022).

Beyond transcriptional regulation, post-translational mechanisms play a crucial role in determining the timing, stability, and activity of clock proteins. Within the canonical TTFL, phosphorylation by casein kinases CK1δ, CK1ε, and CK2 introduces intrinsic delays that prevent the system from reaching equilibrium, thereby sustaining circadian oscillations in PER and CRY abundance even under constant conditions. Moreover, circadian regulation involves rhythmic protein synthesis and degradation coordinated through signalling pathways such as mTOR and CK2, which post-translationally modify the translational machinery to temporally compartmentalize protein renewal. These finely tuned post-translational modifications ensure proteomic stability and maintain a near-24-hour periodicity in cellular physiology (James & O'Neill, 2025).

Beyond controlling gene expression and protein turnover, the molecular circadian clock also orchestrates rhythmic changes in cellular ion homeostasis. Intracellular concentrations of key ions such as K^+, Na^+, and Cl^- oscillate over the day, buffering the osmotic shifts associated with rhythmic protein synthesis and degradation (**Figure 10**c). These daily ion fluxes contribute to maintaining cellular volume and electrochemical stability, thereby coupling metabolic and osmotic rhythms to the molecular circadian clock. This coordination between proteostasis and ion transport ensures that cellular physiology remains temporally aligned with energy demands across the circadian cycle (James & O'Neill, 2025; Stangherlin, 2023; Stangherlin et al., 2021).

Altogether, the molecular clock acts as a hierarchical, cell-autonomous system capable of integrating environmental cues such as light, feeding, and temperature, while sustaining self-sufficient rhythmicity. This molecular machinery not only governs circadian gene

expression but also influences neuronal physiology and behaviour, providing the foundation for the circadian regulation of brain function discussed in the following section.

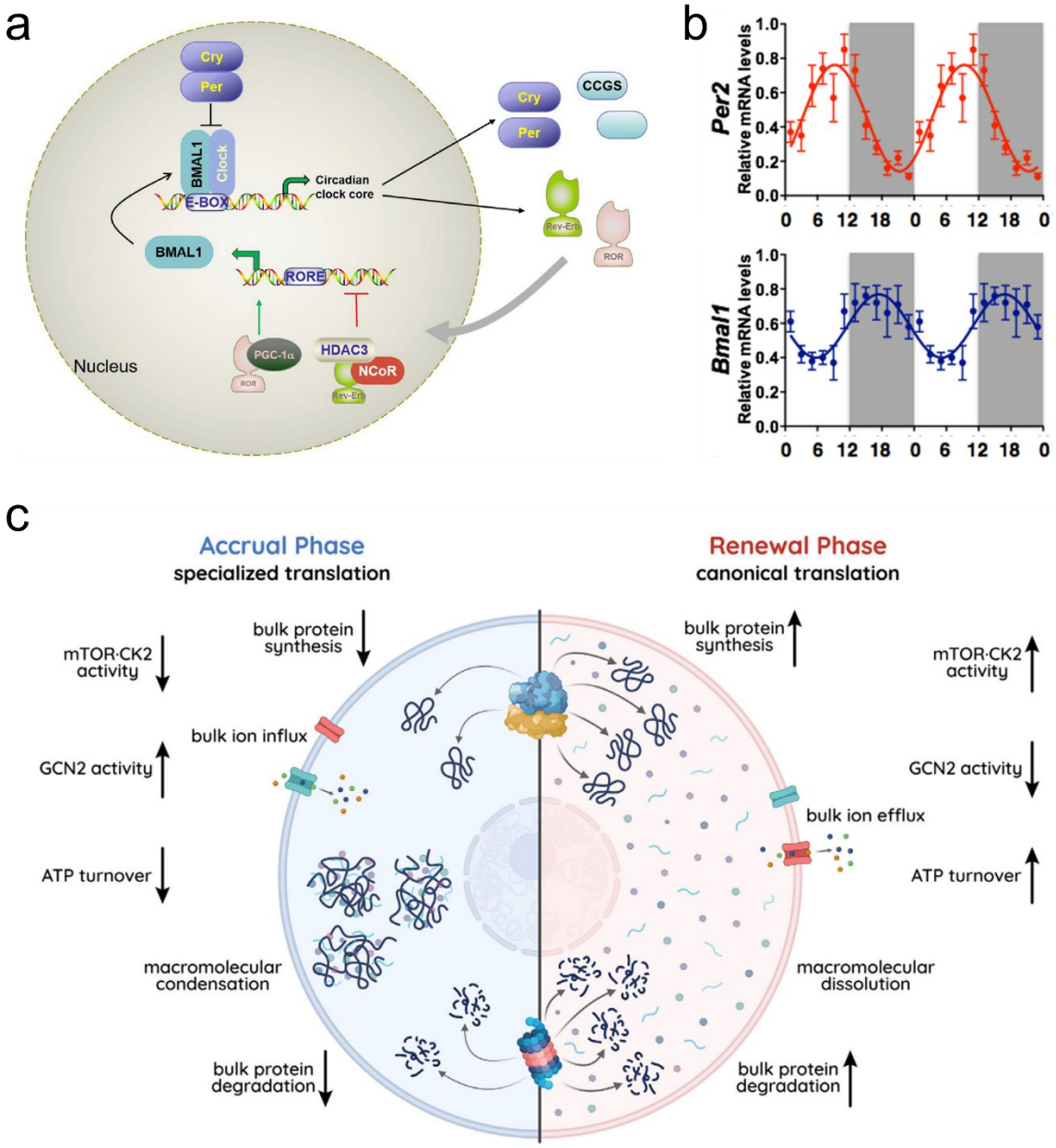

Figure 10: Circadian Molecular Mechanisms and Their Impact on Ion Homeostasis. a) Schematic diagram of the mammalian circadian TTFL. Bmal1 and CLOCK form a heterodimer that binds to the E-box in the downstream gene promoter region and activates Per, CRY, RORα, REV-ERBα, and CCGs. CRY and Per constitute the inhibition arm of TTPL; they dimerize and enter the nucleus to inhibit the activation of Bmal1-CLOCK. This results in oscillating patterns of gene expression. A secondary loop composed of REV-ERBα and RORα competitively binds to the RRE binding site in the BMAL1 promoter and regulates the transcription level of Bmal1. Adapted from Xia et al., 2024. **b)** Graphs illustrating the temporal organization and phase relationship of *Per2* and *Bmal1* mRNA in the rat suprachiasmatic nucleus. Adapted from Harbour et al., 2014. **c)** Cell-autonomous circadian rhythms organize proteostasis into two complementary phases. During the accrual phase, global protein synthesis is reduced while selective translation of specific mRNAs allows cells to save resources and prepare for anticipated metabolic changes. In the renewal phase, signaling pathways such as mTOR and CK2 promote a coordinated increase in protein synthesis and degradation, ensuring proteome turnover without altering total protein content. These rhythmic transitions in proteostatic activity are accompanied by circadian oscillations in intracellular K^+, Na^+, and Cl^-, which maintain osmotic balance and cellular homeostasis throughout the 24-hour cycle. Adapted from James & O'Neill, 2025.

2.3.2 Circadian rhythms in the brain

The activity of mammals, including humans, follows a robust 24-hour rhythm that governs both behaviour and physiology. The most evident manifestation of this rhythmicity is the alternation between sleep and wakefulness, which persists even in the absence of external time cues. Experiments in rodents have clearly demonstrated that their locomotor activity displays self-sustained periodicity under constant environmental conditions. For instance, mice, being nocturnal animals, are predominantly active during the dark phase and rest during the light phase, but they continue to exhibit a near-24-hour rhythm in constant darkness or constant light, with only minimal deviations from the 24-hour period (Hasan et al., 2014). This persistence confirms that the sleep–wake cycle is governed by an endogenous circadian mechanism.

Circadian regulation in the brain extends well beyond sleep and wake states. Numerous aspects of neuronal function display daily oscillations, including firing rate, synaptic strength, and plasticity (Hartsock & Spencer, 2020; Tononi & Cirelli, 2006; Vyazovskiy et al., 2009; Watson et al., 2016). Even neuromodulatory systems show circadian modulation (Yu et al., 2021). Together, these findings illustrate that circadian regulation permeates multiple layers of neural physiology, influencing cellular and molecular processes together with behavioural states.

At the centre of this temporal organization lies the suprachiasmatic nucleus, located in the anterior hypothalamus. The SCN acts as the master pacemaker that synchronizes circadian rhythms throughout the brain and body (Weaver, 1998). Each SCN neuron is an autonomous oscillator, capable of generating rhythmic electrical activity and clock gene expression even in isolation. Yet, for the SCN to track and anticipate solar time, it must be entrained by environmental light, achieved through direct input from intrinsically photosensitive retinal ganglion cells expressing melanopsin (Hattar et al., 2002; LeGates et al., 2014). In circadian biology, a “zeitgeber” (German for “time giver”) is any external cue that synchronizes the internal clock with the environment. Light is the dominant zeitgeber for the SCN, while nonphotic cues such as feeding schedules, social interaction, temperature cycles, and exercise act as weaker zeitgebers, particularly for peripheral clocks. By providing phase-resetting signals, zeitgebers align endogenous rhythms to the 24-hour day, preventing the drift that would otherwise occur under constant conditions. The SCN’s neuronal network translates photic information into coherent timing signals that regulate endocrine, autonomic, and behavioural rhythms across the organism.

The main measurable output of SCN neurons is their spontaneous firing rate, which oscillates between >10 and <1 Hz across the circadian cycle (Green & Gillette, 1982; Colwell, 2011). Importantly, SCN electrical activity reflects solar time rather than behavioural state: its firing rate is high during the SCN circadian day (i.e. light phase), even in nocturnal animals. Light exposure modulates SCN activity through phase-dependent mechanisms. During the SCN circadian day, when firing is already high, light pulses exert minimal effects, while light exposure during the night transiently increases firing and triggers phase shifts in the molecular clock, realigning internal time to external cues (J. R. Jones et al., 2018). This photic entrainment relies on intracellular Ca^{2+}

signalling that activates cAMP/Ca^{2+} response elements (CREs) within *Per1* and *Per2* gene enhancers.

Early studies reported that GABA could be both excitatory and inhibitory in the SCN, with the proportion of excitatory responses varying across the circadian cycle (Wagner et al., 1997). This bidirectional effect is caused by circadian shifts in $[Cl^-]_i$, which alter the reversal potential of $GABA_A$ receptor-mediated currents. Excitatory GABAergic responses are more prevalent during the day (corresponding to a higher $[Cl^-]_i$), peaking around the midday, whereas inhibitory responses dominate during the night (Klett & Allen, 2017). These findings suggest that chloride dynamics contribute to phase-dependent modulation of GABAergic signalling within the SCN, potentially influencing network synchronization and output timing (Belenky et al., 2010).

In summary, circadian rhythms in the brain arise from the interplay between the molecular clock, neuronal network activity, and environmental inputs. The SCN functions as the master synchronizer, translating light information into rhythmic signals that entrain both central and peripheral oscillators. At the same time, local clocks enable region-specific rhythmic modulation of excitability, metabolism, and plasticity, highlighting that the brain's temporal organization is distributed and dynamic to all neural processes.

2.3.3 Epilepsy: a diurnal occurrence

Epileptic seizures do not occur evenly over 24 hours. A growing body of clinical and experimental evidence supports that many forms of epilepsy exhibit diurnal or circadian patterns in seizure occurrence and in the underlying brain activity between seizures. Understanding these daily rhythms is important both for clarifying the mechanisms that regulate neuronal excitability and for optimizing the timing of therapeutic interventions (chronotherapy). For many years a link between seizures and the time of the day was not known, but large-scale EEG studies and chronic implantable recordings have now demonstrated that epileptic activity follows clear temporal patterns rather than being stochastic. Data from over 10 000 individuals with epilepsy, comprising more than one million recorded seizures (Karoly et al., 2021), show a marked predominance of daytime events, with peak incidence between late morning and early afternoon and the lowest occurrence during the night. These findings confirm that epileptic activity in humans is largely a diurnal phenomenon, though individual "seizure chronotypes" vary depending on epilepsy type and brain region of onset. Importantly, the sleep–wake cycle interacts with but does not fully explain circadian seizure timing. The mechanisms underlying this diurnal modulation likely involve a combination of endogenous circadian clocks and state-dependent excitability changes. Molecular circadian regulators such as CLOCK and BMAL1 influence neuronal activity patterns throughout the brain. In mice, deletion of the *Clock* gene in pyramidal neurons results in spontaneous seizures, indicating that clock-controlled transcription directly affects network excitability (Li et al., 2017). Moreover, both the synaptic transcriptome and phospho-proteome of the forebrain exhibit circadian fluctuations, many of which are altered in epilepsy, suggesting that temporal gene regulation contributes to rhythmic seizure susceptibility (Debski et al., 2020).

In addition, alterations in neuronal chloride homeostasis are increasingly recognized as a key mechanism contributing to epileptogenesis. Several studies demonstrate that either persistent or activity-dependent increases in $[Cl^-]_i$ can promote hyperexcitability (Weiss, 2023). Indeed, both chronic downregulation of KCC2 and transient chloride accumulation during intense network activity can reduce GABAergic inhibition and facilitate epileptiform discharges. Genetic and experimental evidence supports this causal role: mutations in KCC2 (SLC12A5) genes, which leads to impaired Cl^- extrusion and a depolarizing shift of the GABA equilibrium potential, have been linked to human epileptic encephalopathies, leading to impaired Cl^- extrusion and a depolarizing shift of the GABA equilibrium potential (Kahle et al., 2014). In addition to being a potential causal factor, intracellular chloride accumulation is also consequence of epileptic activity. During seizure onset, intense synaptic and network activation drives a rapid influx of Cl^- through $GABA_A$ receptors, which can overwhelm the capacity of the chloride extruder KCC2. Using Clomeleon, it was demonstrated that pyramidal neurons in mouse hippocampal slices rapidly accumulate Cl^- at the beginning of seizure-like events and that intracellular Cl^- continues to rise during the ictal phase (Lillis et al., 2012). This chloride accumulation primarily results from massive activation of $GABA_A$ receptors at seizure onset. As the seizure progresses, KCC2 becomes increasingly ineffective in maintaining the chloride gradient, causing a depolarizing shift of E_{GABA}. This shift reduces the inhibitory efficacy of GABAergic signalling and can even render GABA currents excitatory, thereby contributing to the breakdown of inhibition and the propagation of epileptiform activity.

Taken together, these observations indicate that epileptic activity follows a clear diurnal organization, and that chloride homeostasis plays a key role in shaping seizure susceptibility. As discussed earlier in this introduction, intracellular chloride levels in cortical pyramidal neurons oscillate across the day in mice (Pracucci et al., 2023). Such rhythmic modulation may underlie time-of-day differences in seizure susceptibility: when baseline intracellular chloride is elevated, GABAergic inhibition becomes less effective, potentially facilitating seizure generation. This hypothesis will be explored experimentally in one of the results chapters. Furthermore, since intracellular chloride also rises sharply during seizures, as discussed above, the dynamics $[Cl^-]_i$ following epileptic activity will be examined in the results.

3. Results

3.1 Putative circadian mechanism underling the diurnal chloride fluctuation in mouse pyramidal cells

When I joined the laboratory at the beginning of my PhD, the project was already partially underway, with previous work showing that intracellular chloride concentration in pyramidal neurons of the mouse visual cortex does not remain constant but instead exhibits a pronounced diurnal fluctuation (*see introduction 2.2.3*). My contribution focused on extending this line of investigation to a particular experimental condition, namely the ZT29D mice, in which the regular light–dark cycle was extended in order to explore whether chloride homeostasis would remain coupled to behavioural activity or would instead follow an intrinsic circadian regulation. To this end, and in consistency with the previous experimental sets, adult C57BL/6J mice of both sexes (aged 4–6 months) underwent surgical procedures for the expression of the genetically encoded ratiometric sensor LSSmClopHensor in cortical pyramidal neurons of the visual cortex. Mice are usually maintained in a 12 hr light cycle, with light going off at 7 PM and on at 7 AM. Under this light cycle, mice are in in the active phase at night (7PM to 7AM) and start sleeping rapidly after the onset of light at 7AM with consequent rapid reduction of motor activity (**Figure 11**e). To uncouple activity from the Cl^- change, in these experiments light was not switched on at 7 AM and Cl imaging was performed at 12 AM. As a result, the animals experienced a continuous period of darkness lasting more than 16 hours, after which they were imaged at a timepoint corresponding to zeitgeber time 28-29 (ZT29D), i.e. 29 hours after the last darkness-to-light inversion. Following surgery, a recovery period of at least three weeks was observed to allow for stable sensor expression. Prior to imaging, locomotor activity was continuously recorded to assess the behavioural state of the animals (see methods *5.1*). **Figure 11**e-f displays the behavioural results of 5 out of 6 mice imaged (only 5 mice are included because the video recording malfunctioned for one animal). As expected, all the mice remained active during the period of extended darkness (**Figure 11**f *Left*). In 4 out of 5 animals, the periods of immobility were far lower (**Figure 11**f *Right*) indicating that sleep was markedly reduced during prolonged darkness, even if this cannot be considered complete sleep deprivation. This manipulation therefore allowed us to dissociate two normally overlapping variables: the light-driven circadian entrainment and the behavioural sleep–wake state, providing a unique opportunity to test whether fluctuations in neuronal chloride follow environmental lighting cues and motor activity, or whether they are governed by an endogenous circadian mechanism.

Two-photon imaging was carried out in layer 2/3 pyramidal neurons to measure intracellular chloride concentration. Interestingly, despite the marked increase in

behavioural activity during prolonged darkness, chloride followed the same dynamics observed in control conditions: intracellular chloride levels in ZT29D animals are comparable to those measured at ZT5, i.e., in the middle of the normal light phase when mice are typically resting (mean ZT5: 9.05 mM, 9 mice and 663 neurons; ZT29: 9.11 mM, 6 mice and 588 neurons) (**Figure 11**c-d). This suggests that the exposure to light at ZT0, and the subsequent strong reduction in the activity of the mice, are not causally related to the observed $[Cl^-]_i$ cycle. Thus, chloride regulation appeared to remain locked to the circadian cycle rather than to locomotor state or to exposure to light. Statistical analysis confirmed that $[Cl^-]_i$ in ZT29D mice was not significantly different from ZT5 (Mann-Whitney, two-sided, ZT5 vs ZT29D: p=0.68), while both were significantly lower than ZT17 (mean ZT17: 18.68 mM, 8 mice and 1051 neurons; Mann-Whitney, two-sided, ZT17 vs ZT29D: $p=3.7*10^{-3}$). These findings support the conclusion that the diurnal fluctuation of neuronal chloride is not simply a consequence of behavioural state or sleep–wake activity but might be instead mainly governed by intrinsic circadian mechanisms.

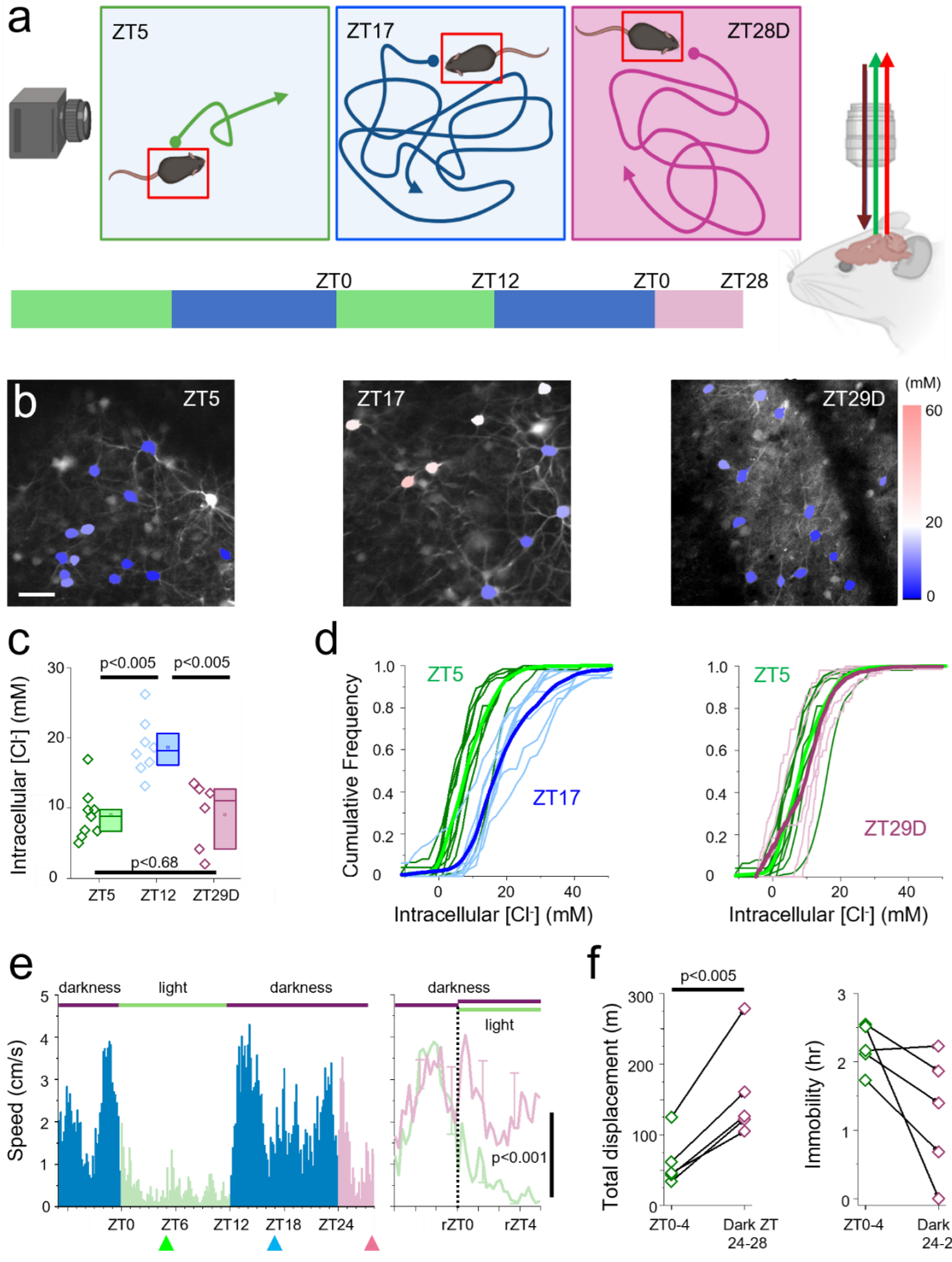

Figure 11: The effect of 4h prolonged darkness on chloride of cortical pyramidal neurons. a) *Top*: Schematic of the behavioural recordings acquired at ZT5, ZT17 and ZT28D. *Bottom*: Schematic of the experimental protocol. Mice were monitored for three days. The data from the first day (when the mouse was placed in the arena) was discarded. At the end of the second day, the mouse was kept in 4 hours of extended darkness. Mice were then imaged at the 2-photon microscope to measure $[Cl^-]_i$. Illustrations were generated with Biorender **b)** Three representative fields of view, showing pyramidal cells expressing LSSmClopHensor, in layers 2/3 of visual cortex, in mice aged >1month. Mice were imaged, under terminal anaesthesia, at the indicated circadian times. The third field, labelled ZT29D, has been imaged after leaving the mice in darkness from ZT12 until anaesthesia 16h later. Calibration bar 40µm. **c)** Quantification of $[Cl^-]_i$ at 3 time points: ZT5 (12:00, 9 mice and 663 neurons), ZT17 (24:00, 8 mice and 1051 neurons) and ZT29 (6 mice, 588 neurons). An average of 4 fields have been acquired for each mouse. The points are the median values for individual

animals, and the box plots show the interquartile range, median (central line) and mean (small symbol) for each experimental group. There is no difference between ZT5 and ZT29D, but both are significantly different from ZT17 (Mann–Whitney, two-sided. ZT5 vs ZT17: $p=1.8*10^{-3}$; ZT17 vs ZT29D: $p=3.7*10^{-3}$; ZT5 vs ZT29D: p=0.68). **d)** *Left*: Cumulative distribution for each mouse imaged at ZT5 (green traces) and at ZT17(blue traces). The thick lines show the mean distributions of the two groups. *Right*: Cumulative distribution for each mouse imaged at ZT5 (green traces) and at ZT29D. **e)** Actogram obtained from the continuous videorecording of 5 out of the 6 mice shown in (c). The mice kept in prolonged darkness were more active compared to the equivalent period when they were in the light (see magnification in the right panel. paired t-test, two-sided, $p=1.8*10^{-4}$. The plot shows the mean ± variance). Bin duration: 10min. **f)** *Left*: The cumulative distance travelled by each mouse increased in prolonged darkness (paired t-test, two-sided, $p=3.5*10^{-3}$, n=5/5). *Right*: the time spent in complete immobility decreased in 4 out of 5 mice. There is no significant correlation between the distance travelled and individual median $[Cl^-]_i$ (p=0.47, ANOVA, n=5).

3.2 The effect of prolonged sleep deprivation on $[Cl]_i$

To assess whether chloride regulation in cortical pyramidal neurons is influenced not only by circadian rhythms but also by sleep, we extended our imaging experiments to the prefrontal cortex (PFC), in collaboration with the research team of Marco Bortolato, specifically interested in this brain region. For these experiments, adult C57BL/6J mice (4–6 months old) of both sexes were employed. The LSSmClopHensor was expressed in PFC pyramidal neurons via the same viral strategy previously described, utilizing a 1:10 mixture of AAV9-EF1a-DIO(LSSmClopHensor) and AAV9-CaMKII-Cre. Two weeks after viral injection of LSSmClopHensor mice were imaged at depths of 80–110 µm in layer 2/3 pyramidal neurons at ZT5 (**Figure 12**d). Under this baseline conditions, intracellular chloride concentrations in the prefrontal cortex were comparable to those measured in the visual cortex ($[Cl^-]_i$ in PFC: 13.5 ± 11.7 mM; $[Cl^-]_i$ in V1: 9.05 ± 3.6 mM; Mann-Whitney, two-sided: p=0.24).

We next examined the effect of 24 hours of continuous sleep deprivation (SD) in PFC. Our sleep deprivation paradigm specifically targeted REM sleep, without interfering with non-REM sleep (Mendelson et al., 1974). To achieve this, we used the well-established “flowerpot” method, in which mice are placed on a small platform surrounded by water. While non-REM sleep episodes can still occur, the loss of muscle tone characteristic of REM sleep causes the animal to fall into the water, thereby preventing REM sleep bouts. Thus, a separate experimental group of the same initial pool of injected animals was subjected to this sleep deprivation protocol. Pyramidal neurons in the prefrontal cortex of sleep-deprived animals displayed a significant elevation in intracellular chloride levels compared to controls (**Figure 12**e; $[Cl^-]_i$ control: 13.56 ± 11.7 mM; $[Cl^-]_i$ SD: 35.9 ± 14.2 mM; Mann-Whitney, one-sided f(x)<g(x), control vs. SD: p= 0.01). A total of 7 mice and 570 cells were imaged in the control group, while 6 mice and 308 cells were evaluated in the SD group.

While our previous experiments had shown that a 4-hour extension of the dark period was insufficient to significantly perturb $[Cl^-]_I$ at ZT5, the extended sleep deprivation paradigm produced a marked effect. These findings indicate that, although chloride homeostasis exhibits a circadian profile under normal conditions, sleep itself exerts an additional and independent influence, with sleep loss imposing a measurable chloride load on cortical pyramidal neurons. It is worth noting that, even if the *flowerpot* is a very used methodology

in literature, it may induce stress to the animal. The latter could contribute to elevating $[Cl^-]_i$, thus introducing a confounding effect.

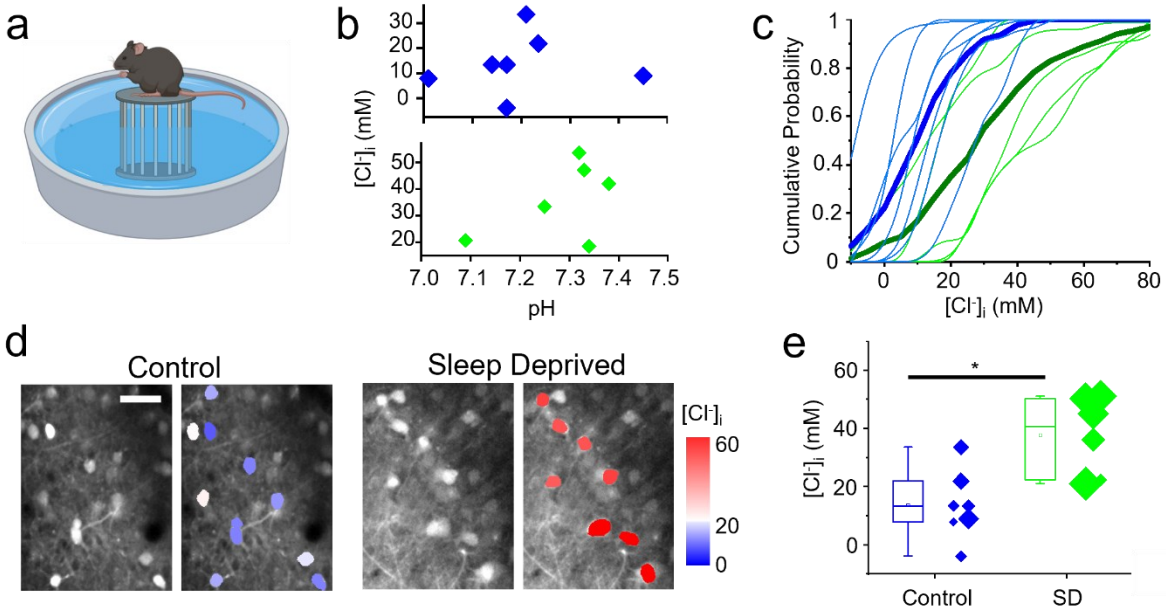

Figure 12: *In vivo* Cl^- imaging in the prefrontal cortex after prolonged sleep deprivation. a) Schematic of the flowerpot sleep deprivation treatment. Mice were sleep deprived for 24h. **b)** Median $[Cl^-]_i$ and pH for each individual mouse. No meaningful correlation was observed between chloride concentration and pH across mice. Data are shown as the median value per animal, although Pearson's correlation was calculated across all analyzed cells (not shown). The correlation was weak in both groups (control: $r = 0.32$, $p = 5.6 \times 10^{-18}$; SD: $r = 0.34$, $p = 1.3 \times 10^{-9}$), indicating only a minor and likely biologically negligible association between chloride and pH. **c)** Cumulative distribution of $[Cl^-]_i$ in control (green thin lines) and in sleep deprived mice (blue thin lines). The thick lines are the averages of the two groups. **d)** *Left:* Two photon imaging in the prefrontal cortex at a depth of 110 µm in a control mouse. The image is the average of the acquisition performed at the 5-excitation wavelengths needed for $[Cl^-]_i$ estimate (see methods 5.4). The cell bodies have been colorized in the right panel to indicate the measured $[Cl^-]_i$. Calibration bar 75 µm. *Right:* Imaging in mouse that was sleep deprived for 24 hours (imaging depth 80 µm). The look up table indicates the concentration in mM. **e)** Cumulative chloride results. Each symbol represents the median $[Cl^-]_i$ for each experimental mouse and the size of each symbol is twice the standard deviation of $[Cl^-]_i$ for each mouse. For each mouse we measured $[Cl^-]_i$ in a variable number of cells dependent on the quality of the sensor transfection. Control: 122, 23, 18, 48, 43, 177, 249; SD: 17, 55, 71, 29, 50, 86. $[Cl^-]_i$ is higher in SD mice (Mann-Whitney, one-sided $f(x)<g(x)$, control vs. SD: $p= 0.01$).

3.3 Seizure susceptibility follows a diurnal rhythm as it is dependent on $[Cl^-]_i$

Since $[Cl^-]_i$ is crucial for the outcome of the inhibitory activity, we tested whether its circadian fluctuations could impinge on cortical excitability and seizure susceptibility. These experiments had already been initiated when I joined the laboratory. My role was to contribute to their continuation, assisting in carrying out and finalizing the experiments for some conditions, as well as in the subsequent analysis of the data.

Elevated chloride levels have long been linked to epileptic activity and are often considered a major factor underlying seizure generation (Kahle & Staley, 2008). Based on this background, we asked whether the natural day–night variation in $[Cl^-]_i$ might modulate the likelihood of epileptiform activity. To address this, seizure susceptibility electrophysiological experiments were performed on adult C57BL/6J mice (4–6 months old) of both sexes. Under deep urethane anesthesia mice were prepared for electrophysiological recording and a small volume of 4-aminopyridine (4-AP; 500 nl, 15 µM in artificial cerebrospinal fluid) was injected directly into the neocortex (**Figure 13**a). Local field potentials (LFPs) were recorded from an area 1mm away from the injection site, either at ZT5 or ZT17. We recorded neural activity for at least 10 minutes prior to 4-AP injection, which always displayed the characteristic slow-wave oscillations (**Figure 13**b).

At ZT17, all tested animals (8/8) rapidly developed pathological discharges progressing to full electrographic seizures within 7–29 minutes after injection (mean latency 17.9 ± 9.5 min SD). In contrast, at ZT5, seizures were observed in only 3 out of 11 mice, and in the remaining experiments no seizure activity was detected during the 60-minute recording period (**Figure 13**d). For consistency, seizure latency in these non-seizing cases was set to 60 minutes, resulting in an estimated average latency of 52 minutes for the ZT5 group. This represents a more than threefold increase compared to ZT17 ($p < 0.005$, Mann-Whitney test) (**Figure 13**e).

To probe the causal role of chloride, we manipulated the system pharmacologically. Pretreating ZT17 mice with cortical application of ACSF containing bumetanide (a selective NKCC1 inhibitor, 55 µM) for 40 minutes strongly suppressed seizure occurrence: in 5 out of 6 mice no seizures occurred within 1 hour, while one mouse had a single, modest seizure after 52 mins (**Figure 13**d, magenta). Thus, blocking NKCC1 activity (which lowers $[Cl^-]_i$ of ~9 mM at night, Pracucci et al., 2023) shifted the ZT17 phenotype towards the more resistant ZT5 state. Conversely, blocking KCC2 for 40 minutes with VU0463271 in ZT5 mice markedly increased seizure susceptibility: 4 out of 5 animals developed intense, sustained epileptiform discharges comparable to those seen at ZT17 (**Figure 13**d, cyan). Thus, the blockage of KCC2 converts the ZT5 to the ZT17 pattern.

Quantification of cumulative pathological activity confirmed these observations (**Figure 13**f-g). We found far higher levels of pathological activity (see methods 5.6) at ZT17 (ZT5 vs ZT17, $p=0.024$, Mann-Whitney test). Again, as with all the other electrophysiology and imaging assays, bumetanide treatment markedly altered the ZT17 pattern, pushing it towards that seen at ZT5 (ZT17-/+bumetanide, $p=0.008$; ZT5 vs ZT17+bumetanide, $p=0.59$). In contrast, VU0463271 increased epileptiform activity at ZT5 (ZT5 vs ZT5+VU0463271 $p<0.05$, Mann-Whitney test) to values not statistically different from ZT17. Together, these findings demonstrate that daily oscillations in pyramidal $[Cl^-]_i$ strongly influence cortical excitability and seizure threshold, and that pharmacological manipulation of chloride transporters can shift these dynamics.

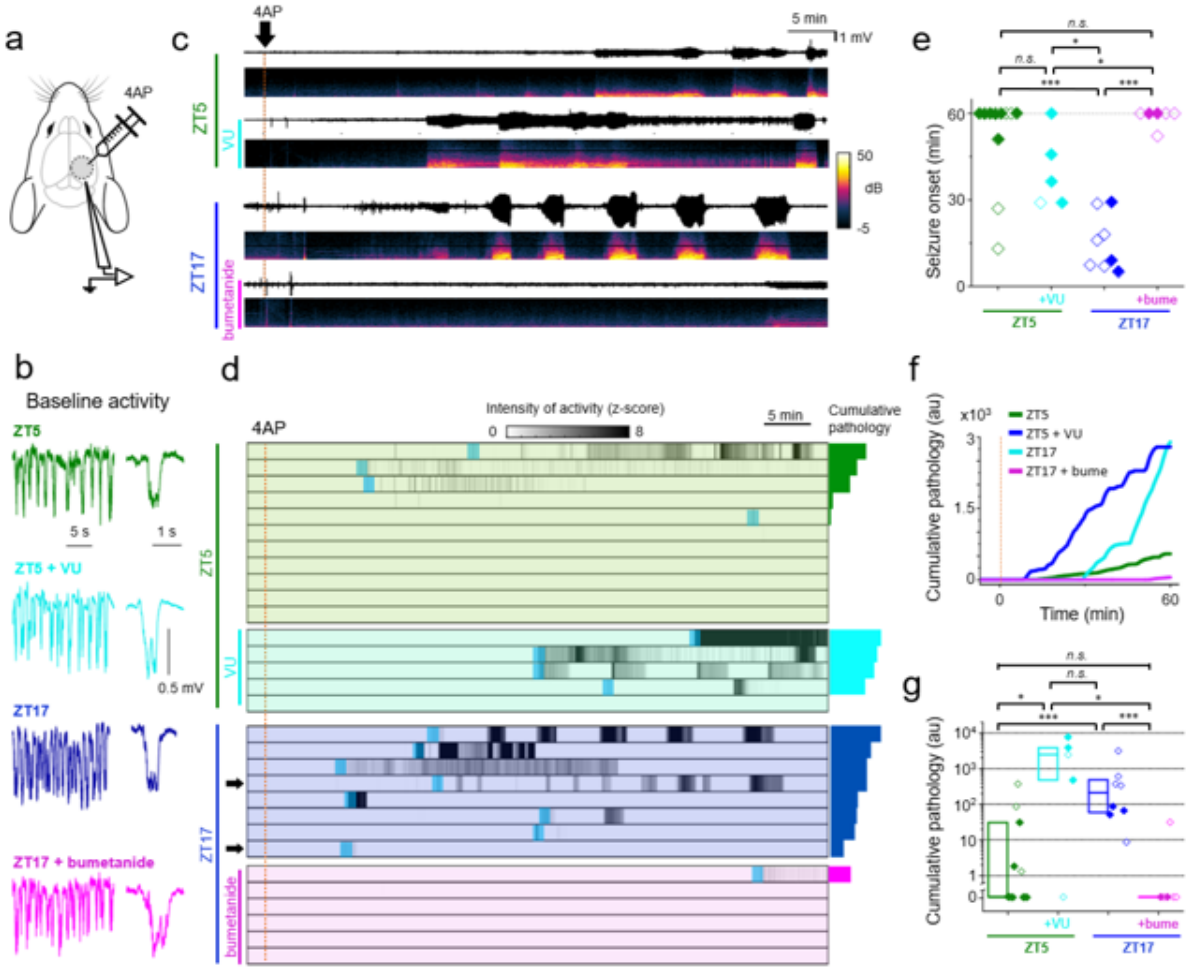

Figure 13: Induced epileptic activity changes with the time of the day. a) Schematic showing the experimental arrangement. **b)** Example LFP traces recorded prior to the application of 4-AP, showing the characteristic rhythmic activity pattern under urethane anaesthesia. In each case, a higher resolution of one of the cortical UP states is shown (downward deflections on the LFP). **c)** Example LFP traces, and corresponding spectrograms, for the first hour after an intracortical injection of 4-aminopyridine (4AP, dotted line), for the four different experimental groups: ZT5 without (green) / with VU0463271 (VU, cyan), and ZT17 without (blue) / with bumetanide (bume, magenta). Drugs were applied 40 min before of the 4AP injection. **d)** Raster plots showing the temporal evolution of the z-score (grey-scale, see Methods 5.6 for details) for all mice included in the study. The light-blue shaded areas indicate the first seizures. The arrowheads in the ZT17 rasters indicate animals where saline was supplemented by 0.08% DMSO but no bumetanide ("vehicle controls"). **e)** Latency to the first seizure. All animals which had no seizures within the hour are depicted as data points at 60 min. Open symbols indicate female mice. Statistical differences were tested using the Wilcoxon rank test (see Methods for the criteria used for burst identification). Two-sided Mann–Whitney tests. ZT5 vs ZT5 + VU: $p = 0.13$; ZT5 vs ZT17: $p = 1.3*10^{-3}$ (**); ZT5 vs ZT17 + bume: $p = 0.54$; ZT5 + VU vs ZT17: $p = 0.01$ (*); ZT5 + VU vs ZT17+bume: $p = 2.8*10^{-2}$ (*); ZT17 vs ZT17+bume: $p = 1.9*10^{-3}$ (**); no correction for multiple tests. **f)** The average cumulative activity recorded for the three experimental groups within the first hour after the 4-AP injection. **g)** The cumulative pathological activity (z-score) in the first hour following the 4AP injection. Box plots show the interquartile range, median (central line) and mean (small symbol). Two-sided Mann–Whitney tests. ZT5 vs ZT5 + VU: $p = 2.5*10^{-2}$ (*); ZT5 vs ZT17: $p = 5.0*10^{-3}$ (**); ZT5 vs ZT17+bume: $p = 0.32$; ZT5 + VU vs ZT17: $p = 0.21$; ZT5 + VU vs ZT17+bume: $p = 2.9*10^{-2}$ (*); ZT17 vs ZT17 + bume: $p = 3.0*10^{-3}$ (**); no correction for multiple tests; There was no statistical difference between sexes. Numbers of animals: ZT5: N = 11; ZT5 + VU: N = 5; ZT17: N = 8; ZT17+bumetanide: N = 6.

3.4 iClima: a new GECS

The need for genetically encoded chloride sensors with improved affinity and reduced pH sensitivity motivated the development of iClima (improved Chloride imaging). The search for such tools led to a collaboration with Daniele Arosio, who engineered few point mutations in the fluorescent protein mClover3. This was reached through iterative optimization to achieve both high chloride affinity and stability against pH variations. Structurally, the sensor consists of a fusion between a chloride-sensitive green fluorescent protein (mutated mClover3), and a chloride-insensitive red fluorescent protein (mCRISPRed). We characterized iClima, as ClopHensor, with the aim of studying chloride dynamics in physiological and pathological conditions *in vivo*.

3.4.1 iClima characterization

Accurate characterization of the sensor is essential to reliably use iClima for *in vivo* experiments. As described in the introduction, three key parameters must be determined: the dissociation constant (K_d), the pK_a, and the fluorescence ratio when [Cl]=0 (R_0). To extract these values, dedicated calibration experiments are required. In the following sections, I describe the *in vitro* calibration strategies we employed, which were performed using two independent imaging setups: a one-photon confocal microscope and a two-photon microscope. This dual approach ensured the robustness of the measurements and validated the performance of iClima under different imaging modalities.

3.4.1.1 Bleed-through measurements

To quantify bleed-through between the spectral channels of the proteins composing the sensor, we performed single-fluorophore controls. Mouse embryonic fibroblasts (MEFs) were transfected by electroporation with either a plasmid encoding mCRISPRed or a plasmid encoding the mutated mClover3, both under the control of the CAG promoter. Two days post-transfection, cells were imaged in phenol red-free medium. For two-photon excitation, both channel 1 (green) and channel 2 (red) were acquired simultaneously at different excitation wavelengths. For one-photon, emission spectra were collected for each fluorophore across a range of excitation wavelengths (**Figure 14**a). BT was calculated according to Eq. 8-9. Specifically, for one-photon acquisition, emission spectra recorded at 450 nm excitation were integrated within the reference detection windows in order to estimate the fraction of the spectrum contributing to bleed-through. These integration windows were chosen to match the emission filters used in the two-photon microscope (527/70 nm for green and 607/70 nm for red). The discrepancy observed between the two BT measurements underscores their dependence on the specific imaging setup and highlights the necessity of performing BT measurements for each system individually.

3.4.1.2 pH calibration

To determine the pH sensitivity of iClima, MEF cells were transfected with a plasmid encoding the sensor under the CAG promoter. Excitation spectra were then measured at different pH values at the two-photon microscope. In order to clamp intracellular ionic concentrations, a series of washes with ad-hoc composed media containing ionophores were performed. These reagents permeabilize the plasma membrane to protons and anions, equilibrating intracellular and extracellular conditions (**Figure 14**b). In this way, the extracellular medium defined the intracellular ionic composition. Spectra were collected at varying pH values while chloride was set to zero (**Figure 14**c). Semi-automated MATLAB scripts were used to draw regions of interest (ROIs) around individual cells and the average signal of both the green and red channels was collected, background subtracted, corrected for PMTs efficiency and BT, and the green/red ratio was calculated (**Figure 14**d). The green/red ratios as a function of the excitation wavelength (from now on, we will refer to it as “green/red excitation spectrum”) were decomposed as a linear combination of the green/red excitation spectra at pH 6.0 and pH 8, obtaining the coefficients ε and δ (**Figure 14**e). These two factors were subsequently used to compute θ as a function of pH (**Figure 14**f). The resulting titration curve was fitted using Eq. 15, yielding a pK_a of 7.8 ± 0.06.

In **Figure 14**e, the errors associated with the fitting coefficients ε and δ are shown. The corresponding uncertainties on θ reflect the propagated error on the pH determination derived from this calibration procedure. From the coefficients ε and δ, the radial coordinate ρ was also calculated. The table below reports the pH values together with the corresponding mean θ and ρ values and their standard deviations.

pH	Mean θ (°)	Error on θ (SD, °)	Mean ρ	Error on ρ (SD)
6	0.23	2.57	1.08	0.28
6.4	1.65	0.85	1.02	0.23
6.8	8.18	1.73	0.99	0.22
7.2	24.96	4.03	0.79	0.18
7.6	58.22	8.53	0.74	0.23
8	89.07	7.62	1.10	0.35

The uncertainty on θ represents the error associated with the estimation of pH. Conversely, the variation in ρ (i.e., the radial coordinate) reflects either a different chloride concentrations or changes in the apparent stoichiometry of the sensor. Differences in chloride concentrations might be attributable to impurities in the calibration media or to residual chloride remaining even after several washing steps. Alternatively, deviations from the ideal stoichiometry of the sensor may occur, even if the two fluorescent proteins are designed to be present in a 1:1 ratio. We hypothesize that these deviations could arise from differences in the maturation kinetics of the two fluorophores. Since the measurements were performed in living, replicating cells, such differential maturation times could lead to transient imbalances in the relative abundance of the green and red components, ultimately producing fluctuations in the measured ρ values.

During this calibration, a total of 2111 cells were analyzed, with a minimum of 152 cells per pH condition. Cell dishes were maintained to a temperature of 32°C during the procedure. The same calibration procedure was repeated under one-photon excitation (see methods *5.7*). The resulting pK_a was 7.8 ± 0.38, closely matching the two-photon estimate. Thus, iClima exhibits a highly reproducible and stable apparent pK_a across different imaging modalities. Lastly, from the excitation spectra obtained at both one-photon and two-photon excitation, we identified the isosbestic points of iClima. For two-photon excitation, the isosbestic wavelength was located at 830 nm (**Figure 14**d), while for one-photon excitation it was identified at 440 nm.

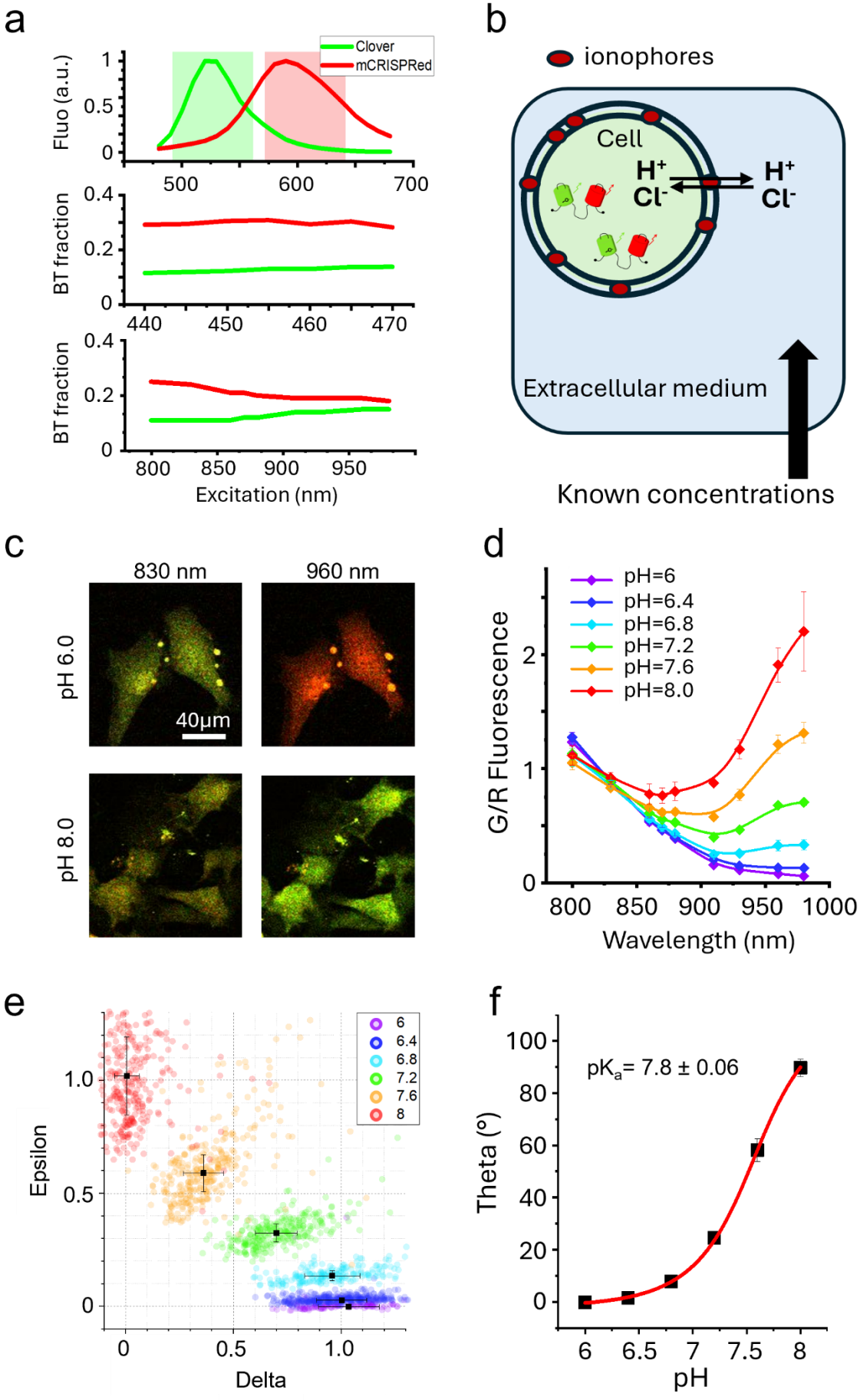
a
Clover
mCRISPRed
Fluo (a.u.)
BT fraction
BT fraction
Excitation (nm)
b
ionophores
Cell
H+
Cl-
H+
Cl-
Extracellular medium
Known concentrations
c
830 nm
960 nm
pH 6.0
pH 8.0
40µm
d
pH=6
pH=6.4
pH=6.8
pH=7.2
pH=7.6
pH=8.0
G/R Fluorescence
Wavelength (nm)
e
6
6.4
6.8
7.2
7.6
8
Epsilon
Delta
f
pKa= 7.8 ± 0.06
Theta (°)
pH

Figure 14: Bleed-through and pH calibration of iClima. a) *Top*, Emission spectra of mutated mClover3 (green) and mCRISPRed (red) excited at 450nm at pH=7.2. *Middle*, BT coefficients representing the leak of each fluorescent protein's signal into the detection channel of the other protein at the one-photon microscope and (*Bottom*) at the two-photon microscope. **b)** Schematic of the calibration process. Six washes are performed in controlled media conditions, in presence of ionophores to equilibrate extracellular and intracellular media. **c)** Representative 2-photon acquisitions of MEF cells expressing iClima in a solution with ionophores $[Cl^-]_i$=0 mM and pH=6.0 (*top*) or 8.0 (*bottom*). **d)** Green fluorescence normalized over red fluorescence at different pH values upon 2 photon excitation. A pH-independent point (isosbestic point) is visible at 830 nm. **e)** Cartesian representation of the components ε and δ at different pH values. Colored points indicate individual cells. **f)** Calibration curve of θ as a function of pH. pK_a, pH_a and pH_b were obtained fitting the experimental data with Eq. 15.

3.4.1.3 Chloride calibration

Following the pH calibration, chloride calibration was performed in MEF cells transfected with iClima. All measurements were carried out at 37 °C, under a constant pH of 7.2, while imposing increasing extracellular chloride concentrations on separate culture plates. For each condition, a minimum of four independent plates were analyzed to ensure reproducibility. Emission spectra were acquired at multiple excitation wavelengths in the one-photon microscope. Semi-automated MATLAB scripts were used to draw ROIs around individual cells, from which emission spectra of iClima were extracted. As expected, the green fluorescence peak, originating from the chloride-sensitive mutated mClover3 domain, decreased as chloride concentration increased, while the red fluorescence peak, corresponding to the chloride-insensitive mCRISPRed domain, remained stable (**Figure 15**a-b). For each plate, the experimental emission spectrum was fitted to the linear combination of the reference spectra of the green and red proteins according to the following model:

$$y = g \cdot G + r \cdot R$$

where G and R are the reference spectra of mClover3 and mCRISPRed, respectively, and *g* and *r* are fitting coefficients. The ratio *g/r* therefore represents the relative contribution of the green and red components, providing a direct readout of the sensor signal. Notably, this spectral fitting approach does not require bleed-through correction because the emission spectrum of iClima is directly decomposed into the reference spectra of mClover3 and mCRISPRed, rather than being separated by fixed emission filters. As a result, the green and red components are mathematically disentangled during the fitting process. The average *g/r* ratios were then plotted against chloride concentration and fitted with Eq. 6 to extract the K_d and R_0 (**Figure 15**c). The fit obtained from excitation at 490 nm (the optimal excitation wavelength for mClover3) yielded an apparent K_d (K_d') of 7.3 ± 1.9 mM. Similar values were obtained at other excitation wavelengths, such as 440 nm (K_d = 9.7 ± 3.0 mM) and 480 nm (K_d = 7.7 ± 2.0 mM), confirming the robustness of the measurement. Thus, we consider the apparent K_d = 7.3 mM as the most representative value. This apparent dissociation constant reflects the protonation state at pH 7.2. By applying the inverse of Eq. 4, the K_d of the fully protonated state of the sensor was calculated to be 5.83 mM. Calibration processes are highly sensitive to even minor chloride contamination. Data acquired with one-photon excitation showed lower variability compared to two-photon experiments, where measurements were noisier and less

consistent. Therefore, one-photon calibration results were considered the most reliable and used to extract the K_d.

The chloride affinity of iClima is substantially higher than that of previously available sensors. For example, LSSmClopHensor exhibits a K_d of 56.5 mM at pH 7.2, far from the physiological intracellular chloride range. In contrast, iClima displays a K_d close to neuronal $[Cl^-]_i$ (~9 mM), making it particularly well-suited for detecting physiological chloride dynamics. Importantly, the high pK_a of iClima (7.8) ensures that measurements are minimally affected by fluctuations in physiological pH (**Figure 15**d), representing a major advantage over earlier genetically encoded chloride sensors. Taken together, these results demonstrate that iClima combines high chloride affinity with pH stability, making it a powerful and improved tool for investigating fine $[Cl^-]_i$ dynamics in living cells, including subtle physiological fluctuations that were previously inaccessible.

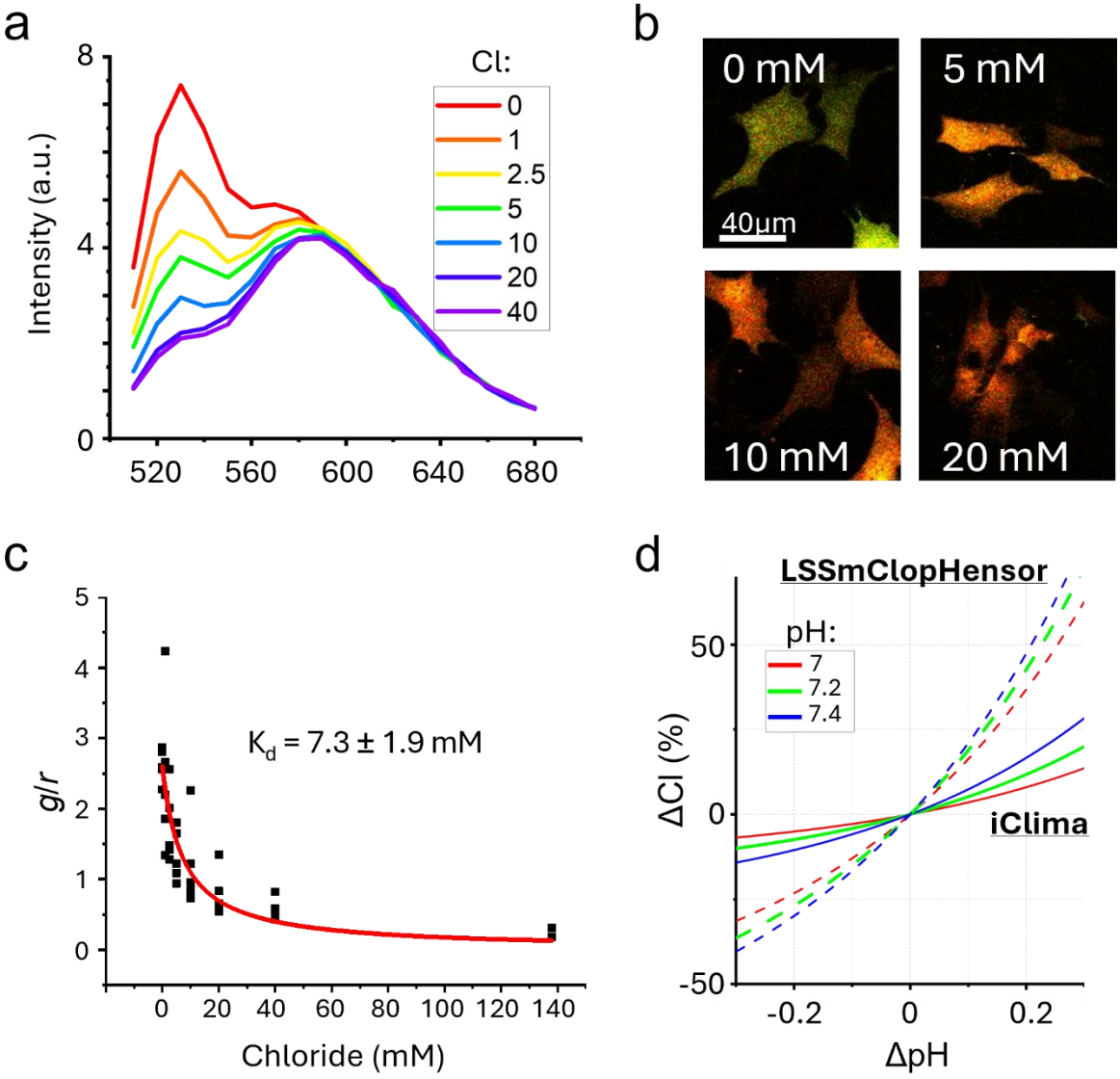

Figure 15: Chloride calibration of iClima. a) iClima emission spectra at increasing chloride concentration (excitation wavelength = 480nm). **b)** 2-Photon imaging of MEF cells expressing iClima at increasing $[Cl^-]_i$ displaying a decrease in green fluorescence. **c)** Fit of *g/r* as a function of $[Cl^-]$ using Eq 6, from which K_d is extracted. Individual points display the average values of a single well. **d)** Error of the $[Cl^-]_i$ measure as a

function of the error on pH. iClima (solid lines) displays a far weaker dependency on pH compared with LSSmClopHensor (dashed lines). Plot was generated considering Eq. 5.

3.4.2 iClima detects circadian fluctuations of chloride in U2-OS cells

After characterizing the properties of iClima, we asked whether this genetically encoded chloride sensor was sensitive enough to detect physiologically relevant intracellular chloride fluctuations. As a collaboration, I thus visited with an Erasmus+ Traineeship the laboratory of John O'Neill at the MRC Laboratory of Molecular Biology. The goals of my exchange period were: a) to determine whether a human cell line displays circadian oscillations in intracellular chloride, in synchrony with canonical circadian reporters; b) to validate iClima as a sensor capable of detecting such oscillations in real time. Given the O'Neill lab's expertise in circadian biology, this was an ideal setting to explore this question. For this purpose, two U2OS (human osteosarcoma) cell lines were used: U2OS stably expressing PER2 tagged at the C-terminus with firefly luciferase (*PER2:LUC*), and U2OS stably transduced with a lentivirus expressing firefly luciferase under a BMAL1 promoter (pBMAL:LUC) and iClima under EF1α promoter.

Cells were entrained with 12hr:12hr 37ºC:32ºC temperature cycles for five days. On day six, at the transition point between cold and warm phases, cells were replenished with low serum media and placed at constant temperature for 24 hours, under free-running conditions, before the first recording. In the case of luminescence measurements, 0.3 mM luciferin was added to the medium.

On the day of the experiment, cells were divided into three experimental groups (**Figure 16**a):

1) Bioluminescence group: recorded in an ALLIGATOR (Automated Longitudinal Luciferase Imaging Gas And Temperature-Optimized Recorder; (Zeng & O'Neill, 2022) to monitor circadian reporter activity (PER2 and BMAL1).
2) Imaging group: recorded by confocal microscopy to track chloride dynamics with iClima.
3) Elemental analysis group: subjected to Microwave Plasma–Atomic Emission Spectroscopy (MP-AES) to quantify other intracellular ion content (K^+, Mg^{2+}, Na^+, Ca^{2+}).

Chloride is poorly detectable by MP-AES because its excitation requires high energy and its emission efficiency is intrinsically low, resulting in a weak signal, making genetically encoded sensors particularly valuable for this kind of measurement. Moreover, iClima allows continuous non-invasive measurements in living cells, providing temporal resolution that bulk elemental analyses cannot achieve.

As expected, the circadian reporters *PER2:Luc* and *pBMAL1:Luc* showed anti-phasic oscillations at the beginning of the recording, with progressive amplitude damping and slight phase shifts over time. This is consistent with the well-known phenomenon of population desynchronization in cultured cells, where individual oscillators gradually lose synchrony, resulting in amplitude damping and phase instability at the population level

(Nagoshi et al., 2004; Welsh et al., 2004). Indeed, cells typically resume circadian cycling after mitosis with small phase differences, contributing to phase drift over several days. This phenomenon might be particularly strong in a cancer cell line such as U2OS, because cells might lack contact inhibition mechanisms. Data presented in **Figure 16**b-c represent the averaged traces from 12 plates for each reporter line of a 96 well plate.

For iClima, imaging was performed on four plates; the dataset derived from one of the plates was discarded from the analysis after 2 days of recording due to poor cell health. The starting number of cells analyzed was n=719. ROIs were drawn on cells and the signals in the green and red channels were averaged for each ROI. ROIs were re-drawn for each timepoint to manage putative dead cells or cell movements. The overall loss of cells during acquisition was 3.84% per day, consistent with previously reported rates in long-term live-cell imaging (Kennelly et al., 2011). Analysis of the red/green ratio revealed rhythmic oscillations that could be fitted with a damped cosine function, i.e. a cosine wave with an exponentially decreasing amplitude (see methods 5.11).The fitted period of chloride oscillations was 23.7 h (parameters: Baseline= 3.18, m=-0.0023, amplitude= 0.0169, k= $4.78*10^{-9}$, phase= 19.6 °, period= 23.7 h, p-value test= $5.2*10^{-4}$. **Figure 16**c).

Eight plates, each containing six replicate wells, were analyzed by MP-AES. Both K^+ and Mg^{2+} concentrations displayed rhythmicity, with fitted periods of 23.1 h and 23.5 h, respectively (**Figure 16**c. K^+ parameters: Baseline= 5.8 ppm, m= -0.0169, amplitude= 0.374, k= 0.0172, phase= 19.34°, period= 23.1 h, p-value test= $2.59*10^{-9}$; Mg^+ parameters: Baseline= 0.412 ppm, m= $-6.671*10^{-4}$, amplitude= 0.0094, k= $1.96*10^{-9}$, phase= 20.6 h, period= 23.5 h, p-value test= 0.00561). In contrast, Na^+ and Ca^{2+} did not display significant oscillations (data not shown). The phases of the chloride, potassium, and magnesium oscillations were closely aligned (Cl: 19.6 h, K: 19.3 h, Mg: 20.6 h), suggesting that these ions may undergo coordinated circadian regulation.

These data provide preliminary but encouraging evidence that intracellular chloride, along with potassium and magnesium, may undergo circadian oscillations in human cells. The absence of detectable Ca^{2+} oscillations is not surprising, as calcium is a tightly regulated second messenger; its signalling is typically fast, highly localized, and tightly buffered within subcellular compartments. In contrast, the lack of a clear Na^+ rhythm is more unexpected; however, it should be noted that U2OS cells are a cancer-derived line and may exhibit altered osmotic or ionic regulatory pathways, which could mask or disrupt circadian sodium oscillations. Importantly, iClima was proved capable of detecting chloride fluctuations in a physiologically relevant context. However, several limitations should be noted such as the fact that chloride data dispersion increased toward the end of the recordings, reducing robustness. This might also be influenced by ongoing cell division, which can disrupt population synchrony and contribute to increased variability in the late measurements. Moreover, circadian rhythmicity was not directly demonstrated, as we did not manipulate the circadian period pharmacologically (e.g. by lengthening with specific drugs); Finally, the use of U2OS, a cancer-derived cell line, limits the physiological interpretation of ion rhythms. Nevertheless, even if preliminary, the synchronized oscillations of Cl^-, K^+, and Mg^{2+} with ~24 h periodicity represent a strong indication that ionic homeostasis may be under circadian control in human-derived cells, and that iClima can serve as a powerful tool to investigate these dynamics in living cells.

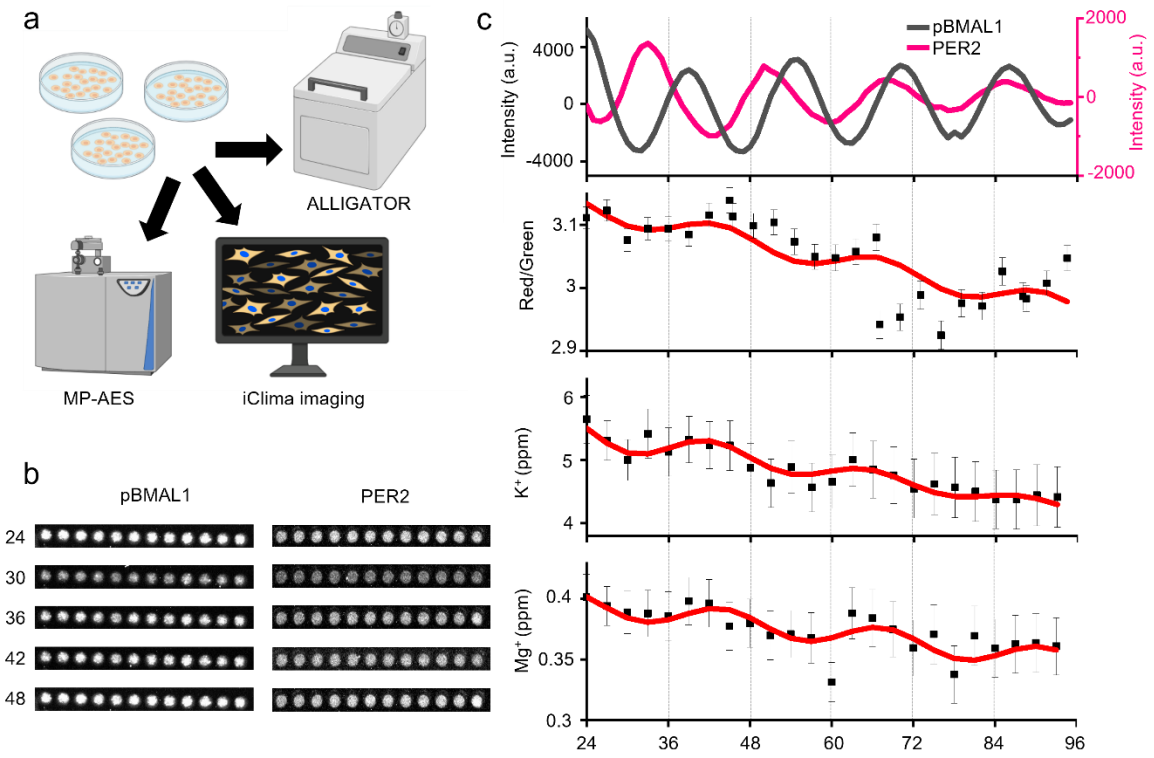

Figure 16: Circadian control of ionic homeostasis in U2OS cell. a) Schematic of the experiment. The circadian rhythm of U2OS cells was entrained with temperature cycle. Cells were subsequently subjected to different analyses to assess: circadian phase by bioluminescence, intracellular chloride by iClima imaging, and additional ions by MP-AES. **b)** Raw luminescence images of *PER2:Luc* and p*BMAL1:Luc* reporters during the first 24 h. **c)** *Top*: Average detrended luminescence profiles of *PER2:Luc* and p*BMAL1:Luc* in U2OS cells (see Methods 5.11 for detrending procedure). *Middle:* Black dots indicate the average red/green fluorescence ratio across all imaged cells (error bars = SEM); the red curve represents the fit ($p < 0.001$). *Bottom*: Black dots indicate average intracellular concentration from 8 plates of K^+ and Mg^{2+}, respectively (error bars = SEM); red curves represent their corresponding fits (K^+ $p < 0.01$, Mg^{2+} $p < 0.001$; ppm, parts per million).

3.4.3 Dynamics of $[Cl^-]_i$ during epileptic activity

After characterizing the iClima sensor *in vitro*, we next aimed to test whether the sensor was also functional *in vivo*, and specifically whether it was sensitive enough to detect large chloride transients associated with epileptic activity. To this end, we performed *in utero* electroporation (IUE) to express the sensor in cortical pyramidal neurons of V1 superficial layers as in Dal Maschio et al., 2012. Electroporation was performed using a plasmid encoding iClima under the CAG promoter, with expression specificity determined by the timing of electroporation and the position of the electrodes. Out of six pups born, four exhibited fluorescence cells, indicating successful sensor expression.

Starting from P29, mice were anesthetized with urethane for imaging sessions performed at ZT5. During the surgical preparation, an imaging window was implanted, leaving space to allow the insertion of a capillary electrode for local field potential recording. This setup enabled simultaneous two-photon imaging and LFP monitoring (**Figure 17**a). For each mouse, spectral series were acquired over multiple fields of view, resulting in the analysis of at least 30 neurons per animal (**Figure 17**b). The median baseline values measured across animals were $[Cl^-]_i$ = 6.3 mM and pH = 7.0 (**Figure 17**c). To test whether iClima

could report large chloride fluctuations during epileptic events, seizures were pharmacologically induced by local administration of 4-aminopyridine (4-AP) and VU0463271 at mid-day. VU0463271 is a selective blocker of the KCC2 cotransporter, which causes a moderate elevation of $[Cl^-]_i$ in cortical neurons. When combined with 4-AP, this condition reliably induces seizure activity at this circadian timepoint (Pracucci et al., 2023). Neural activity was monitored through simultaneous LFP recordings and two-photon imaging at a single excitation wavelength (sensor's isosbestic point), allowing correlation of optical signals with electrophysiological activity. Of the four fluorescent mice, one died during the early phases of the experiment; therefore, only three mice were included in the subsequent seizure analysis. During epileptic episodes, clearly visible in the electrophysiological traces, the green fluorescence signal showed a marked decrease (**Figure 18**a-b), consistent with a rise in intracellular chloride concentration. This signal recovered after the seizure terminated. Closer inspection of individual seizure events revealed that $[Cl^-]_i$ reached values up to ≈40 mM, calculated assuming a stable pH (**Figure 18**c). To quantify the kinetics of chloride transients, the green/red fluorescence ratio was extracted for each imaged neuron around the onset and offset of seizures. Averaged traces were then fitted with a logistic function for the rising phase and a single exponential function for the decay. From these fits, we estimated a half-rise time of t = 2.6 s and a decay time constant (τ) of 18 s (**Figure 18**d).

These experiments demonstrate that iClima is functional *in vivo*, allowing not only the measurement of absolute intracellular chloride concentration but also the temporal dynamics of chloride changes during pathophysiological events. In particular, during epileptic seizures, we observed a robust and transient accumulation of intracellular chloride, followed by a gradual recovery. iClima thus proves to be a powerful tool for monitoring both the amplitude and the kinetics of chloride transients in living brain tissue.

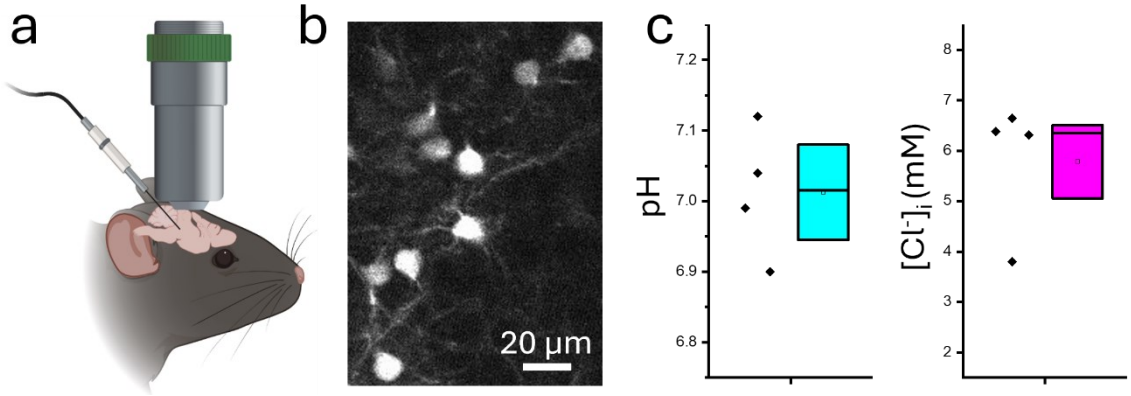

Figure 17: Chloride measures in IUE mice. a) Schematic representation of the experiment: simultaneous LFP and 2-photon imaging was performed in anesthetized mice expressing iClima in pyramidal neurons. Generated with Biorender. **b)** Representative imaging field. **c)** Cumulative pH (*left*) and chloride (*right*) results. Each symbol represents the median pH and $[Cl^-]_i$ for each experimental mouse. For each mouse we measured $[Cl^-]_i$ in a variable number of cells dependent on the quality of the sensor transfection (n: 34, 30, 43, 59).

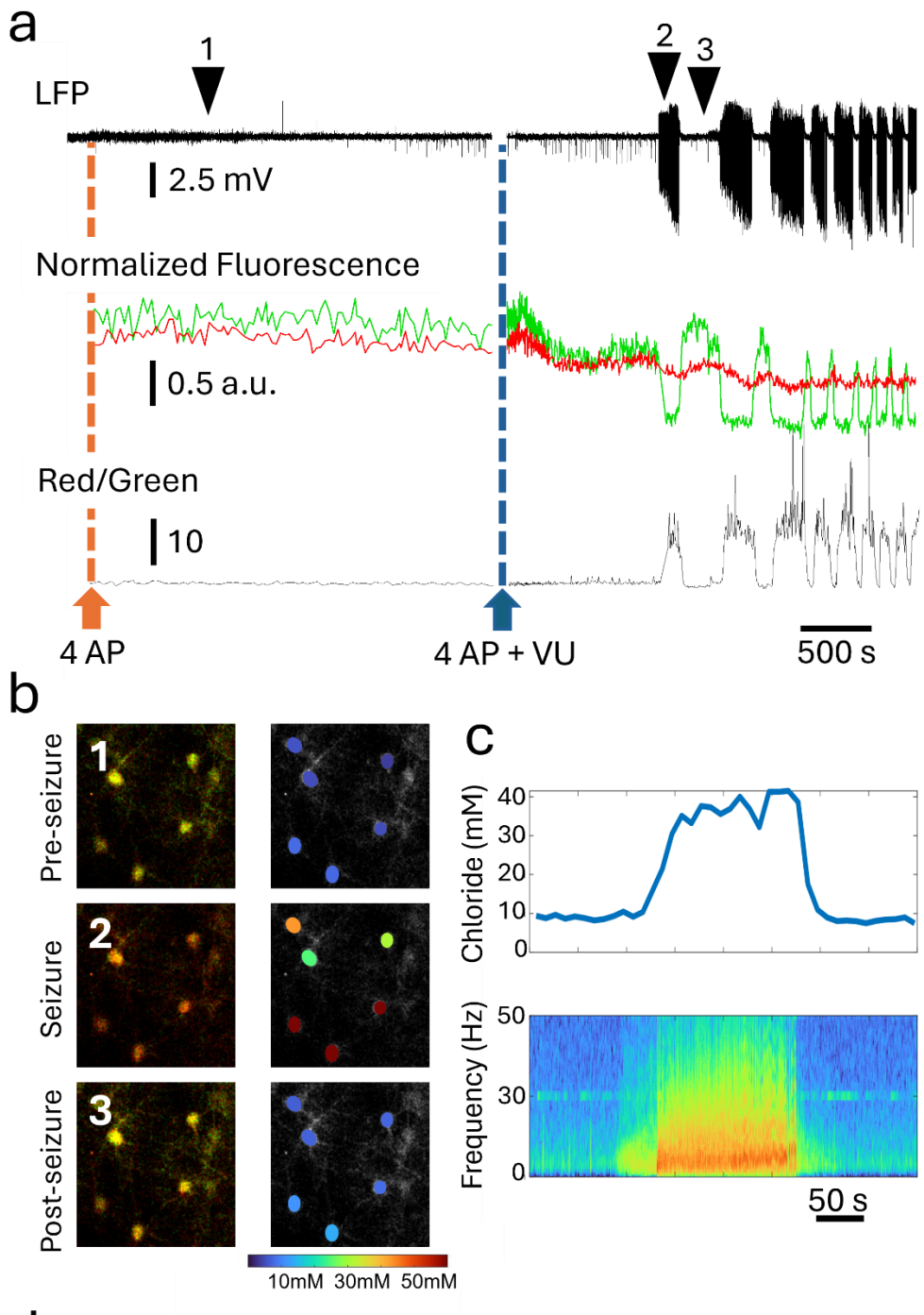
a
1
2
3
LFP
2.5 mV
Normalized Fluorescence
0.5 a.u.
Red/Green
10
4 AP
4 AP + VU
500 s
b
Pre-seizure
Seizure
Post-seizure
1
2
3
10mM 30mM 50mM
c
Chloride (mM)
40
30
20
10
0
Frequency (Hz)
50
30
0
50 s
d
Seizure onset
Green/Red
0
0.2
0.4
t=2.6 s
-20 -10 0 10 20
Time (s)
Seizure end
0
0.2
τ= 18.0s
-20 -10 0 10 20
Time (s)

Figure 18: Dynamic of an epileptic seizure studied with iClima. a) A representative recording shows several ictal events that were detected both in the LFP recording and by imaging. $[Cl^-]_i$ rapidly increases during each seizure as shown by the increase of the green/red ratio. **b)** *Left*, imaging at the isosbestic point of the timeframes indicated in 'a' (top, baseline; middle, epileptic seizure; bottom, post-seizure). *Right*, same as the left with color coded estimates of $[Cl^-]_i$ values. **c)** Zoom-in of an ictal event showing the relationship between the $[Cl^-]_i$ changes (*top*) and the LFP spectrogram (*bottom*). **d)** Zoom-in of pyramidal chloride dynamics (gray curves) during seizure onsets and seizure ends. The median behavior was fitted (red curve) and time constants were shown.

3.4.4 iClima detects evoked chloride transients elicited by visual stimulation

Understanding the spatiotemporal dynamics of inhibitory signalling in the visual cortex is essential for deciphering how sensory processing is regulated *in vivo*. Although inhibition plays a key role in shaping excitatory responses, direct measurement of inhibitory postsynaptic events *in vivo*, particularly during physiological activity, has remained challenging. To address this, we used iClima, to monitor chloride transients in layer 2/3 pyramidal neurons of the primary visual cortex of awake and anesthetized mice during visual stimulation. Our goal was twofold: (1) to determine whether inhibitory responses could be reliably detected *in vivo* with this approach, and (2) to characterize the temporal profile of these responses to different visual stimulation under different physiological states.

A total of 11 mice were transfected with iClima and implanted with chronic cranial windows over V1. Mice were then handled daily and subsequently habituated to head-fixation on the imaging setup (a custom wheel under the two-photon microscope). Following habituation, each mouse underwent multiple imaging sessions under different experimental conditions: daytime (around midday) vs nighttime (around midnight), and either in the awake, head-fixed condition or under light isoflurane anesthesia. During awake imaging, mice were free to locomote on the wheel. During anesthetized recordings, mice body temperature was maintained with a heating pad. Within each imaging session, visual stimuli were presented multiple times (typically 10 repetitions, minimum 5). Not all mice were recorded in all combinations of condition (day/night × awake/anesthetized); inclusion of data was evaluated on a per-animal, per-session basis.

The primary stimulus used for this analysis was a full-field luminance step: after a baseline dark screen, the display was switched to a bright uniform luminance for 20 s, followed by a return to darkness. This paradigm is known to evoke strong excitatory and inhibitory responses in V1 neurons, with inhibitory components often peaking shortly after stimulus onset (Tucker & Fitzpatrick, 2006). Using iClima, we observed clear chloride transients in CaMKII-positive neurons, indicating net inhibitory drive at both stimulus onset and offset (**Figure 19**a), with an average peak reaching 2.31% in the onset and 1.17% in the offset response. Strikingly, these inhibitory responses could be detected robustly across animals, representing, to our knowledge, the first demonstrations of *in vivo* chloride imaging of visually evoked inhibition with a physiological stimulus. Interestingly, although the 2.31 % peak change might appear small, it corresponds (assuming a cytosolic pH of 7.4) to an estimated chloride load of approximately 370 µM entering the cell (see methods

5.13). Such a modest increase is physiologically plausible given that the stimulus is naturalistic, and highlights the sensitivity of iClima in resolving small fluctuations of intracellular chloride within the physiological range for the first time.

Quantitative analysis of the peak amplitudes and their latencies revealed no significant differences between recordings performed at midday and those performed at midnight, either in the awake or anesthetized state (Mann-Whitney tests not significant). This allowed me to pool all daytime and nighttime data within each physiological condition (awake/isoflurane) (**Figure 19**b). Considering all pooled awake and isoflurane sessions, we then measured the amplitude of the responses at stimulus onset and offset (**Figure 19**c). No significant difference was observed between the onset peak amplitudes when comparing awake and anaesthetized groups (Mann–Whitney test, p=0.27). However, a significant difference emerged between the offset peaks in the two conditions, with awake animals showing a larger response comparing to isoflurane (one-tailed Mann–Whitney test, awake > isoflurane: p = 0.0089). Furthermore, within each condition, the offset peak was consistently smaller than the onset peak (one-tailed Mann–Whitney test, awake: p = 0.0049; isoflurane: p = 0.01016). In addition, no significant difference was found between the latencies of the onset and offset peaks, which occurred with an average of 3.5 s and 2.8 s, respectively (Mann–Whitney test, p=0.06869). Together, these results suggest that the onset-evoked chloride response is more stereotyped and robust across brain states, as it remains comparable between awake and anesthetized conditions. In contrast, the offset response appears less stable and more state-dependent, as it is strongly attenuated under isoflurane anesthesia. Additionally, when present, the offset peak consistently reaches a lower amplitude than the onset peak, indicating that stimulus offset drives a weaker inhibitory response compared to stimulus onset.

To further characterize the population response decay, the average awake and isoflurane-anesthetized sessions were then fitted for the ON- and OFF-responses using a single-exponential model, with the constraint that the signal must return to the pre-stimulus baseline (0%). Under awake conditions, the two time-constants were comparable (τ_{ON}=6.58 s, τ_{OFF}=4.08 s), whereas under isoflurane anesthesia, the ON-response recovery was substantially slower (τ_{ON}=12.4, τ_{OFF}=5.0s). Isoflurane is known to prolong $GABA_A$-mediated IPSCs and to enhance tonic inhibition by increasing activation of extrasynaptic receptors (Jia et al., 2008; M. V. Jones & Harrison, 1993). Such a persistent tonic drive during the stimulus might result in residual inhibitory input that slows the return toward baseline. To verify whether this apparent slowing of recovery was driven by a true change in kinetics or by a shift in the steady-state level, we repeated the fit using a model with a free asymptote. Remarkably, with this approach the fitted time constant for the isoflurane ON-response became comparable to the OFF-response and to awake conditions (τ_{ON}=4.94 s), whereas the fitted steady-state limit was significantly shifted compared to baseline (fitted asymptote: -0.53%). Importantly, fitting with a free asymptote in awake mice had only a minor effect, resulting in a τ_{ON} of 6.58 s and an asymptote very close to baseline (−0.12%). This result suggests that under isoflurane, the recovery kinetics per se are not slower, but the system converges toward a new steady state during the stimulus period. This is consistent with the known effects of isoflurane, which enhances tonic inhibition by activating extrasynaptic $GABA_A$ receptors. Such sustained inhibitory drive could maintain elevated intracellular chloride levels during the stimulus,

effectively shifting the equilibrium potential and resulting in a non-zero asymptote, without altering the intrinsic time constant of chloride extrusion.

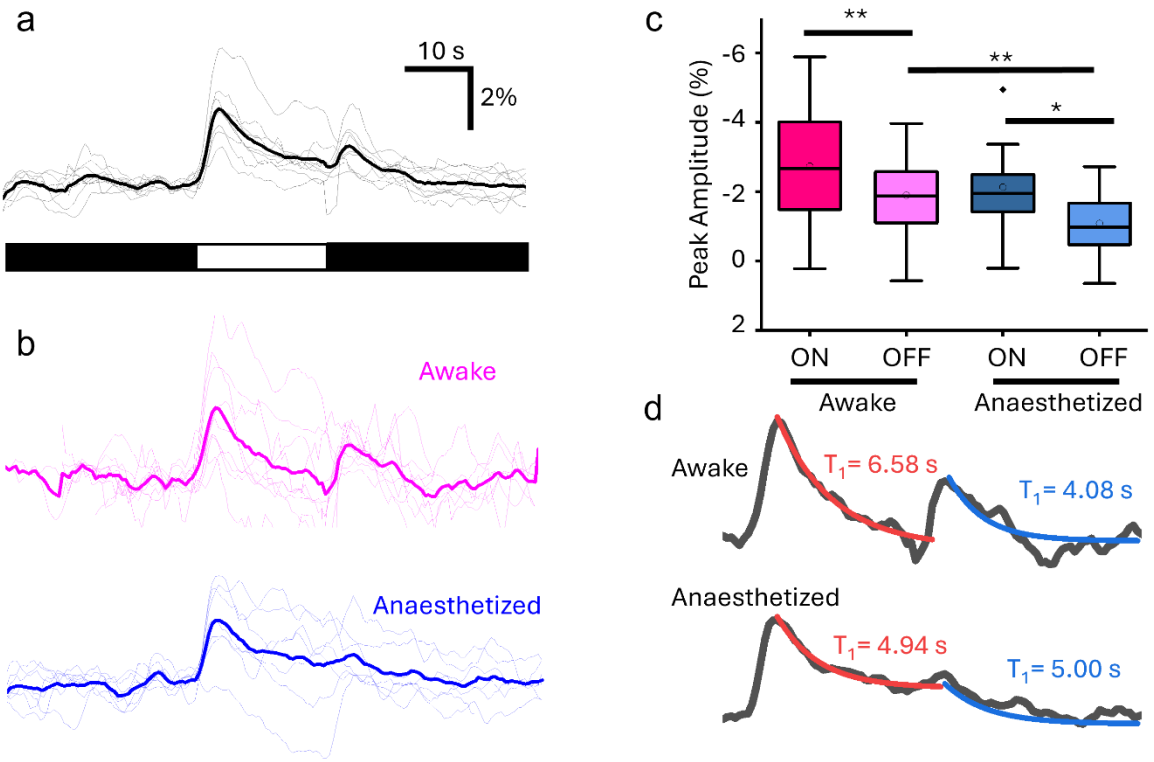

Figure 19: Chloride responses to step of light. a) Average chloride response of pyramidal cells (CaMKII$^+$) to a step of light lasting 20s. Thick line, average across mice. Thin lines are average of multiple recording sessions and multiple cells of single mice. Below, schematic represents the light evolution of the screen. **b)** Average chloride response of the awake-mouse (above) and isoflurane anesthetized-mouse sessions (thick line). Thin lines represent the average of multiple cells in each experimental session. Scalebar is the same of fig. a). **c)** Chloride peak amplitude detected after the onset and offset of the light step. **d)** Exponential decay fit of the average chloride response in the awake (above) and anaesthetized (below) animals. Red lines represent the on-response decay fit while the off responses are fitted by the blue lines. Decay times of the fit are shown.

In addition to the full-field luminance step, we presented a drifting horizontal grating stimulus to a subset of mice. In this paradigm, the display was first set to a uniform gray background, followed by the presentation of a high-contrast (circa 100%) horizontal grating drifting continuously for 5 s, with its mean luminance matched to the gray baseline. Strikingly, all animals that were shown the drifting grating (10/10) exhibited clear inhibitory responses, with an average peak of 2.48% that occurred at approximately 3 s after stimulus onset (**Figure 20**a). The magnitude of this response is comparable to that observed with the luminance step paradigm, further supporting the sensitivity of iClima to detect small, transient fluctuations of intracellular chloride *in vivo*.

As with the luminance step, the peak amplitude and latency were quantified across animals. No significant differences emerged between day and night recordings within either physiological condition (awake or anesthetized; Mann–Whitney tests, n.s.), which allowed pooling of data across time-of-day for each state. When comparing awake and

anesthetized animals, a clear difference was observed in peak latency: under isoflurane, the population peak occurred earlier (mean peak time = 2.5 s) compared to awake animals (mean peak time = 4.5 s; **Figure 20**b). In contrast, peak amplitudes were similar across groups, although awake animals displayed a slightly higher response (mean peak amplitude = 2.94% vs. 2.51% under isoflurane). We next characterized the recovery phase following stimulus offset by fitting the population-averaged traces with a single-exponential decay model including a free asymptote. Under awake conditions, the fitted time constant was τ = 6.1 s, consistent with the step-evoked responses. Under isoflurane anesthesia, the recovery was slightly slower (τ= 9.5 s), consistent with prolonged chloride clearance. Taken together, these results suggest that isoflurane anesthesia not only modulates the strength of inhibitory drive but also alters the temporal dynamics of visually evoked responses. The earlier peak latency under isoflurane may reflect facilitated activation of $GABA_A$ receptor, which has been shown to occur at lower agonist concentrations in the presence of volatile anaesthetics (Franks & Lieb, 1994). The slower recovery phase, in turn, may result from the well-documented effect of isoflurane to prolong $GABA_A$ channel open times and enhance tonic inhibition through extrasynaptic receptor activation (Jia et al., 2008). Together, these effects may shift the network toward a more strongly inhibited state, resulting in an earlier onset of inhibitory responses and a more prolonged return to baseline.

In the case of the 5-s drifting grid stimulus, we noticed that the rising phase of the response often peaked surprisingly late relative to stimulus onset, with some animals showing peaks even after stimulus offset. This observation raised the possibility that the 5-s stimulus duration might be too short to fully capture the kinetics of the chloride transient. To better resolve the temporal profile of the inhibitory response, we extended the grid duration to 10 s while maintaining identical luminance and contrast conditions. As for the previous paradigms, no significant differences were found between recordings performed at midday and those performed at midnight, either in the awake or isoflurane condition (Mann–Whitney tests not significant). Consequently, daytime and nighttime data were pooled within each physiological state. Under this 10-s stimulation, the population average again exhibited a robust inhibitory response, with a mean peak amplitude of 1.98 % and a latency of 4.5 s from stimulus onset (**Figure 20**c). The longer stimulus duration allowed us to more accurately follow the evolution of the response over time. Interestingly, rather than displaying a simple exponential decay immediately after the peak, as observed for both the flash and the 5-s grid paradigms, the 10-s grid responses showed a plateau phase that persisted for several seconds before gradually returning toward baseline. This plateau suggests that, under sustained visual drive, inhibitory signalling may reach a quasi-steady state before chloride extrusion mechanisms re-establish baseline levels.

Beyond these findings, the use of iClima also enabled imaging with improved temporal resolution. All recordings described so far were acquired with a time resolution of 2 frames per second. However, by restricting the acquisition to a smaller portion of the field of view (**Figure 20**e), we were able to achieve a frame rate of 30 Hz. Reaching this temporal resolution allows the frame rate to exceed the characteristic timescale of the 5-s drifting grating response, effectively oversampling it and better resolving the kinetics of the sensor’s response. This oversampling enables averaging of the response over multiple frames, which in turn reduces noise and improves the signal-to-noise ratio. From this

recordings, distinct responses to the visual stimulus were observed in both the cells within the imaged field (**Figure 20**f). This demonstrates that iClima can discriminate inhibitory activity across different pyramidal neurons within the same imaging plane and, in principle, provides the capability to resolve inhibitory signaling at the single-cell and single-trial level.

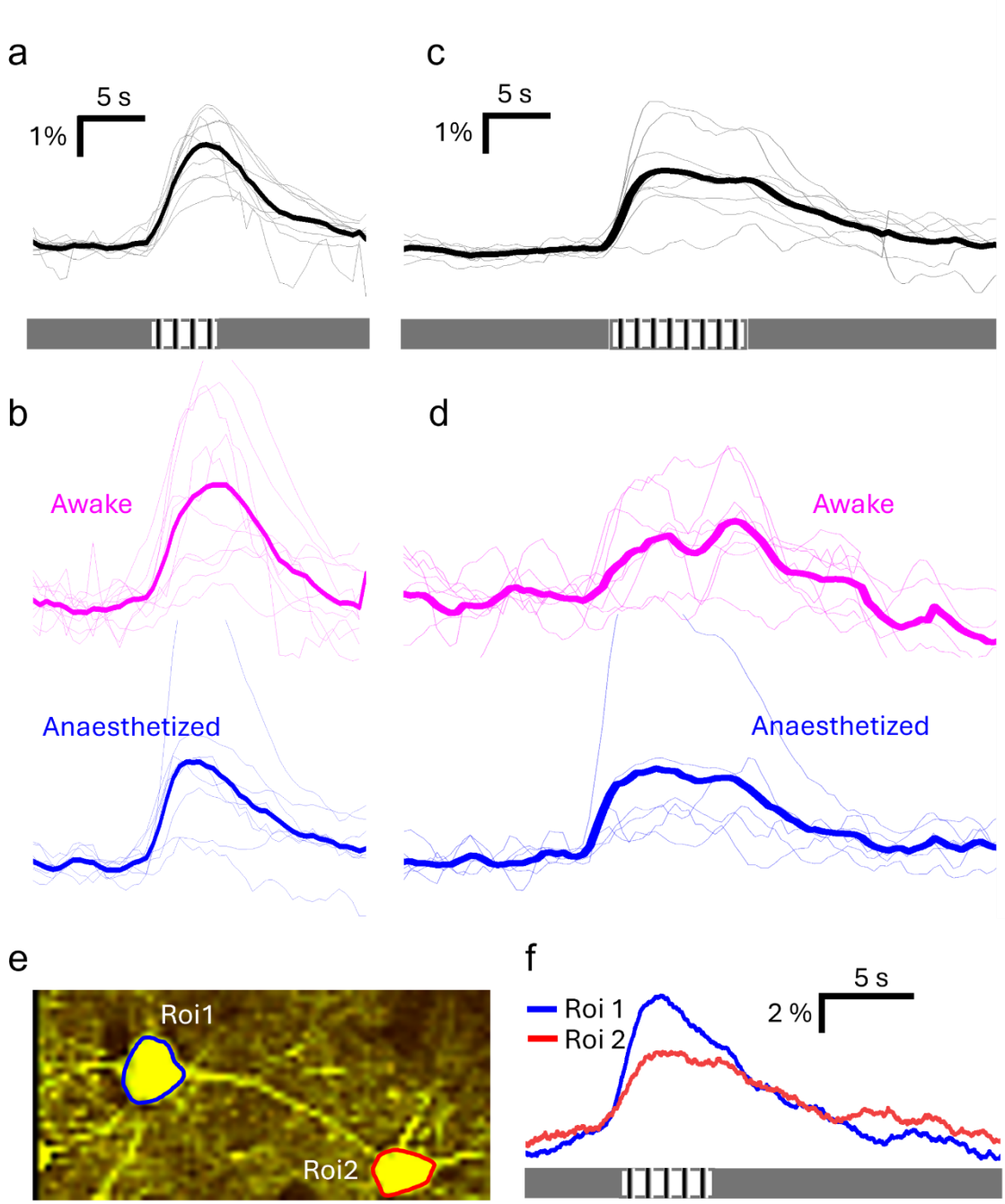

Figure 20: Chloride responses to grid. a) and c) Average chloride response of pyramidal cells (CaMKII$^+$) to a moving grid lasting 5 s (figure a) and 10 s (figure c). Thick line, average across mice. Thin lines are average of multiple recording sessions and multiple cells of single mice. Schematic represents the light evolution of the screen. **b) and d)** Average chloride response of the awake-mouse (above) and isoflurane anesthetized-mouse sessions (thick lines) for the 5 s (figure b) and 10 s (figure d) gratings. Thin lines are average of multiple recording sessions and multiple cells of single mice. Scalebar is the same as figure a and c. **e)** Average projection (30 Hz time series) of a field of view where 2 ROIs are depicted. **f)** Representative Cl^- transients in response to a single grid presentation in the two cells as indicated in e.

3.4.4.1 Validation of stimulus-evoked iClima signals

To further validate that the signals observed with iClima truly reflect visually driven neuronal responses a series of control experiments were carried out. A first potential concern is that photons from the stimulation screen could directly enter the microscope's optical path, thereby contaminating the detected fluorescence signal. In theory, this could happen if light from the stimulus monitor bypassed the sample and reached the detectors. We know that such contamination can indeed occur. To get rid of this contamination, we record movies under identical stimulation conditions but with the laser turned off, and then subtract this "dark" movie from the imaging data. However, this approach relies on the assumption that the contamination measured in the dark movie is sufficiently similar to that occurring during actual imaging. To ensure that the dark correction we apply is sufficient, we repeated the visual stimulation protocol under identical screen conditions in presence of an optomechanical "hard shutter" located in the laser path upstream of the microscope entrance. The shutter was controlled by an Arduino board and was alternately opened and closed on a frame-by-frame basis, such that every second frame was acquired with the laser completely blocked ("dark frame") (**Figure 21**a). This acquisition scheme provided two key advantages. First, it allowed us to subtract the true, frame-by-frame dark signal from each ROI during the experiment itself, rather than relying on separate dark recordings obtained before or after the real acquisition. Second, it enabled us to directly analyze the dark frames themselves and estimate the extent to which light contamination from the stimulus display could, in principle, affect the ratiometric signal.

Visual stimulation consisted of an equiluminant gray screen followed by five repetitions of a 5-s drifting grid (100 % contrast) interleaved with 3-s gray periods, for a total of 40 s of stimulation, followed by a post-stimulus recovery epoch. ROIs were manually drawn around pyramidal cell somata, and for each ROI the corresponding dark frame signal was subtracted on a frame-by-frame basis (**Figure 21**b). Even after this correction, which explicitly removed any contribution from light leakage, the average responses to visual stimulation remained robust (**Figure 21**c). This result strongly suggests that the observed fluorescence changes are not due to contaminating photons but rather reflect a biologically driven change in intracellular chloride. Importantly, this subtraction was ROI-specific and thus preserved the "spatial" pattern of the correction (note that, with scanning microscopy, a spatial pattern is actually a temporal pattern), further minimizing the possibility of residual artifacts.

Next, we asked to what extent could this contaminating light affect our measurement, under the assumption that no chloride dependent change in fluorescence happens in our neurons. To quantify this, we generated artificial time series for each cell and each channel as the sum of a constant F and a time series D(t). F is the baseline fluorescence measured for a cell ROI in one of the two channels, which in our assumption is constant (no chloride dependent signal). D(t) is the time series for the same cell ROI in absence of 2P excitation (the so called "dark"). These artificial traces therefore represent the fluorescence signal that would be expected if the only source of change were fluctuations in the dark signal. Analysis of these artificial cells revealed extremely small $\Delta R/R_0$ responses compared to the real response (**Figure 21**d). Moreover, the temporal profile of these signals was completely different to the responses observed in real cells.

Finally, to exclude other potential confounding such as motion artifacts or hemodynamic responses, we repeated the 5-s grid stimulation protocol in a separate cohort of mice expressing LSSmClopHensor, a ratiometric sensor with a much lower sensitivity to intracellular chloride compared to iClima. Imaging was performed at the respective isosbestic point for each sensor to limit pH dependency of the measure. Analysis of 121 ROIs from iClima-expressing neurons confirmed the presence of a robust peak response, whereas 149 ROIs from LSSmClopHensor-expressing neurons showed no significant response (**Figure 21**f-g). Together, these results strongly support the interpretation that the responses measured with iClima represent true, stimulus-evoked chloride transients rather than optical or hemodynamic artifacts. This data also demonstrates the large increase of sensitivity provided by iClima compared with the previous state-of-the-art sensor.

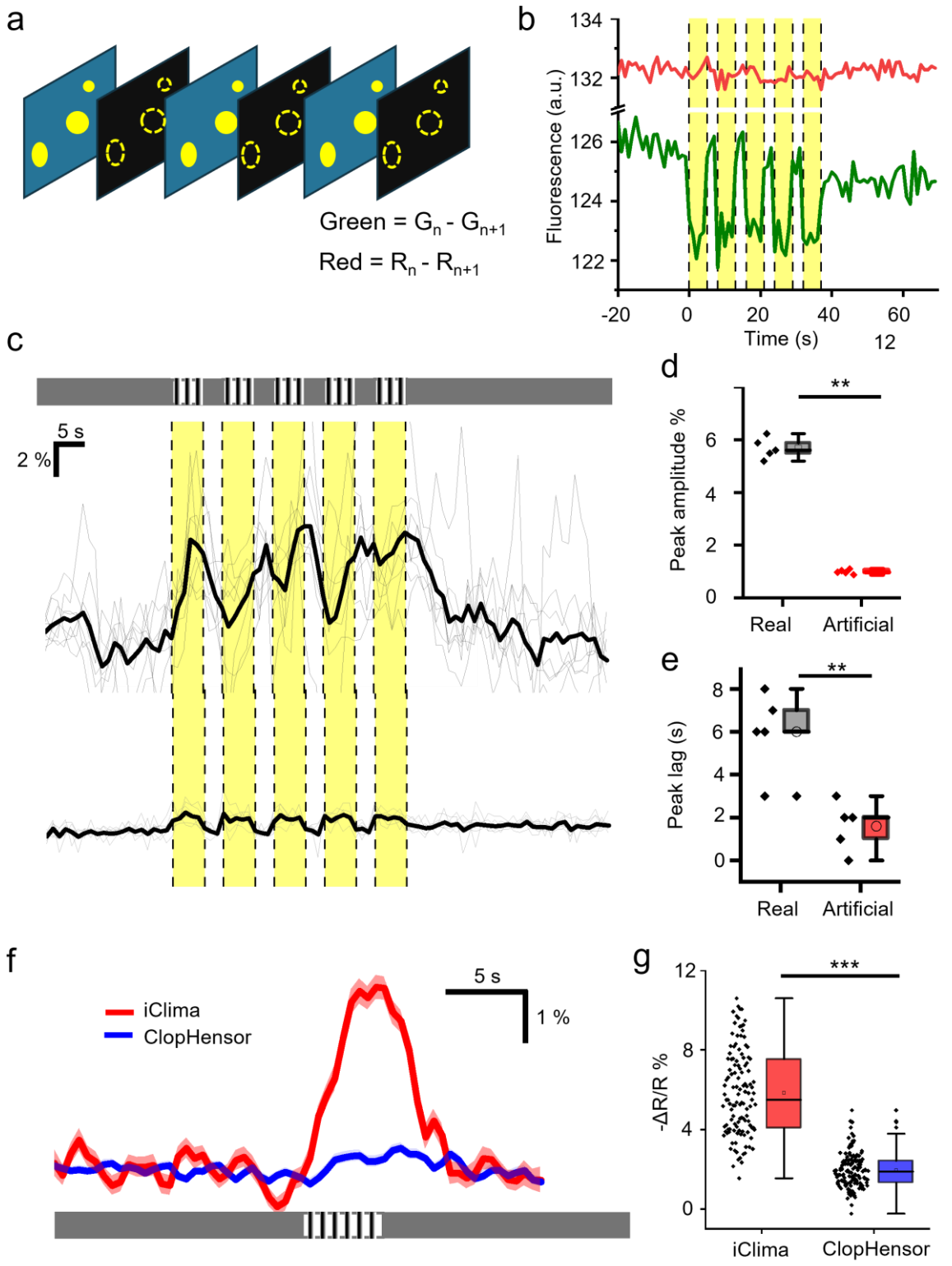

Figure 21: Control experiments confirming the specificity of visually evoked iClima signals. a) Schematic of the acquisition protocol used to cope with potential light contamination from the visual display. A mechanical shutter was inserted in the excitation laser path and alternately opened or closed on a frame-by-frame basis, yielding interleaved "light" and "dark" frames. **b)** Representative dark traces (red and green channels) of a ROI during visual stimulation (yellow shading). The dark-frame signal was subtracted on a per-ROI basis frame by frame. **c)** Population-averaged $\Delta R/R_0$ responses (thick line, mean; thin lines, trials) to five repetitions of a 5-s drifting grating stimulus after dark-frame subtraction. *Above*: real cells. *Below*: "artificial" cells. The persistence of robust visually evoked responses demonstrates that detected signals are not due to stray light from the stimulus monitor. **d) and e)** Comparison of the peak amplitude (Figure d) and peak lag

(Figure e) between real cells and artificial cells. **f) and g)** Comparison between responses recorded in iClima- and LSSmClopHensor-expressing neurons under identical visual stimulation. While iClima-expressing neurons (red) exhibited significant visually evoked chloride responses, LSSmClopHensor controls (blue) showed no detectable signal changes. Box plots summarize peak $\Delta R/R_0$ values across all ROIs.

3.4.5 Locomotion correlates with Cl^- transients in visual cortex

As described in the previous chapter, a subset of experiments were conducted awake, head-fixed mice positioned on a freely rotating wheel under the two-photon microscope (**Figure 22**a). The awake animals could move spontaneously while neural activity was continuously monitored. This opened the possibility to explore how locomotion influences intracellular chloride concentration and thus, cortical inhibitory dynamics. Indeed, previous studies have shown that inhibitory activity in visual cortex is strongly modulated by locomotion (see Introduction 2.2.5.1). Thus, we expect that $[Cl^-]_i$ dynamics in pyramidal neurons might provide a new layer of detail on the role of inhibition in visuo-motor integration.

To test this hypothesis, the previously recorded two-photon imaging data were analyzed, focusing specifically on spontaneous transitions between stationary and running states. Segments of recordings in which no visual stimulus was presented were selected, to isolate locomotion effects. The dataset included recordings from 11 different mice that met the quality and behavioural criteria described below. Two distinct classes of events were identified. In the first, the animal remained stationary for at least 10 s before initiating running for at least 4 s. In the second class, the animal had been running for at least 10 s and then stopped, remaining still for at least another 10 s. Speed and chloride ratio traces were aligned on the transitions, namely time = 0s.

When the mouse started running, we observed a rise of intracellular Cl^- concentration in pyramidal neurons (**Figure 22**c). The average signal reached its peak 3 s after locomotion onset, with an average amplitude of $\Delta R/R_0$ about 4.3%, that supposing a pH of 7.2 is equivalent to a physiological chloride entry of ~1 mM (see methods 5.13). This finding is in line with the well-established increase in inhibitory activity during locomotion in visual cortex (see introduction 2.2.5.1). When locomotion ceased, the chloride signal gradually returned to baseline levels (**Figure 22**d). The decay phase could be well described by an exponential function with τ = 4.6 s. Interestingly, the time constant obtained here is comparable to the recovery time observed after visually evoked Cl^- responses, suggesting that both locomotion- and stimulus-driven chloride dynamics share mechanisms of homeostatic regulation. Only the offset transitions allowed for reliable fitting, since, by definition, the mouse remained still for at least ten seconds after stopping, ensuring a stable post-locomotion baseline.

To understand whether the chloride responses elicited by visual stimulation and locomotion are additive, we next analysed trials in which grids were presented. Each trial was classified according to the animal's behavioural state during the period surrounding stimulus onset. They were labelled as *runnig* when the mouse's speed exceeded 1 cm/s for at least 80% of the time within a six-second window centred on the stimulus onset

(from –3 to +3 s). *Not-runnig* trials were defined as those in which the mouse remained below this threshold for the entire period extending from 10 s before to 10 s after the stimulus. All trials form the same session were normalised to a common baseline calculated exclusively from not-running periods. As expected, the traces corresponding to running trials displayed a higher pre-stimulus baseline (3.4 %) than those recorded during *non-running* periods, indicating that locomotion alone increases intracellular chloride. Despite this difference in baseline, both conditions showed comparable stimulus-evoked transients when their respective baselines were subtracted: in both cases, the visually evoked chloride response had a similar amplitude with a peak-to-baseline difference of 2.3% in the not-running and 2.8% in the running trials (**Figure 22**d).The data therefore suggest a linear summation between the two processes.

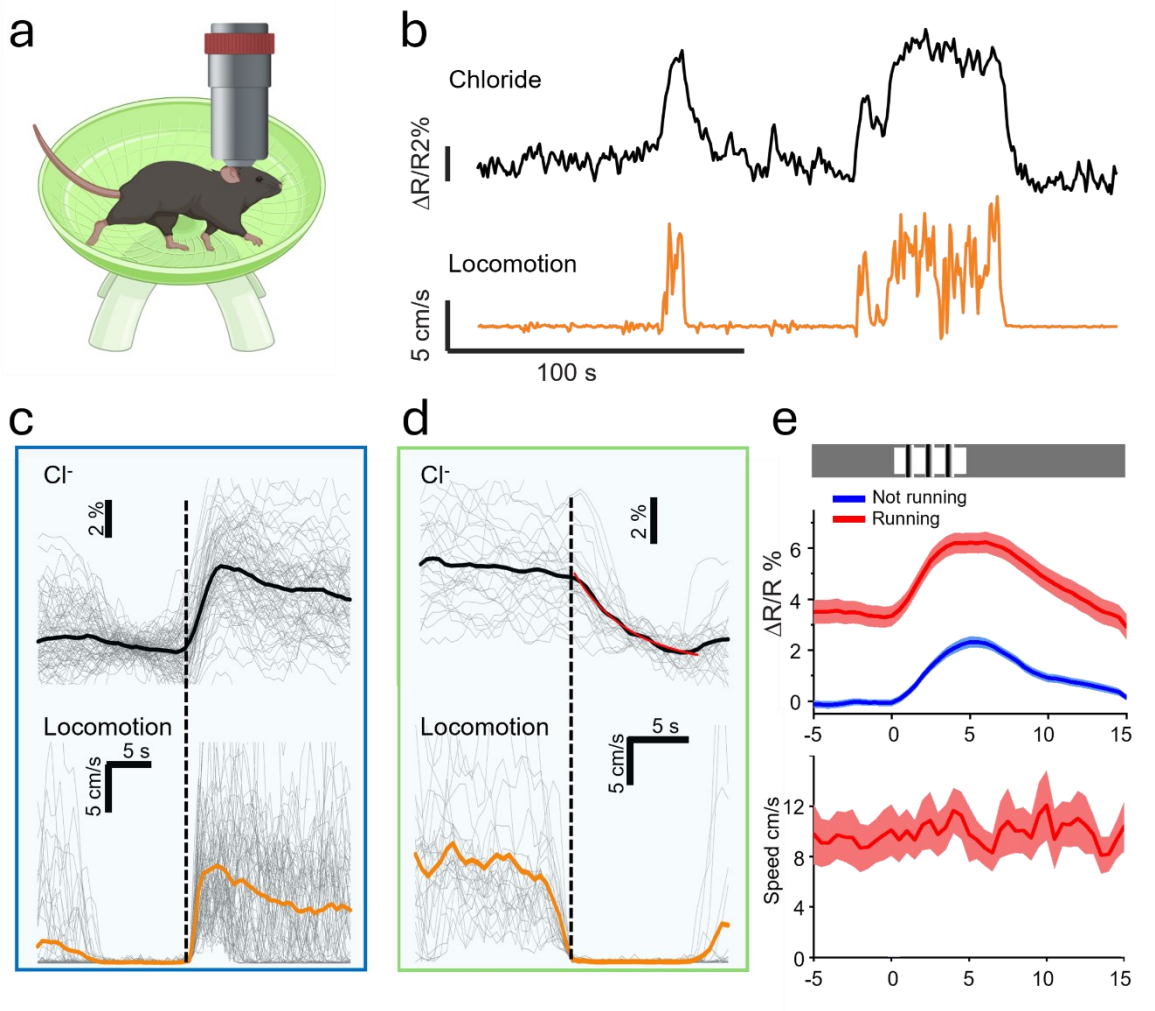

Figure 22: **Locomotion induce Cl^- transients. a)** Illustration of the experimental conditions: the mouse could freely walk over the wheel under the microscope. **b)** Comparison between Cl^- transients (black, top) and locomotion (orange, bottom). **c)** Kinetic of the Cl^- transients (*Top*) in correspondence of the start of movement (*Bottom*). Gray traces, single trials. Bold curves, averages. **d)** Same ad in c, representing the end of movement. Cl^- recovery was fitted with an exponential decay function, shown in red. **e)** *Top,* Comparison between grating-induced Cl^- transients in trials when animals were running and not-running for the whole length of the trace. *Bottom,* Locomotion average in the same trials (the blue curve is shown but flat to zero values). Bold curves, averages. Shaded areas, standard deviations.

3.4.6 The onset of Cl^- transients integrates gamma activity

To investigate how inhibitory activity contributes to visually evoked chloride transients in pyramidal neurons, we performed *in vivo* electrophysiological recordings in urethane-anesthetized mice (n = 6). Visual stimulation consisted of a step of steady light (10 cd/m², 20 s duration) presented on a dark background, identical to the protocol used in the chloride imaging experiments (**Figure 23**a). Recordings were obtained with 16-channel silicon probes (Neuronexus, single-shank, 25 µm site spacing, total span ≈ 450 µm) inserted perpendicularly into the visual cortex.

Local field potentials (LFPs) were filtered in the 20–48 Hz range to isolate low-gamma oscillations. Power in this frequency band was computed in short moving windows and normalized to baseline activity (ΔPower/Power). Visual stimulation reliably induced gamma responses at both light onset and light offset (**Figure 23**b). On average, gamma power increased by 37% at light onset and by 31% at light offset. Similar to chloride imaging experiments, the onset response was consistently larger than the offset response (**Figure 23**d-e). Response latencies did not differ significantly between onset and offset, suggesting comparable temporal dynamics. Notably, the onset gamma peak appeared more consistent across trials and animals compared to the offset response.

From the same recordings, multi-unit activity (MUA) was extracted to assess spiking responses (**Figure 23**c). Across trials and channels, the analysis of MUA revealed clear increases in firing rate following both stimulus onset and offset. These peaks in spiking activity corroborate the notion that both transitions in luminance engage cortical excitatory-inhibitory feedback. To directly compare electrophysiological and optical measurements, I compared the temporal dynamics of gamma and chloride transients. Interestingly, the rising phase of chloride accumulation closely followed the integrated gamma power in both onset and offset conditions (**Figure 23**f). This alignment suggests that inhibitory-driven gamma oscillations and chloride net flux in pyramidal neurons are temporally coupled. Given that gamma oscillations emerge from recurrent interactions between excitatory pyramidal cells and inhibitory interneurons, the data support the interpretation that chloride influx reflects interneuron-mediated inhibition underlying gamma generation.

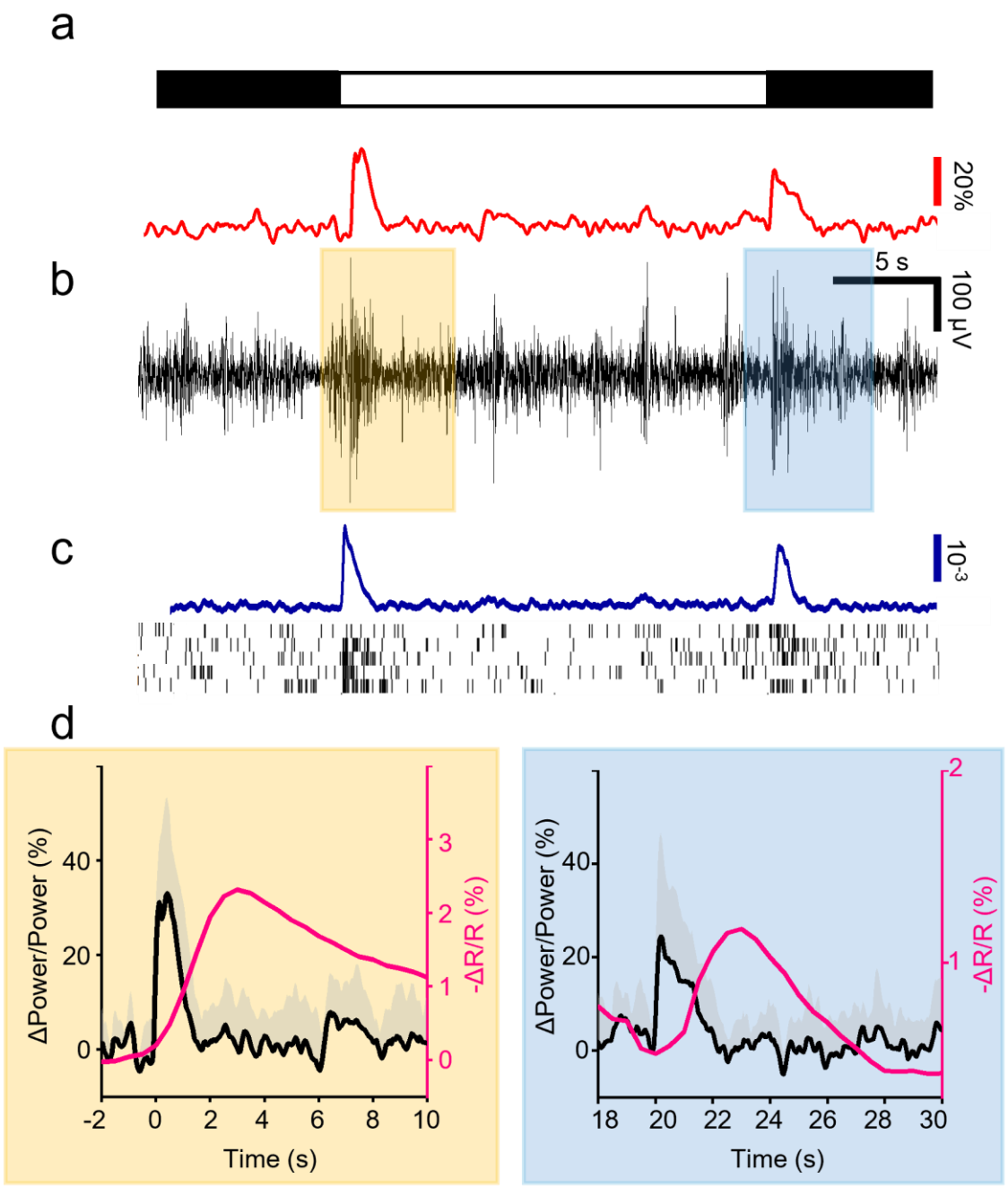
a
b
c
d
20%
5 s
100 µV
10-3
ΔPower/Power (%)
-ΔR/R (%)
Time (s)
e
Perak Amplitude (%)
On
Off
f
Onset
Offset
Normalized Activity (a.u.)
Chloride
Gamma integral
Time (s)

Figure 23: Visual-evoked electrophysiological activity correlates with chloride transients in pyramidal neurons. a) *Top:* Schematic of the visual stimulation protocol: a 20 s luminance step (10 cd/m²) presented on a dark background. *Bottom:* Average gamma power (20–48 Hz) across all trials, channels, and mice (n = 6), normalized to baseline (ΔPower/Power%). **b)** Example LFP trace from a single channel in one trial. **c)** *Top:* MUA probability, computed per mouse by summing spikes across channels and trials, then averaged across animals (blue). *Bottom:* Example MUA raster plots from one channel across 5 stimulus presentations. **d)** Relationship between gamma activity (black) and chloride transients (magenta). Black curves are the averages among different mice and shaded area indicates ±SD of gamma power (plotted above baseline only). Left: onset response; Right: offset response, corresponding to the highlighted windows in panel b. **e)** Peak gamma amplitudes for onset and offset responses across mice. On responses were significantly larger than off responses (Wilcoxon signed-rank test, $p = 0.04675$). **f)** Normalized temporal dynamics of chloride transients and integrated gamma activity. Each trace was normalized to its own peak and aligned to stimulus onset (0 s) and offset (20 s).

4. Discussion

This doctoral project, carried out over four years, focused on intracellular chloride and its contribution to cortical physiology and pathophysiology. The project was guided by two main objectives. First, to employ a previously published genetically encoded chloride sensor (LSSmClopHensor) to investigate how neuronal $[Cl^-]_i$ is modulated under different conditions. Second, to improve the sensitivity and temporal resolution of *in vivo* $[Cl^-]_i$ measurements and use this refined tool to test biophysically driven hypotheses about chloride dynamics under circadian control, during sensory and behavioural processing, and in epileptiform states.

From results previously obtained in our lab, we knew that $[Cl^-]_i$ follows a diurnal cycle in pyramidal neurons, being “low” during the resting/light phase (ZT5) and “high” during the active/dark phase (ZT17) (Pracucci et al., 2023). An independent study performed in Oxford at the same time of our study suggested that the night shift of $[Cl^-]_i$ is due to the increased activity during the active phase (Alfonsa et al., 2023). To test if the shift in $[Cl^-]_i$ we measured is activity dependent, I used LSSmClopHensor to monitor the effect of 4h prolonged darkness on neuronal $[Cl^-]_i$ at ZT5. Despite higher locomotor activity in prolonged darkness, $[Cl^-]_i$ remained comparable to ZT5 time point and significantly lower than at the nominal night point. This data supports, but are not a proof, of a primarily circadian control of $[Cl^-]_i$ and argues against a trivial dependence of $[Cl^-]_i$ on acute light or sleep per se. Our result enters an active debate, because other studies (Alfonsa et al., 2023, 2025) reported a primary dependence of $[Cl^-]_i$ on sleep state rather than on circadian phase. Methodological differences are likely relevant here. Indeed, Alfonsa et al. subjected animals to a more intrusive behavioural manipulations (i.e. active manipulation to prevent sleep), condition that can introduce stress. Moreover, many experiments of Alfonsa et al. were performed *ex vivo*. In contrast, our approach relied on *in vivo* chloride measurement. Anyway, both studies converged on finding a similar daily cycle in $[Cl^-]_i$, increasing the confidence of this relevant finding.

We next examined the effect of REM sleep deprivation on pyramidal neurons of prefrontal cortex using a literature standard protocol (Mendelson et al., 1974). The data show that REM sleep deprivation increases $[Cl^-]_i$ at midday (ZT5), the trough of its circadian cycle. The result suggests that this form of sleep loss affects chloride revealing (dys)regulatory influences beyond circadian phase. A reasonable alternative interpretation is that the sleep deprivation protocol we used caused some degree of stress, even if widely used in literature. Stress may in turn elevates $[Cl^-]_i$ through mechanism still unknown. To resolve these possibilities, future experiments should include concurrent endocrine and behavioural stress readouts (Nyuyki et al., 2012; Siddique et al., 2018), so that deprivation-induced effects can be disentangled from putative stress-induced ones.

So far, we investigated relevant questions using LSSmClopHensor, which allows to perform quantitative measures of steady state $[Cl^-]_i$. However, we reasoned that this GECS had limited utility due to the strong pH dependency of the fluorescence. This

requires performing *in vivo* 2P spectroscopy to measure pH, limiting the use of this sensor on steady state conditions only. Also, the sensor pK_a of 6.67 resulted in a low Cl^- affinity at physiological pH (K_d' = 56 mM).

To overcome the pH sensitivity and affinity limitations of earlier sensors, we developed and characterized a new GECS, which we called iClima (for improved chloride imaging). Similarly to its predecessor, iClima's architecture combines a green chloride- and pH-sensitive reporter with a pH- and chloride-insensitive red reference in a ratiometric format. Calibrations defined a high pK_a and a well behaved isosbestic point. Together with a K_d that matches the $[Cl^-]_i$ in adult pyramidal neurons, these properties reduce residual pH contamination within the physiological range and improve sensitivity to small $[Cl^-]_i$ excursions. In practice, this enables more reliable absolute measures of Cl^- and the possibility of resolving smaller Cl^- fluctuations. Importantly, in iClima the red reference fluorophore is mCRISPRed, differently from LSSmClopHensor that owns LSSmKate2. mCRISPRed is characterized by higher brightness and improved photostability compared to LSSmKate2 (photobleaching half-times: mCRISPRed ≈ 93 s, LSSmKate2 ≈ 44 s Piatkevich et al., 2010; Subach et al., 2021). This enhanced stability reduces signal decay during prolonged imaging and, in principle, allows either for longer time-series acquisitions or for denser sampling at higher acquisition frequencies, thus enabling a finer discrimination of chloride dynamics.

Using iClima in the non-neural human U2-OS cell line, a circadian chloride oscillation with a period near 24 hours was detected. The phase relationship to canonical molecular clocks indicates that chloride participates in broader cellular rhythms beyond the nervous system. This is in line with previous observations of ions oscillations in non-neural cells (Feeney et al., 2016; Stangherlin et al., 2021). The ability to resolve such small, long-timescale fluctuations illustrate the sensitivity and stability of iClima in non-neuronal contexts, which strengthens confidence in its performance. *In vivo*, iClima reliably reported large chloride transients during evoked epileptic seizures. We quantified onset and recovery kinetics, that were consistent with a substantial chloride load during pathologic hyperactivity.

Having confirmed that iClima performs reliably *in vivo*, being sensitive to large pathological variations in $[Cl^-]_i$, we next explored its limits of detection. Specifically, we asked whether it could resolve the much smaller $[Cl^-]_i$ changes induced by physiological GABAergic activity, which are likely to be over an order of magnitude lower. Indeed, iClima successfully detected chloride responses to visual stimulation in cortical pyramidal neurons, providing the first *in vivo* optical readout of chloride (inhibitory synaptic) currents under physiological conditions. Light step onsets and offsets produced small but reproducible chloride transients with a decay constant on the order of seconds, measurable in both awake and anesthetized mice. The improved sensitivity of iClima enabled the estimation of inhibitory chloride loads within the physiological range, signals that were undetectable with LSSmClopHensor. Visual stimuli elicited only a modest change in the fluorescence ratio, with a peak increase of ~2.31%. Assuming a cytosolic pH of 7.4, this corresponds to an estimated intracellular chloride load of approximately 370 µM (see methods 5.13). This amplitude is markedly smaller than calcium responses typically observed with GCaMP indicators, where transient increases of intracellular $[Ca^{2+}]$ of only a few hundred nanomolar produce much larger fluorescence changes ($\Delta F/F >$

50%. (Chen et al., 2013). Finally, high-temporal-resolution iClima imaging allowed the detection of single-cell, single-trial chloride responses, further highlighting the sensor's exceptional sensitivity and stability.

Moreover, the onset of chloride transients strongly resembled the time integral of gamma power activity. This concordance with electrophysiology supports the interpretation that chloride entry reflects inhibitory synaptic activity from interneuron classes that participate in gamma rhythms generation (Veit et al., 2017).

Finally, in awake animals, locomotion alone produced transient $[Cl^-]_i$ increases in V1 with second-scale kinetics. Visual stimulation and running combined approximately linearly, which matches the well-known locomotion-related gain modulation of cortical inhibition. The difference here is that the effect is documented directly at the level of Cl^- currents in pyramidal cells.

Some limitations deserve mention. Indeed, while iClima reduces pH sensitivity, extreme pH excursions would still need explicit control. Generation of a pH-insensitive sensor, with pK_a further shifted toward more alkaline values, would address this issue. In addition, although recordings were performed both during the light and dark phases, we did not detect significant differences in the amplitude or kinetics of visually evoked chloride transients between day and night sessions. This was somewhat unexpected, as previous reports have described diurnal modulation of cortical excitability, as well as diurnal difference in the phosphorylation state of NKCC1 and KCC2 transporters (Alfonsa et al., 2023, 2025; Pracucci et al., 2023). It is possible that spontaneous locomotion, which we found to strongly correlate with intracellular chloride increases in awake mice, acted as a confounding variable that masked potential day–night differences. Indeed, locomotion alone induced chloride transients of similar magnitude to those evoked by visual stimulation. Therefore, a more systematic control of behavioural state across circadian phases will be essential to disentangle genuine time-of-day effects from movement-related modulation of inhibitory dynamics.

Another aspect deserving consideration concerns the variability observed during iClima calibration. In particular, both the fluctuations of the radial coordinate (ρ) in the pH calibration and the variable dispersion of Rcl values across calibration and time-lapse imaging suggest that the apparent 1-to-1 stoichiometry between the two fluorescent proteins might not always be perfectly stable. This variability could arise from differences in the maturation kinetics of the two fluorophores: according to the online database FPBase (Lambert, 2019), the mClover3 has a maturation half-time of approximately 43.5 min, whereas the mCRISPRed requires about 354 min to reach half-maximal fluorescence. A slower maturation of the red fluorophore could transiently unbalance the green/red ratio in dividing cells, such as the cells used during calibration. This interpretation is consistent with the greater variability observed in cultured cells compared to *in vivo* experiments. In non-dividing neurons, protein turnover is slow, and synthesis/degradation rates are relatively stable, probably leading to condition closer to a steady-state equilibrium between the two mature fluorophores. In contrast, cultured cells undergo continuous division and de novo protein synthesis, conditions under which asynchronous fluorophore maturation could increase the variability of the Rcl. This variability may represent a limitation for the accurate estimation of absolute $[Cl^-]_i$ values

but does not compromise the reliability of ratio kinetics, which ultimately constitute the most relevant parameter for dynamic measurements.

Regarding the practical application of the sensor, iClima offers a versatile and robust alternative to previous chloride indicators, both chemical and genetically encoded. A primary advantage over chemical sensors lies in its genetically encoded nature, which enables cell-type-specific targeting and supports stable, long-term measurements both *in vitro* and *in vivo*. The sensor can be readily delivered via *in utero* electroporation using plasmid constructs or through viral vector injection, providing a high degree of experimental flexibility. As with all GECS, iClima's chloride sensitivity is inherently coupled to pH. However, the green fluorescent protein has been specifically optimized so that, within the physiological pH range, this dependence is minimized, thereby enhancing measurement reliability in biological conditions. From a technical perspective, the main hardware requirement is the ability to acquire two emission channels, either simultaneously or in rapid succession (e.g., using two-photon microscopy or spinning disk systems), which is a standard feature in most modern imaging facilities.

The practical implementation of iClima depends on the experimental goal. When absolute chloride concentrations are required, iClima follows a calibration strategy conceptually similar to that of LSSmClopHensor. Although pK_a and K_d are intrinsic properties of the sensor, calibration of the imaging system is necessary to account for factors such as fluorophore-specific bleed-through, the R_0 (green/red ratio at zero intracellular chloride), and detector gain differences. The latter can be corrected using a reference fluorophore (e.g., Rhodamine 6G), as described in Chapter 2.1.4.2. While these parameters currently depend on the specific microscope setup, we are developing a standardized methodological framework (to be described in a forthcoming methods article). This approach will allow users to scale reference excitation spectra according to instrument-specific factors, thereby enabling the conversion of raw fluorescence measurements into quantitative estimates of intracellular pH and absolute chloride concentration with minimal additional complexity.

When the aim is to measure relative changes in intracellular chloride, iClima represents a substantial improvement over previous sensors. The sensor dynamics can be analysed using approaches analogous to those commonly employed in calcium imaging experiments. However, as a turn-off sensor, iClima inherently exhibits a lower signal-to-noise ratio compared to turn-on indicators. This limitation is further intensified by the fact that physiological chloride fluctuations, such as those elicited by visual stimulation or locomotion, are relatively small in amplitude, resulting in noisier signals compared to calcium transients. In addition, it should be noted that both the green and red channels are occupied by the sensor, which may represent a practical limitation for experiments requiring additional fluorescent reporters. Despite these limits, the ratiometric nature of iClima provides an advantage, since as the green/red ratio intrinsically corrects for fluctuations in excitation power. Furthermore, iClima supports high-frequency imaging over extended periods with minimal signal degradation, demonstrating high photostability. This contrasts with earlier sensors such as LSSmClopHensor, which exhibited significant photobleaching of the red fluorophore. In this context, implementation is straightforward and requires only an initial estimation of bleed-through between the green and red

channels for the specific imaging system, which can then be subtracted from the recorded signals.

iClima opens several concrete perspectives. First, targeted sparse expression will let us resolve chloride dynamics at subcellular scale, including distinguishing Cl^- transients in dendrites and spines compared with somata. This should reveal whether chloride microdomains emerge during specific synaptic inputs and how they dissipate across space and time. Building on this, sparse labelling combined with high-speed imaging will enable compartment-specific measurements during controlled input: by optogenetically activating distinct interneuron classes such as PV, SOM, and VIP, we can map the chloride load they impose on pyramidal neurons and test for characteristic spatial and temporal fingerprints.

Alterations in the excitation/inhibition balance are a hallmark of several neurological and psychiatric disorders, often arising from impaired inhibitory neurotransmission due to disrupted chloride homeostasis. Dysregulation of intracellular Cl^- levels compromises GABAergic signalling, leading to aberrant network excitability and defective information processing. Such mechanisms have been implicated in disorders including epilepsy, autism spectrum disorders, and schizophrenia, where altered efficacy of chloride cotransporters systems, particularly via KCC2, results in depolarizing GABA responses and a loss of inhibitory control (Ben-Ari, 2017; Hyde et al., 2011; Kaila et al., 2014). By applying iClima to disease models, it will be possible to precisely monitor how $[Cl^-]_i$ evolves during these pathological states, identify how disrupted Cl^- homeostasis contributes to altered signalling cascades, even at the subcellular level. Eventually, this will be useful to evaluate the efficacy of therapeutic interventions aimed at restoring chloride-dependent signalling.

A broader implication concerns chloride as a messenger. Recent literature is indeed starting to consider chloride not only a passive carrier of inhibition but a dynamic signal that interacts with intracellular cascades, as in the case of the interaction with WNK (Lüscher et al., 2020). The discovery that WNK kinases are directly regulated by intracellular chloride concentration (Piala et al., 2014) has redefined the classical view of Cl^- as a mere biophysical determinant of inhibition, highlighting its role as a genuine second messenger capable of modulating kinase activity and ion transporter function. This pathway establishes a bidirectional communication between ionic homeostasis and cell signalling: changes in $[Cl^-]_i$ not only influence neuronal excitability but also trigger phosphorylation cascades that adjust transporter activity (Boyd-Shiwarski et al., 2022; Heubl et al., 2017; Rinehart et al., 2009). In this framework, chloride becomes an active participant in cellular adaptation processes, linking inhibitory transmission, osmotic regulation, and cell-volume control to broader physiological states such as sleep–wake cycles and circadian modulation of excitability (Alfonsa et al., 2023; Pracucci et al., 2023). Thus, tools like iClima represent a crucial technological step, as they allow quantification of $[Cl^-]_i$ fluctuations *in vivo*, enabling us to investigate chloride's role across physiological and pathological contexts. The study of chloride physiology is only beginning. As more advanced optical tools emerge, they will uncover how this ion orchestrates cellular signalling and contributes to the brain's intricate electrical and biochemical language.

Phase 1) Use of LSSmClopHensor to investigate steady-state Cl^- homeostasis

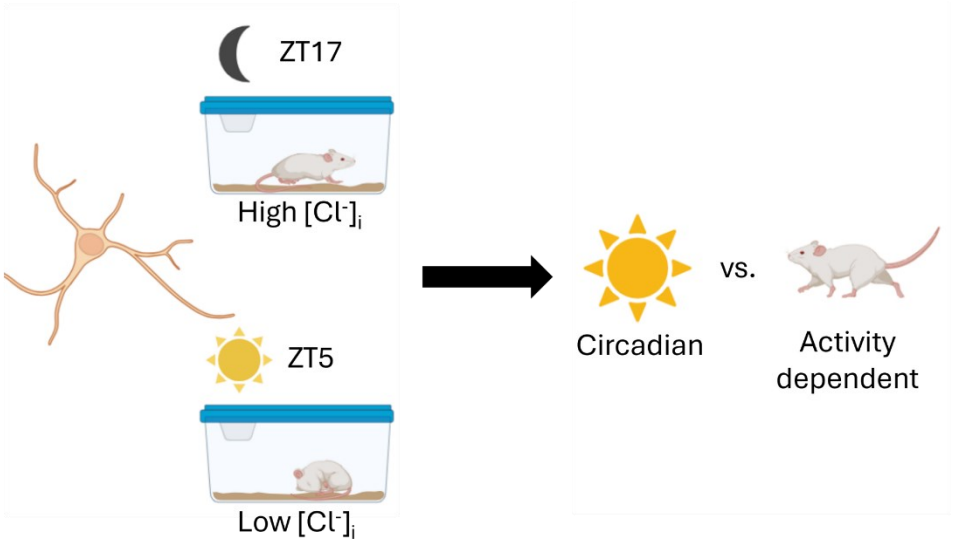

Phase 2) Characterization of the improved GECS iClima

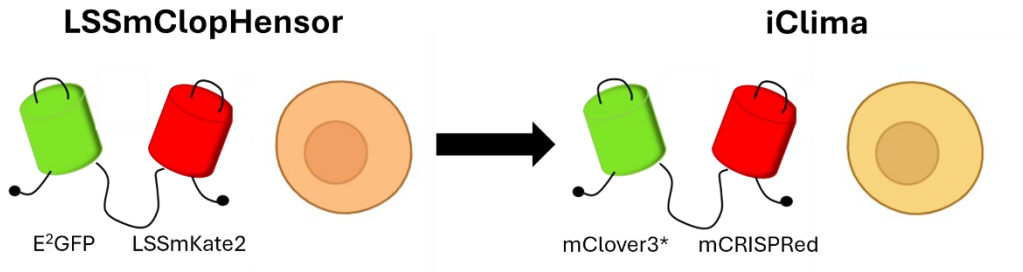

High pH-dependency

Low affinity (K_d'= 56 mM)

Limited to steady-state imaging

Reduced pH interference

Improved sensitivity (K_d'= 7.3 mM)

High photostability

Capable of detecting physiological Cl^- fluctuations

Phase 3) Use of iClima *in vitro* and *in vivo*

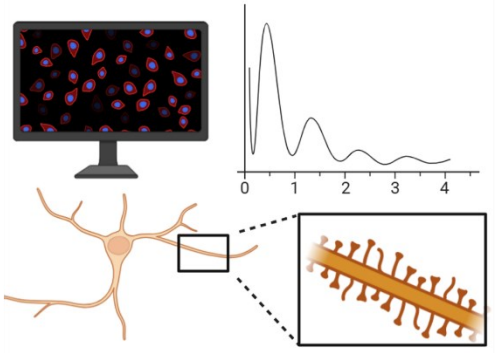

2-photon imaging *in vivo*

Measure absolute $[Cl^-]_i$

Long-lasting time series recordings

Detect even small physiological Cl^- fluctuations

Subcellular imaging (dendrites/spines)

Figure 24: Schematic overview of the conceptual and methodological framework of this work. Phase 1) Intracellular chloride concentration in cortical pyramidal neurons follows a diurnal cycle, being low during the light/resting phase (ZT5) and high during the dark/active phase (ZT17). This observation raised the question of whether $[Cl^-]_i$ oscillations are controlled by intrinsic circadian mechanisms or by neuronal activity and behavioural state. To address this, we employed LSSmClopHensor for quantitative steady-state measurements. **Phase 2)** We developed and characterized iClima, a new genetically encoded chloride sensor (GECS). The previously available LSSmClopHensor was limited by pH sensitivity and low chloride affinity. iClima combines a Cl^--sensitive green fluorophore (mutated mClover3) with a bright, pH-insensitive red reference (mCRISPRed). This design enhances sensitivity, reduces pH interference, and increases photostability. **Phase 3)** iClima was used *in vitro* and *in vivo* to detect Cl^- shifts in both physiological and pathological states. iClima enables long-term in vivo 2-photon imaging and detection of subtle physiological Cl^- fluctuations at cellular and subcellular resolution. Illustration created with BioRender.com

5. Materials and Methods

5.1 Solutions

- Urethane 20 mg/100ml was obtained dissolving urethane salt (Sigma) in saline water (0.9% NaCl) at room temperature.
- Tribromoethanol (Avertin) anesthesia was used in a concentration of 0.02 mL per 1 gr of mouse
- Artificial cerebrospinal fluid (ACSF) 1x stock was prepared with NaCl 120 mM, KCl 3.2 mM, K_2HPO_4 1 mM, HEPES 10 mM, $NaHCO_3$ 26 mM in a final volume of 1L of deionized water. The 7.4 pH was adjusted at 7.4 and the stock was stored at 4°. Fresh preparations were enriched with $CaCl_2$ 2 mM and $MgCl_2$ 1 mM.
- Bumetanide 55 μM solution was produced by adding an 8-μL aliquot of bumetanide stock solution (50 mg/mL in DMSO) in 10 mL of saline.

5.2 Behavioural tracking and analysis

Mouse behaviour was recorded and analyzed using a custom-made MATLAB code developed in our laboratory, in combination with a video-recording system. Experiments were performed on one animal at a time, within a closed arena (57 x 32 cm) equipped with food and water ad libitum and maintained under a standard 12h light/dark cycle (lights off: 7:00 PM–7:00 AM). The arena was continuously monitored using an infrared camera, and data acquisition was synchronized via an Arduino-based system.

To reduce variability due to novelty-induced exploration, automated recordings were performed for at least three consecutive days, with the first 24 h excluded from analysis. The tracking algorithm extracted the silhouette of the animal from the background reference image and computed the center of mass of the binary object (“blob”). This approach enabled reconstruction of locomotor trajectories and classification of behavioural states into locomotion, local activity (e.g., grooming), or resting. Periods of immobility longer than 40 s were classified as sleep (Fisher et al., 2012; Pack et al., 2007). From these data, actograms were generated to visualize changes in locomotor speed, spatial trajectories, and positional preferences within the arena. These features provided a reliable readout of behavioural dynamics across light/dark cycles. For the ZT29D condition, the dark phase was extended beyond the regular 12 hours, and recordings were continued to monitor changes in locomotor state. The analysis pipeline was implemented in a custom MATLAB code developed in our laboratory.

5.3 Viral injections and chronic implants

Expression of the LSSmClopHensor and iClima was achieved through viral transfection in the indicated experiments. Both sensors were expressed by co-injection of adeno-associated viral (AAV) vectors. The viral constructs used for these experiments were AAV9.EF1α.DIO(LSSmClopHensor) or AAV9.EF1α.DIO(iClima), and AAV9.CamKII.Cre for Cre-dependent expression. Both sensor constructs were designed as double-floxed inverted open reading frame (DIO/FLEX) vectors under the EF1α promoter. For co-expression, viral mixes were prepared at the following final titers: 8.7×10^{11} vg/ml for the sensor virus and 2.1×10^{11} vg/ml for the Cre virus.

Mice were anesthetized with 2,2,2-tribromoethanol (Avertin) administered intraperitoneally at 0.02 ml/g body weight. Depending on the experimental protocol, two types of surgeries were performed: acute injections or chronic window preparations. For acute experiments, two small craniotomies were drilled above the primary visual cortex (V1), using stereotaxic coordinates relative to lambda: antero-posterior (AP) = 0 mm and medio-lateral (ML) = 2.5 mm and 3.5 mm. A Hamilton NanoFil syringe equipped with a 36G needle (World Precision Instruments) was positioned at the injection sites, and 500 nl of the viral mix (sensor + Cre) was injected at a depth of 300 µm below the cortical surface (two depths of 750 and 450 µm were used for the PFC) at a rate of 100 nl/min. After each injection, the needle was left in place for 1 min to minimize reflux along the injection tract. At the end of the injections, the skin was sutured using sterile surgical thread, and a topical analgesic gel was applied to the incision site. Mice were allowed to recover from anesthesia on a heating pad before returning to their home cage.

For chronic experiments, a 3 mm diameter craniotomy was performed over V1. Two injections of the viral mix were delivered as described above were perfomed at the same stereotaxic coordinates used for acute injections (500 nl each at 300 µm depth). Following injections, a chronic cranial window was implanted to allow long-term two-photon imaging. The window consisted of two circular glass coverslips (inner diameter 3 mm, outer diameter 5 mm) permanently bonded together using optical adhesive. The smaller coverslip fit precisely within the craniotomy, while the larger one was secured to the skull surface with cyanoacrylate glue. A custom lightweight metal head bar (<1 g) was then affixed to the skull caudal to the craniotomy using Metabond dental cement (Parkell) followed by a layer of Paladur (Kulzer). Once the Metabond had set, the Paladur was applied to reinforce the fixation and to create a circular cement well around the cranial window, allowing the application of water during imaging sessions with the immersion objective. The cement ring was finally painted black to absorb ambient light and reduce stray photon contamination during imaging.

After surgery, mice were allowed to recover on a heating pad until fully awake and then returned to their home cage. Paracetamol was administered in the drinking water at a dose of 200 mg/kg/day for 2 consecutive days to provide postoperative analgesia and support recovery.

5.4 *In vivo* chloride imaging with LSSmClopHensor

Intracellular chloride concentration was measured using the genetically encoded ratiometric biosensor LSSmClopHensor, selectively expressed in cortical pyramidal neurons. Expression of LSSmClopHensor was achieved by viral transfection using a mixture of two viral vectors: AAV9-EF1a-DIO(LSSmClopHensor) and AAV9-CaMKII-Cre with a ratio 1:10. Adult C57Bl6j mice (4-6 months) were anaesthetized with 2,2,2-tribromoethanol (Avertin) (i.p. 0.02 ml/g body weight), the head of the mouse was gently fixed in a stereotactic frame and the scalp was open. See the section 5.3 for details about the transfection. V1 injections the injections sites were AP= 0mm and ML = 2.5 and 3.5 mm from Lamda. For PFC injections, ML= 0.5 mm and AP= 2 and 3.5 mm anterior to Bregma.

When ready, mice were anesthetized with 2,2,2-tribromoethanol (Avertin) (i.p. 20 µl/g weight) and prepared for acute two-photon imaging. A 4 mm craniotomy was performed over V1 or PFC and covered with a 5 mm-coverslip. Imaging was performed immediately after surgery. Mice were positioned underneath a 2-photon microscope. Images were acquired at 5 different excitation wavelengths (800 / 830 / 860 / 910 / 960 nm - some of the 800nm data sets were barely fractionally above noise levels and so were not used for analyses) and collected through green and red emission filters (527/70 nm and 607/70 nm respectively, BrightLine). The imaging was performed at depths ranging from 90 to 300 µm, corresponding to cortical layers 2/3. Post hoc analysis of the images was performed using a graphical user interface (GUI), implemented in MATLAB, that automated finding cell somata, to collect red/green fluorescence ratios at the different wavelengths, and compute intracellular pH and [Cl^-] values for each cell, based upon earlier calibration experiments performed using ionophore-permeabilized GL261 cell and neuronal cultures (Sulis Sato et al., 2017). The imaging was performed with a Bruker Ultima microscope, a Coherent Ultra II laser and an Olympus 20X, NA 1.05 objective (water immersion). For the ZT29D experiments, imaging sessions were performed after 16 hours of extended darkness, corresponding to ZT28–29.

5.5 Sleep Deprivation

Mice expressing LSSmClopHensor in the prefrontal cortex were subjected to a 24-hour sleep deprivation paradigm (see section 5.4 for sensor expression). Two weeks after viral injection, animals were placed individually on small circular platforms (“flowerpots”) surrounded by water, a widely used method for selective REM sleep deprivation in rodents (Mendelson et al., 1974). The platform had a diameter of 3.5 cm, allowing the mouse to maintain balance during wakefulness and non-REM sleep, but causing it to fall into the surrounding water upon entering REM sleep, when muscle tone is lost. The water level was adjusted so that the animal’s body remained above the surface when standing on the platform, but contact with the water was immediate if it lost postural control. Water temperature was maintained at 27 °C throughout the 24-hour deprivation period to ensure thermal comfort and prevent hypothermia. The flowerpot setup was covered with a metal wire mesh positioned above the tank, allowing the animals to freely access food pellets and a water bottle placed on top of the grid. The sleep deprivation started at midday (ZT5)

and continued for 24 hours. At the end of the deprivation period, mice were anesthetized and prepared for two-photon imaging as described in the section 5.4, and analized accordingly.

5.6 Seizure susceptibility experiments

Seizure susceptibility electrophysiological experiments were performed on acutely prepared C57BL/6J mice, under urethane anaesthesia (i.p. 1.6 g/kg). The mouse was placed in a stereotaxic head-holder and a small craniotomy was performed to reveal the cortex. Recording was performed either using AgCl electrodes with a 2 MOhm glass pipet or a multi-electrode array. For AgCl recordings, LFP signals were amplified 500 times (EXT−02F amplifiers; NPI electronic), band pass filtered (0.1−1000 Hz), cleared from 50 Hz electrical noise (Hum Bug Noise Eliminator; Quest Scientific), and finally sampled at 10 kHz (16-bit AD board USB6251 from National Instrument). For MEA recordings (MEA, Neuronexus – A1x16-3mm-25-177), the signal was digitised at 30 kHz (NPI EXT-02F amplifier), and acquired with the Neuronexus SmartBox Pro. In both cases, electrodes were introduced into the cortex to a depth of 0.3 mm, and approximately positioned within the primary somatosensory cortex. The cortex was kept moist with warmed saline throughout recording sessions.

Epileptic activity was induced acutely by a single bolus injection of 500 nl of 15 mM 4-aminopyridine in saline (total amount delivered 7.5 nmol), injected at 500 nl/min via a NanoFil needle (36G, World Precision Instruments; 30 s injection), roughly 1 mm caudal to the recording site (approximately into the anterior end of primary visual cortex). In all the animals, saline was applied directly to the surface of the brain after the craniotomy was made, to keep it moist. In a subset of experiments, this saline solution was supplemented with either 55 μM bumetanide (in 0.08% DMSO and saline) or VU0463271 (10 μM in saline and 0.1% DMSO, as described for the preceding experiments) for approximately 1 hour before 4-AP injections. To test for effects of this trace amount of DMSO, in two experiments (arrowheads in **Figure 13**d), saline was applied with just 0.08% DMSO.

Extracellular field recordings were analysed to detect pathological discharges using a custom-written code in MATLAB. In brief, this used a frequency-domain analysis to detect time-frequency pairs with “abnormal” power (**Figure 25**). The spectrogram (bin width 10 s, with 1 s time shift) of the baseline (the period preceding 4AP injection) was computed and we obtained mean and standard deviation of the spectral power for frequencies between 8-100 Hz. The spectrogram of the entire recording was normalized to the baseline mean and standard deviation for each frequency band individually. To avoid contamination with mains noise, we omitted frequencies between 49-51 Hz. This process generated a Z-score spectrogram (Z = (x-mean)/s.d.), in which each element of the Z-score matrix represented the excess power at a particular frequency, for each time bin. Using a threshold of 4 standard deviations above the baseline mean, we identified all time bins for which any frequency exceeded this threshold. The power integrated in each time bin was summed cumulatively, to estimate the pathological activity within the brain. Continuous epochs of suprathreshold bins lasting more than 15 s were designated to be

single “events”. In fact, most seizures lasted for many tens of seconds, before transitioning into a period of post-ictal suppression.

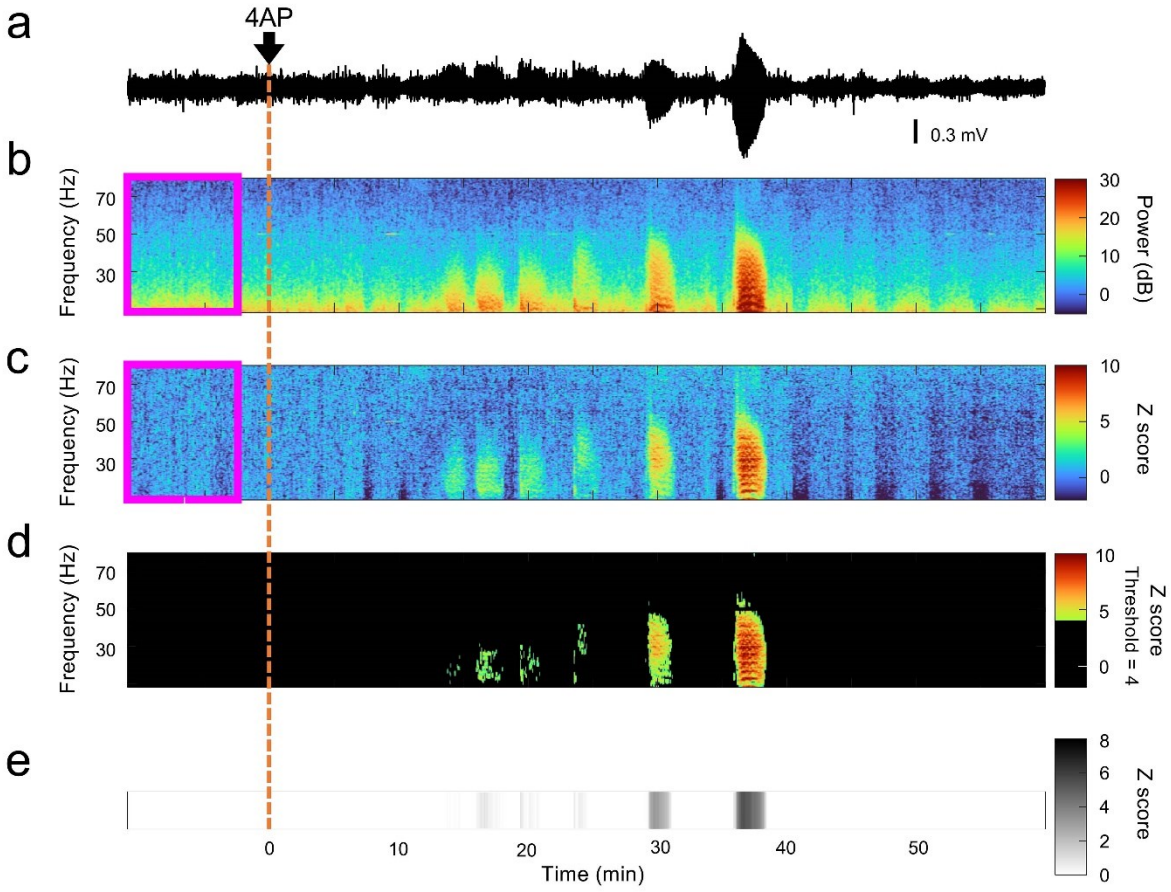

Figure 25: Computation of the z-scoring of epileptiform activity. a) An example trace of the LFP recording, during a midnight 4-AP experiment. 4AP was microinjected over a period of 5 min, starting at time 0. **b)** Spectrogram of the same trace (computed using the MATLAB function mtspecgramc.m; time windows of 10 s with steps of 1 s, 5 tapers and time-bandwidth product=3). Frequencies between 8 Hz and 100 Hz were used. Note that power attenuates at high frequencies. The magenta frame highlights a baseline period before 4AP injection. **c)** Z-transform of the spectrogram in b computed as follows: for each frequency f, we computed the mean (μ_f) and the standard deviation (σ_f) of the power during the baseline. Then, for every element of the spectrogram x_{ft}, the z transform was obtained with $(x_{ft} – \mu_f) / \sigma_f$. Note that this normalization overcomes the attenuation of the power at high frequencies. **d)** A binary mask was applied to the z-transform of the spectrogram to keep only values higher than 4 (4 σ higher than the baseline power). **e)** The z-score time course was computed, summing the z-transform of the spectrogram across all frequencies (columns).

5.7 iClima calibrations

Mouse embryonic fibroblast (MEF) cells were cultured in Dulbecco’s Modified Eagle Medium (DMEM, high glucose; Gibco) supplemented with 10% fetal bovine serum, 100 U/ml penicillin, and 100 µg/ml streptomycin (Gibco). The cells were maintained at 37°C in a humidified incubator with 5% CO_2 until they were used for transfection. Transfection was performed using the Neon™ Transfection System 100 µL Kit (Thermo Fisher Scientific). Briefly, cells were trypsinized, centrifuged, and washed twice with phosphate-buffered saline (PBS). The resulting pellet was resuspended in the manufacturer’s resuspension buffer and mixed with 10–12 µg of plasmid DNA encoding for either mClover3 (modified

as in iClima), mCRISPRed, or iClima under the control of the CAG promoter. Electroporation was then carried out using 2 pulses of 20 ms at 1200 V. Immediately after electroporation, the cells were transferred to 35 mm dishes containing fresh culture medium and maintained for 48 hours before imaging.

For both pH and chloride calibrations, a specific calibration medium was used. This solution contained 20 mM HEPES, 0.6 mM $MgSO_4$, 38 mM Na-gluconate, and 100 mM K-gluconate. To obtain the desired chloride concentrations, this medium was mixed with a solution in which NaCl and KCl replaced Na-gluconate and K-gluconate, thus allowing to reach final chloride concentrations ranging from 0 to 138 mM. To equilibrate intra- and extracellular ions and to allow complete exchange of protons and chloride ions across the plasma membrane, the calibration medium was supplemented with a cocktail of ionophores composed of nigericin (5 µM), carbonyl cyanide p-chlorophenylhydrazone (CCCP, 5 µM), valinomycin (5 µM), and tributyltin chloride (TBTC, 10 µM). The culture medium was removed from the plates and replaced with the ionophore-containing calibration solution, and cells were then exposed to six sequential washes of three minutes each to ensure complete equilibration. For pH calibrations, the chloride concentration was kept at 0 mM and the pH of the solution was varied, while for chloride calibrations the pH was fixed at 7.2 and only the chloride concentration was changed.

Two-photon imaging experiments were performed at eight different excitation wavelengths (800, 830, 860, 875, 890, 910, 940, and 960 nm). Emission light was collected through green and red band-pass filters (527/70 nm and 607/70 nm, respectively; BrightLine). The temperature during imaging was maintained at 32°C. For each experimental condition, the mean fluorescence intensity in the green and red channels was measured, and the ratio between them (G/R) was calculated. The G/R values at different pH were fitted as explained in the introduction 2.1.4.2.

One-photon characterization of iClima was performed using a Leica Stellaris confocal microscope equipped with a white-light laser. Excitation was carried out at 440, 445, and 450 nm, and then every 10 nm up to 490 nm. Emission spectra were recorded between 465 and 695 nm with 21 steps, a step size of 10 nm, and a bandwidth of 30 nm. Since this system does not use fixed emission filters as in two-photon microscopy, the pH calibration was performed by integrating the emission spectra over two selected wavelength ranges corresponding to the green (520–555 nm) and red (590–625 nm) emission channels. The fluorescence intensity in these ranges was corrected for bleed-through, calculated independently for each spectral window. After correction, the G/R ratio was computed for each pH condition, and the resulting values were fitted to derive the apparent pK_a, following the same fitting procedure used for the two-photon data.

For Cl^- calibrations, washes at several extracellular [Cl^-] were performed, ROIs extracted, dark- and BT corrected, and eventually emission spectra extracted (1-photon). Fitting was then performed as explained in the results to find the K_d.

5.8 Bioluminescence recording with ALLIGATOR

U2OS cells stably expressing *PER2:Luc* or p*BMAL1:Luc* reporters were cultured under standard conditions (using DMEM (Dulbecco's Modified Eagle Medium) +10% Serum (HyClone™ FetalClone™ II Serum) + 1% Penicillin/Streptomycin) and prepared for circadian bioluminescence recordings using a Lumicycle (Obscura Alligator Luminescence System, Cairin Research). Cells were split and seeded at a density of approximately 1×10^4 cells/mL in a 96-well dish using pre-warmed growth medium. A total of 12 wells for each condition were plated and were entrained for five days as described in results. On day 6, cells were replenished with reduced (1%) serum medium supplemented with 0.3 mM Luciferin. During this procedure cells were kept on a pre-warmed heating platform (37 °C). Cells were then placed at constant 37 °C to allow stabilization of rhythms under free-running conditions for 24 hours.

On the experimental day, dishes were sealed with gas permeable adhesive seals. Bioluminescence was continuously recorded every hour for 3 days, setting the exposure time of the Lumicycle at 30 minutes. Images were analysed with ImageJ. Single ROI were drawn around each of the 12 well and the average intensity fit to be detrended.

5.9 Microwave Plasma – Atomic Emission Spectroscopy (MP-AES)

Elemental analysis was performed using an Agilent 4210 MP-AES (Microwave Plasma – Atomic Emission Spectrometer; Agilent Technologies, USA). MP-AES enables simultaneous multi-element detection based on excitation of aerosolized sample droplets in a nitrogen plasma (≈6000 °C), followed by wavelength-resolved emission measurements. Unlike ICP-MS, MP-AES does not rely on ionization but instead detects element-specific emission photons. The system is suitable for the detection of most elements with the exception of sulfur, chloride, and fluoride, which cannot be reliably quantified. *pBMAL1:Luc* U2OS cells were seeded in 12-well plates and grown to confluence. For each condition, four replicates were prepared to account for variability and potential outliers. Cells were entrained for five days as described in results. On day 6, a final medium change was performed at 10:00 a.m. using recording medium (DMEM supplemented with 1% serum, 1% Penicillin/Streptomycin). During this procedure, plates were maintained on a pre-warmed heating platform (37 °C) to avoid temperature shock. Cells were then transferred to constant 37 °C conditions for 24 h under free-running conditions prior to harvesting.

For MP-AES sample preparation, plates were transferred onto ice and washed once with 1 mL ice-cold salt-free iso-osmotic buffer A (300 mM sucrose, 10 mM Tris base, 1 mM EDTA; pH 7.4 adjusted with phosphoric acid), followed by two washes with buffer B (identical composition, pH 7.4 adjusted with acetic acid). Osmolarity of the buffers was carefully matched to that of the culture medium (~330–340 mOsm) using concentrated sucrose and confirmed with an osmometer. All solutions were prepared with HPLC-grade water and analytical-grade reagents. After removal of residual buffer, cells were lysed by adding 200 µL of 65% ultrapure nitric acid. Lysis proceeded for 1 hour at room temperature

in a chemical fume hood. Lysates were collected, span at 10°C, and 100uL of the solution was added to 1.2 mL of HPLC water in 15 mL Falcon tubes and stored at –80 °C until analysis.

For the MP-AES measurements, the volume per run was 1.3 mL. To minimize background noise, all glassware were rinsed three times with HPLC-grade water prior to use. Particular care was taken during washes and transfers to avoid disrupting the cell monolayer or introducing trace contaminants. For each run, calibration standards were prepared in 5% ultrapure nitric acid to match the matrix of the samples. A multi-element calibration solution (Agilent, 5190-7001) containing 5 ppm of trace metals and 50 ppm K was used as reference. A series of calibration curves was generated by running at least three standard dilutions plus a blank (5% HNO_3) before sample analysis. Sample concentrations were then quantified against the calibration curves.

5.10 Time-lapse imaging of iClima-expressing cells

pBmal1:Luc U2OS cells stably transfected with the iClima sensor (iClima under EF1α promoter) were used for time-course imaging experiments. Cells were split as usual and seeded at a density of 3 × 10^4 cells/mL in 8-well Ibidi chambered dishes (Ibidi, cat. no. 80826) using pre-warmed growth medium. Four wells were prepared and incubated at 37 °C until reaching full confluency (5 days). At 10:00 am, a pre-warmed medium change was performed using DMEM supplemented with 10% HyClone™ FetalClone™ II Serum and 1% Penicillin/Streptomycin, providing a synchronizing pulse. Cells were then transferred to a temperature-cycling incubator (37 °C at 10 am, 32 °C at 10 pm) for 5 days to entrain circadian rhythms. On day 6, phenol red-free DMEM supplemented with 1% serum and Penicillin/Streptomycin was pre-warmed and used for the final medium change at 10:00 am. During this procedure, cells were maintained on a 37 °C pre-heated platform. Cultures were subsequently placed at constant 37 °C under free-running conditions for 24 h prior to imaging.

Imaging was performed on a Leica SP8 confocal microscope equipped with an environmental chamber set to 37 °C and 5% CO_2. The following acquisition settings were used: excitation at 442 nm and 488 nm (laser power 15% for both), the green emission filter was 500–545 nm while the red emission filter was 570–700 nm. 15 square fields of side 581.25 µm were acquired per well. Acquisitions were performed every 3 hours with the help of autofocus. After 2 days of recording, one well was removed from the analysis due to due to poor cell health. Regions of interest (ROIs) were drawn with the help of a custom made MATALB app. The average Greed and Red value of each ROI was extracted and ratio calculated. ROIs were re-drawn for each timepoint to manage putative dead cells or cell movements. Data acquired with 488 nm excitation were used for the fit due to the low quality of the 442 nm-excited data.

5.11 Circadian fit for MP-AES and *in vitro* imaging of iClima

MP-AES data and iClima R/G results were fitted using a nonlinear least-squares procedure. The model function combined a linear baseline with a damped oscillatory term, and was defined as:

$$Y(X) = B + mX + A\,e^{-kX}cos\left(\frac{2\pi\,(X-\varphi)}{T}\right)$$

where B is the baseline, m the slope of the linear trend, A the oscillation amplitude, k the exponential damping coefficient, φ the phase shift, and T the period of the oscillation. The period parameter was constrained within a predefined range [20, 24] to reflect physiological plausibility.

Weighted residuals were used to account for the measurement errors of the data points:

$$r(X) = \frac{Y(X)_{data} - Y(X)_{model}}{\sigma_Y}$$

where σ_Y is the standard deviation associated with each observation.

To evaluate whether the oscillatory model provided a significantly better fit than a constant baseline model, we compared it against a null model defined as:

$$Y\,(X) = constant$$

Where constant being the mean of the data. The goodness-of-fit improvement was assessed using an F-test:

$$F = \frac{(SSE_0 - SSE_2)/(k_2 - k_0)}{SSE_2/(N-k_2)}$$

where SSE_0 and SSE_2 are the residual sums of squares of the null and full models, respectively, k_0 and k_2 their number of free parameters, and N the number of data points. The corresponding p-value was used to test whether the full model explained the observed variability significantly better than the constant model.

5.12 *In vivo* chloride imaging with iClima with simultaneous LFP recording

Intracellular chloride concentration was measured using the genetically encoded ratiometric biosensor iClima, selectively expressed in cortical pyramidal neurons. The specific expression was achieved by *in utero* electroporation at embryonic day 15.5 (E15.5) with a custom-made triple electrode to transfect neuronal progenitors of layer 2/3 pyramidal neurons of the visual cortex (Dal Maschio et al., 2012). Briefly, *C57BL/6J* pregnant females were obtained arranging timed matings. E15.5 pregnant mice were anaesthetized with isoflurane (5% for the induction, 1% for maintenance) and placed face up on a heating pad covered with a sterile sheet. Intramuscular injections of a pain killer

(Tramadol 50 mg/ml, dose: 50 µg/g) and an antibiotic (Baytril 50 mg/ml, dose: 75 µl/g) were performed. The hair on the abdominal region was removed using a hair removal cream (Veet) and the skin was cleaned with an Iodine solution (Betadine) and then with ethanol 70% 3 times. The uterus was exposed with laparotomy and a solution of plasmid encoding iClima under the CAG promoter (5 µg/µl) and a green dye (Fast Green, 0.3 mg/ml in water) was injected in the right lateral hemisphere of the embryos through a 30g needle connected to a pico-pump. A triple electrode was used to transfect the neuronal progenitors in the occipital region. Embryos were kept wet delivering heated sterile saline solution. After the transfection, the abdomen was stitched, a healing ointment (Connettivina) was applied on the wound, and the mouse was left in a warm cage to recover. Additional antibiotic was administered orally for the next 3 days.

Mice obtained through this procedure were used for imaging experiments starting from postnatal day 29. They were anaesthetized with urethane anaesthesia (i.p. 8µl/g of 20% urethane salt (Sigma) in NaCl 0.9%). The anaesthesia level was assessed using a tail pinch and, if needed, additional doses (10% of initial dose) were administered to maintain a stable level of anaesthesia. A local anaesthetic (Lidocain Hydrochloride 1% gel; Molteni Farmaceutici) was applied to the skin before cutting it. The head of the mouse was fixed in a stereotactic frame; the skull was cleaned from membranes and dried. A 4 mm craniotomy was performed over V1 and partially covered with a 5mm-glass coverslip. A chamber was created around the craniotomy applying a thin layer of dental cement (Vertex Dental). The cortex was maintained constantly wet with artificial cerebrospinal fluid (ACSF). Once under 2-photon microscope, the fluorescence was checked to understand which part of the brain to penetrate with the LFP electrode. LFP recording was performed using an Ag/AgCl electrode in a glass microcapillary. A Sutter Instruments puller was used to pull the borosilicate microcapillary (outer diameter of 1 mm, inner diameter of 0.58 mm, length of 10cm, BF-100-58-10; Sutter Instruments) up to a tip diameter of about 1.5 µm. The capillary was filled with ACSF and inserted into an electrode holder, which was connected to the electrode filament. The holder was inserted into a headstage (NPI Electronics) connected to a reference electrode bathing into the ACSF-filled recording chamber obtained in correspondence of the craniotomy of the mouse. Glass micropipette was placed at a depth of 250 − 300 µm to record from cortical layers 2/3 (using a motorised micromanipulator at an angle of 45°; Sutter Instrument MP-C -200) in the same area of the 2-photon imaging, reaching the brain from the glass-opening of the craniotomy. LFP signals were amplified 1000 times (EXT − 02F amplifiers; NPI electronic), band pass filtered (0.1−1000 Hz), cleared from 50 Hz electrical noise (Hum Bug Noise Eliminator; Quest Scientific), and finally sampled at 10 kHz with 16-bit precision (AD board USB6251; National Instruments). 2-photon images for absolute chloride measurements were acquired at 5 different excitation wavelengths (830 / 860 / 880 / 930 / 960 nm) and collected through green and red emission filters (527/70 nm and 607/70 BrightLine®). We used a Bruker Ultima microscope with a Chameleon Ultra II laser (Coherent) and an Olympus 20X objective (NA 1.05, water immersion). After absolute Cl^- measures, at least 3 minutes of baseline local field potential were recorded. Next, we dripped 4-aminopyridine (15 µM in ACSF) directly onto the craniotomy, where a partial cover glass allowed it to penetrate and diffuse to the brain parenchyma.

Following that, both imaging at 830 nm (1 frame every 10 s) and LFP recording were acquired on a time series. In case the animal did not show any seizure within 50 min form 4-AP, VU0463271 10 µM was added to the bath. Absolut chloride concentration was obtained following all the steps presented in the introduction, using a GUI implemented in MATLAB, that automated finding cell somata, to collect red/green fluorescence ratios at the different wavelengths, and compute intracellular pH and [Cl^-] values for each cell. Local field potential recordings were analyzed using *ZebraExplore*, a MATLAB-based graphical user interface developed in the laboratory, which provides tools for visualization and analysis of electrophysiological recordings. Local field potential recordings and the input voltage to the galvanometric mirrors were acquired simultaneously using the same acquisition board. A custom MATLAB script extracted the timing of each imaging frame from this signal, enabling precise synchronization between two-photon imaging and LFP recordings. Seizure were detected as described in methods chapter number 5.6. For each identified time window, the script identifies the onset and offset points and extracts epochs from the fluorescence time series centered on either the onset or offset of epileptic events. ROIs were drawn semi-automatically from a custom made MATLAB script. For each ROI, the average red and green fluorescence intensities are calculated by averaging the pixel values within the ROI. Each ROI-event trace was extracted and all were then fitted with a logistic sigmoid function for the onset and a decreasing exponential for the offset.

5.13 Dynamical Cl^- imaging *in vivo*

Experiments were performed on adult *C57BL/6J* mice of both sexes, expressing the chloride sensor iClima or LSSmClopHensor in V1 (see methods 5.3 for details of expression). Mice were housed under a 12 h light/dark cycle with food and water ad libitum. After viral injection and cranial window implantation over V1, mice were allowed to recover for 4 days before behavioural handling. During the following 3 days, mice were handled daily and the wheel from the imaging setup was placed in their home cage to facilitate familiarization. Mice were then habituated to head-fixation under the two-photon microscope across 5 consecutive days. The duration of head-fixation was progressively increased from 10 min on the first day up to 1 h on the fifth day. During habituation sessions, animals were head-fixed while allowed to walk or run voluntarily on a freely rotating wheel. At the end of each habituation session, mice received a small dose of condensed milk as reward.

Imaging experiments were conducted in multiple sessions at two time points: around midday and midnight. Moreover, imaging was conducted in Awake, head-fixed animals allowed to walk on the wheel, and on Anesthetized animals under 1-1.5% isoflurane in O_2 1.5 l/min. During each experimental session, several types of visual stimuli were presented as described in method session *5.14*. Each visual stimulus was presented in at least 5 trials per session. Before the first and after the last trial, a “dark” acquisition (no laser) was recorded to quantify (and later subtract) the contaminating light coming from the visual stimulation screen. Two-photon imaging was performed using a Bruker Ultima microscope equipped with a Chameleon Ultra II Ti:Sapphire laser (Coherent) tuned to 830 nm (910nm in the case of LSSmClopHensor), and an Olympus 20× water-immersion objective (NA 1.05). Emission was collected through green (527/70 nm) and red (607/70

nm BrightLine®) filters. Images were acquired at 2× zoom (squared fields with sides of ~300 μm) at 2 frames per second for most visual stimuli, except for high-speed acquisitions (30 fps) in dedicated recordings. To minimize light contamination from the visual stimulation display, a small black fabric curtain was mounted around the objective and gently lowered to cover the gap between the objective and the mouse's head, without obstructing the animal's eye. This simple shielding effectively reduced the number of stray photons from the screen reaching the objective and thus minimized potential stimulus-induced artefacts in the imaging signal. The rotary encoder signal was analyzed using a custom MATLAB pipeline to compute locomotion speed and position. The analysis extracted instantaneous speed.

Simultaneously, behavioral and synchronization signals were recorded through a Digidata® 1440A Data Acquisition System, including the rotary encoder signal (wheel movement, pre-processed by Arduino), TTL pulses from the visual stimulation system, and galvo mirror signals from the microscope. The wheel movement was monitored with a rotary encoder from which the signal of the position was read by an Arduino, traduced in an analog signal (0-5 V) and sent to the acquisition board.

Visual stimuli were generated through a custom MATLAB application controlling a secondary monitor placed in front of the mouse. An Arduino connected to a phototransistor mounted on the monitor detected the onset of each visual stimulus and produced a TTL pulse through. A TTL was also sent at the start of each trial to trigger microscope acquisition. All TTLs and galvo signals were recorded to enable precise temporal synchronization between visual stimuli and two-photon imaging frames.

Dark acquisitions were analyzed to extract fluorescence-independent signals in both green and red channels using a custom MATLAB script. Average traces were computed across all dark recordings, and dark time series were subtracted from experimental recordings to correct for contaminating signals. In the case of *alternate-dark* acquisition, we repeated the visual stimulation protocol with an optomechanical hard shutter placed in the laser beam path upstream of the microscope entrance. The shutter was controlled by an Arduino board, programmed to open and close alternately on a frame-by-frame basis, such that every other frame was acquired with the laser completely blocked ("dark frame").

ROIs were automatically extracted from movies using a custom MATLAB routine. For each ROI, average red and green fluorescence traces were calculated by averaging pixel intensity within the ROI mask. For each ROI and trial, red and green fluorescence signals were dark-subtracted. The ratio signal (R = G/R) was computed and normalized to the baseline period preceding stimulus onset to yield ΔR/R traces:

$$\frac{\Delta R}{R_0} = \frac{R - R_0}{R_0}$$

where $R_0$is the mean ratio during baseline frames. Traces were then averaged across trials and ROIs to obtain mean session responses. The imaging and stimulus timing were synchronized via the recorded TTL and galvo channels. Mice average responses were analyzed to extract peak amplitude, time-to-peak, and decay constant. Decay kinetics were fit with a single-exponential model. In trials where locomotion-elicited transients were

detected, the R_0 measured in the “not-running” trials was used. In this way it was possible to compare the two conditions.

Baseline $[Cl^-]_i$ was estimated from the average baseline ratio R_{Cl} assuming a fixed intracellular pH, according to Eq. 5 of the iClima calibration model. R_{Cl} was recalculated according to the response peak, and was used to compute variations in intracellular chloride during visual stimulation and locomotion.

5.14 Visual stimulation

Visual stimuli were generated using a custom MATLAB application developed in the laboratory. The application, interfaced with an Arduino board, used Psychtoolbox to render and control visual stimuli presented on a calibrated LCD monitor. The monitor was positioned 30 cm in front of the animal, such that the contralateral eye relative to the imaged visual cortex was facing the screen. To synchronize visual stimulation with two-photon imaging, the MATLAB application modulated the luminance of a small, hidden corner of the screen at specific time points, at the beginning of each trial (baseline onset) and at the onset of each visual stimulus. This patch was not visible to the animal, as it was covered by an opaque mask and coupled to a phototransistor placed directly in front of it. The phototransistor continuously monitored screen luminance and sent its analog output to an Arduino board, which detected threshold crossings. Whenever the signal exceeded a predefined threshold, the Arduino generated a TTL pulse that was recorded via the acquisition system. These TTLs provided precise temporal markers to align visual stimulus presentation with the imaging frames and/or electrophysiological recordings.

Two main types of visual stimuli were used:

1. Luminance step: The monitor luminance was set close to 0 cd/m² during a 30 s baseline period, followed by a 20 s full-field luminance step to 10 cd/m². This was followed by a 20 s recovery period during which the luminance returned to 0 cd/m².
2. Moving grating (Grid 0°): A full-field drifting grating stimulus moving from tail to head (referred to as *grid 0°*) was presented. The baseline preceding the stimulus consisted of a uniform gray screen of 5 cd/m² mean luminance for 30 s. Gratings (0.02 cycles/deg square wave) were shown for either 5 s or 10 s, depending on the experimental protocol, and drifted at a temporal frequency of 2 cycles/degree. The grating alternated between white (10 cd/m²) and black (~0 cd/m²) bars, resulting in a ~100% contrast stimulus.

All stimulus parameters (onset, duration, luminance, and motion direction) were controlled programmatically by the MATLAB application.

5.15 Gamma and multi-unit experiments

Recordings were performed in C57BL/6J mice (n = 6), starting from 4 weeks of age (young adult stage). Animals were anesthetized with urethane (1.6 g/kg, i.p.) and placed in a stereotaxic frame. A small craniotomy was made above the primary visual cortex (V1), and the exposed cortex was kept moist with sterile saline throughout the experiment.

Extracellular signals were recorded using 16-channel silicon probes (single-shank MEA, Neuronexus A1x16-3mm-25-177). The probe was inserted perpendicularly into the cortical surface to span approximately 450 µm. Signals were amplified and digitized at 30 kHz using the SmartBox Pro acquisition system (Neuronexus Technologies), and recordings were managed through SmartBox Control software (Allego) for real-time monitoring and data storage. Visual stimuli were presented following the same procedure described in method session 5.14. In brief, stimulation consisted of a step of steady light (10 cd/m², 20 s duration) displayed on a dark background. For each mouse, at least two sessions of 5 trials each were recorded.

For gamma-band analysis, the LFPs from all recorded electrodes were pre-processed using a custom MATLAB GUI developed in the laboratory. LFP signals were band-pass filtered between 20–48 Hz to isolate low-gamma oscillations. Power in this band was computed in sliding windows (window size: 0.2 s; step: 0.05 s) and normalized to pre-stimulus baseline activity, defined in the [–1.8, –0.2 s] interval before stimulus onset. For each session, power traces were averaged across channels and across trials, yielding a mean response per session. These session averages were then further averaged across all sessions recorded from the same animal to obtain an individual mean gamma response for each mouse. Group averages and standard deviations were then computed across all animals (as shown in **Figure 23**d). The resulting gamma-band temporal profiles were integrated around stimulus onset and offset windows, normalized to their peak amplitude, and compared with the corresponding chloride fluctuation curves obtained from imaging data.

MUA signals were extracted using the same laboratory-developed MATLAB GUI. The wideband LFP signal was high-pass filtered between 300 and 3000 Hz. Spike detection was based on a thresholding method (Quiroga et al., 2004), where the noise level (σ) was estimated as the median of the absolute signal divided by 0.6745, which is a fast method to compute the median absolute deviation for normally distributed samples. The detection threshold was then defined as $\mathrm{Thr} = N \times \sigma$, with N=4 in my analysis. Detected spikes within a refractory period (2 ms) were grouped. For MUA extraction, all spikes exceeding threshold were considered without clustering into single units (i.e., all spikes were treated as belonging to one population of active units per channel). For each channel, a raster matrix (trials × time) was generated, and a Gaussian kernel (σ = 0.05 s) was used to smooth the spike trains, yielding a continuous estimate of firing probability over time (“integrated MUA probability”). Only channels 10–16 were included in the analysis (layer II/III/IV), as these displayed the highest spike activity. For each mouse, the MUA probability traces were averaged across the selected channels, trials, and then across all sessions, producing an average MUA response per animal. Finally, individual animal averages were pooled to compute the group mean, which are shown in **Figure 23**c.

6. Bibliography

Alfonsa, H., Burman, R. J., Brodersen, P. J. N., Newey, S. E., Mahfooz, K., Yamagata, T., Panayi, M. C., Bannerman, D. M., Vyazovskiy, V. V., & Akerman, C. J. (2023). Intracellular chloride regulation mediates local sleep pressure in the cortex. *Nature Neuroscience*, *26*(1), 64–78. https://doi.org/10.1038/s41593-022-01214-2

Alfonsa, H., Chakrabarty, A., Vyazovskiy, V. V., & Akerman, C. J. (2025). Sleep-wake-related changes in intracellular chloride regulate plasticity at glutamatergic cortical synapses. *Current Biology*, *35*(6), 1373-1381.e3. https://doi.org/10.1016/j.cub.2025.01.050

Anderson, S. A., Eisenstat, D. D., Shi, L., & Rubenstein, J. L. R. (1997). Interneuron Migration from Basal Forebrain to Neocortex: Dependence on *Dlx* Genes. *Science*, *278*(5337), 474–476. https://doi.org/10.1126/science.278.5337.474

Arosio, D., & Ratto, G. M. (2014). Twenty years of fluorescence imaging of intracellular chloride. *Frontiers in Cellular Neuroscience*, *8*. https://doi.org/10.3389/fncel.2014.00258

Arosio, D., Ricci, F., Marchetti, L., Gualdani, R., Albertazzi, L., & Beltram, F. (2010). Simultaneous intracellular chloride and pH measurements using a GFP-based sensor. *Nature Methods*, *7*(7), 516–518. https://doi.org/10.1038/nmeth.1471

Ascoli, G. A., Alonso-Nanclares, L., Anderson, S. A., Barrionuevo, G., Benavides-Piccione, R., Burkhalter, A., Buzsáki, G., Cauli, B., DeFelipe, J., Fairén, A., Feldmeyer, D., Fishell, G., Fregnac, Y., Freund, T. F., Gardner, D., Gardner, E. P., Goldberg, J. H., Helmstaedter, M., Hestrin, S., … The Petilla Interneuron Nomenclature Group (PING). (2008). Petilla terminology: Nomenclature of features of GABAergic interneurons of the cerebral cortex. *Nature Reviews Neuroscience*, *9*(7), 557–568. https://doi.org/10.1038/nrn2402

Ashton, T. D., Jolliffe, K. A., & Pfeffer, F. M. (2015). Luminescent probes for the bioimaging of small anionic species in vitro and in vivo. *Chemical Society Reviews*, *44*(14), 4547–4595. https://doi.org/10.1039/C4CS00372A

Avoli, M. (1996). GABA-Mediated Synchronous Potentials and Seizure Generation. *Epilepsia*, *37*(11), 1035–1042. https://doi.org/10.1111/j.1528-1157.1996.tb01022.x

Balena, T., & Woodin, M. A. (2008). Coincident pre- and postsynaptic activity downregulates NKCC1 to hyperpolarize ECl during development. *European Journal of Neuroscience*, *27*(9), 2402–2412. https://doi.org/10.1111/j.1460-9568.2008.06194.x

Bekar, L. K., & Walz, W. (2002). Intracellular chloride modulates A-type potassium currents in astrocytes. *Glia*, *39*(3), 207–216. https://doi.org/10.1002/glia.10096

Belenky, M. A., Sollars, P. J., Mount, D. B., Alper, S. L., Yarom, Y., & Pickard, G. E. (2010). Cell-type specific distribution of chloride transporters in the rat suprachiasmatic nucleus. *Neuroscience*, *165*(4), 1519–1537. https://doi.org/10.1016/j.neuroscience.2009.11.040

Ben-Ari, Y. (2001). Developing networks play a similar melody. *Trends in Neurosciences*, *24*(6), 353–360. https://doi.org/10.1016/s0166-2236(00)01813-0

Ben-Ari, Y. (2002). Excitatory actions of gaba during development: The nature of the nurture. *Nature Reviews Neuroscience*, *3*(9), 728–739. https://doi.org/10.1038/nrn920

Ben-Ari, Y. (2017). NKCC1 Chloride Importer Antagonists Attenuate Many Neurological and Psychiatric Disorders. *Trends in Neurosciences*, *40*(9), 536–554. https://doi.org/10.1016/j.tins.2017.07.001

Ben-Ari, Y., Cherubini, E., Corradetti, R., & Gaiarsa, J. L. (1989). Giant synaptic potentials in immature rat CA3 hippocampal neurones. *The Journal of Physiology*, *416*(1), 303–325. https://doi.org/10.1113/jphysiol.1989.sp017762

Ben-Ari, Y., Khalilov, I., Kahle, K. T., & Cherubini, E. (2012). The GABA excitatory/inhibitory shift in brain maturation and neurological disorders. *The Neuroscientist: A Review Journal Bringing Neurobiology, Neurology and Psychiatry*, *18*(5), 467–486. https://doi.org/10.1177/1073858412438697

Biwersi, J., Tulk, B., & Verkman, A. S. (1994). Long-wavelength chloride-sensitive fluorescent indicators. *Analytical Biochemistry*, *219*(1), 139–143. https://doi.org/10.1006/abio.1994.1242

Blaesse, P., Airaksinen, M. S., Rivera, C., & Kaila, K. (2009). Cation-Chloride Cotransporters and Neuronal Function. *Neuron*, *61*(6), 820–838. https://doi.org/10.1016/j.neuron.2009.03.003

Bortone, D. S., Olsen, S. R., & Scanziani, M. (2014). Translaminar Inhibitory Cells Recruited by Layer 6 Corticothalamic Neurons Suppress Visual Cortex. *Neuron*, *82*(2), 474–485. https://doi.org/10.1016/j.neuron.2014.02.021

Boyd-Shiwarski, C. R., Shiwarski, D. J., Griffiths, S. E., Beacham, R. T., Norrell, L., Morrison, D. E., Wang, J., Mann, J., Tennant, W., Anderson, E. N., Franks, J., Calderon, M., Connolly, K. A., Cheema, M. U., Weaver, C. J., Nkashama, L. J., Weckerly, C. C., Querry, K. E., Pandey, U. B., … Subramanya, A. R. (2022). WNK kinases sense molecular crowding and rescue cell volume via phase separation. *Cell*, *185*(24), 4488-4506.e20. https://doi.org/10.1016/j.cell.2022.09.042

Bugeon, S., Duffield, J., Dipoppa, M., Ritoux, A., Prankerd, I., Nicoloutsopoulos, D., Orme, D., Shinn, M., Peng, H., Forrest, H., Viduolyte, A., Reddy, C. B., Isogai, Y., Carandini, M., & Harris, K. D. (2022). A transcriptomic axis predicts state modulation of cortical interneurons. *Nature*, *607*(7918), 330–338. https://doi.org/10.1038/s41586-022-04915-7

Buzsáki, G., & Wang, X.-J. (2012). Mechanisms of Gamma Oscillations. *Annual Review of Neuroscience*, *35*(1), 203–225. https://doi.org/10.1146/annurev-neuro-062111-150444

Chen, T.-W., Wardill, T. J., Sun, Y., Pulver, S. R., Renninger, S. L., Baohan, A., Schreiter, E. R., Kerr, R. A., Orger, M. B., Jayaraman, V., Looger, L. L., Svoboda, K., & Kim, D. S. (2013). Ultrasensitive fluorescent proteins for imaging neuronal activity. *Nature*, *499*(7458), 295–300. https://doi.org/10.1038/nature12354

Cherubini, E., Gaiarsa, J. L., & Ben-Aft, Y. (1991). *GABA:an exdtatory transmitterin earlypostnatallife*. *14*(12).

Clavel, D., Gotthard, G., Von Stetten, D., De Sanctis, D., Pasquier, H., Lambert, G. G., Shaner, N. C., & Royant, A. (2016). Structural analysis of the bright monomeric yellow-green fluorescent

protein mNeonGreen obtained by directed evolution. *Acta Crystallographica Section D Structural Biology*, *72*(12), 1298–1307. https://doi.org/10.1107/S2059798316018623

Colwell, C. S. (2011). Linking neural activity and molecular oscillations in the SCN. *Nature Reviews Neuroscience*, *12*(10), 553–569. https://doi.org/10.1038/nrn3086

Dal Maschio, M., Ghezzi, D., Bony, G., Alabastri, A., Deidda, G., Brondi, M., Sato, S. S., Zaccaria, R. P., Di Fabrizio, E., Ratto, G. M., & Cancedda, L. (2012). High-performance and site-directed in utero electroporation by a triple-electrode probe. *Nature Communications*, *3*(1), 960. https://doi.org/10.1038/ncomms1961

Debski, K. J., Ceglia, N., Ghestem, A., Ivanov, A. I., Brancati, G. E., Bröer, S., Bot, A. M., Müller, J. A., Schoch, S., Becker, A., Löscher, W., Guye, M., Sassone-Corsi, P., Lukasiuk, K., Baldi, P., & Bernard, C. (2020). The circadian dynamics of the hippocampal transcriptome and proteome is altered in experimental temporal lobe epilepsy. *Science Advances*, *6*(41), eaat5979. https://doi.org/10.1126/sciadv.aat5979

DeFelipe, J., López-Cruz, P. L., Benavides-Piccione, R., Bielza, C., Larrañaga, P., Anderson, S., Burkhalter, A., Cauli, B., Fairén, A., Feldmeyer, D., Fishell, G., Fitzpatrick, D., Freund, T. F., González-Burgos, G., Hestrin, S., Hill, S., Hof, P. R., Huang, J., Jones, E. G., … Ascoli, G. A. (2013). New insights into the classification and nomenclature of cortical GABAergic interneurons. *Nature Reviews Neuroscience*, *14*(3), 202–216. https://doi.org/10.1038/nrn3444

Delpire, E., & Staley, K. J. (2014). Novel determinants of the neuronal Cl− concentration. *The Journal of Physiology*, *592*(Pt 19), 4099–4114. https://doi.org/10.1113/jphysiol.2014.275529

Dipoppa, M., Ranson, A., Krumin, M., Pachitariu, M., Carandini, M., & Harris, K. D. (2018). Vision and Locomotion Shape the Interactions between Neuron Types in Mouse Visual Cortex. *Neuron*, *98*(3), 602-615.e8. https://doi.org/10.1016/j.neuron.2018.03.037

Doyon, N., Vinay, L., Prescott, S. A., & De Koninck, Y. (2016). Chloride Regulation: A Dynamic Equilibrium Crucial for Synaptic Inhibition. *Neuron*, *89*(6), 1157–1172. https://doi.org/10.1016/j.neuron.2016.02.030

Feeney, K. A., Hansen, L. L., Putker, M., Olivares-Yañez, C., Day, J., Eades, L. J., Larrondo, L. F., Hoyle, N. P., O'Neill, J. S., & van Ooijen, G. (2016). Daily magnesium fluxes regulate cellular timekeeping and energy balance. *Nature*, *532*(7599), 375–379. https://doi.org/10.1038/nature17407

Fisher, S. P., Godinho, S. I. H., Pothecary, C. A., Hankins, M. W., Foster, R. G., & Peirson, S. N. (2012). Rapid Assessment of Sleep-Wake Behavior in Mice. *Journal of Biological Rhythms*, *27*(1), 48–58. https://doi.org/10.1177/0748730411431550

Fiumelli, H., Cancedda, L., & Poo, M. (2005). Modulation of GABAergic transmission by activity via postsynaptic Ca2+-dependent regulation of KCC2 function. *Neuron*, *48*(5), 773–786. https://doi.org/10.1016/j.neuron.2005.10.025

Fiumelli, H., & Woodin, M. A. (2007). Role of activity-dependent regulation of neuronal chloride homeostasis in development. *Current Opinion in Neurobiology*, *17*(1), 81–86. https://doi.org/10.1016/j.conb.2007.01.002

Flemmer, A. W., Giménez, I., Dowd, B. F. X., Darman, R. B., & Forbush, B. (2002). Activation of the Na-K-Cl Cotransporter NKCC1 Detected with a Phospho-specific Antibody. *Journal of Biological Chemistry*, *277*(40), 37551–37558. https://doi.org/10.1074/jbc.M206294200

Franks, N. P., & Lieb, W. R. (1994). Molecular and cellular mechanisms of general anaesthesia. *Nature*, *367*(6464), 607–614. https://doi.org/10.1038/367607a0

Fries, P. (2015). Rhythms for Cognition: Communication through Coherence. *Neuron*, *88*(1), 220–235. https://doi.org/10.1016/j.neuron.2015.09.034

Fu, Y., Tucciarone, J. M., Espinosa, J. S., Sheng, N., Darcy, D. P., Nicoll, R. A., Huang, Z. J., & Stryker, M. P. (2014). A Cortical Circuit for Gain Control by Behavioral State. *Cell*, *156*(6), 1139–1152. https://doi.org/10.1016/j.cell.2014.01.050

Galietta, L. J. V., Haggie, P. M., & Verkman, A. S. (2001). Green fluorescent protein-based halide indicators with improved chloride and iodide affinities. *FEBS Letters*, *499*(3), 220–224. https://doi.org/10.1016/S0014-5793(01)02561-3

Geddes, C. D., Apperson, K., Karolin, J., & Birch, D. J. S. (2001). Chloride-Sensitive Fluorescent Indicators. *Analytical Biochemistry*, *293*(1), 60–66. https://doi.org/10.1006/abio.2001.5103

Green, D. J., & Gillette, R. (1982). Circadian rhythm of firing rate recorded from single cells in the rat suprachiasmatic brain slice. *Brain Research*, *245*(1), 198–200. https://doi.org/10.1016/0006-8993(82)90361-4

Grimley, J. S., Li, L., Wang, W., Wen, L., Beese, L. S., Hellinga, H. W., & Augustine, G. J. (2013). Visualization of Synaptic Inhibition with an Optogenetic Sensor Developed by Cell-Free Protein Engineering Automation. *The Journal of Neuroscience*, *33*(41), 16297–16309. https://doi.org/10.1523/JNEUROSCI.4616-11.2013

Harbour, V. L., Weigl, Y., Robinson, B., & Amir, S. (2014). Phase Differences in Expression of Circadian Clock Genes in the Central Nucleus of the Amygdala, Dentate Gyrus, and Suprachiasmatic Nucleus in the Rat. *PLoS ONE*, *9*(7), e103309. https://doi.org/10.1371/journal.pone.0103309

Hartsock, M. J., & Spencer, R. L. (2020). Memory and the circadian system: Identifying candidate mechanisms by which local clocks in the brain may regulate synaptic plasticity. *Neuroscience & Biobehavioral Reviews*, *118*, 134–162. https://doi.org/10.1016/j.neubiorev.2020.07.023

Hasan, S., Veen, D. R., Winsky-Sommerer, R., Hogben, A., Laing, E. E., Koentgen, F., Dijk, D., & Archer, S. N. (2014). A human sleep homeostasis phenotype in mice expressing a primate-specific *PER3* variable-number tandem-repeat coding-region polymorphism. *The FASEB Journal*, *28*(6), 2441–2454. https://doi.org/10.1096/fj.13-240135

Hattar, S., Liao, H.-W., Takao, M., Berson, D. M., & Yau, K.-W. (2002). Melanopsin-Containing Retinal Ganglion Cells: Architecture, Projections, and Intrinsic Photosensitivity. *Science*, *295*(5557), 1065–1070. https://doi.org/10.1126/science.1069609

Herstel, L. J., Peerboom, C., Uijtewaal, S., Selemangel, D., Karst, H., & Wierenga, C. J. (2022). Using SuperClomeleon to Measure Changes in Intracellular Chloride during Development and after Early Life Stress. *Eneuro*, *9*(6), ENEURO.0416-22.2022. https://doi.org/10.1523/ENEURO.0416-22.2022

Heubl, M., Zhang, J., Pressey, J. C., Al Awabdh, S., Renner, M., Gomez-Castro, F., Moutkine, I., Eugène, E., Russeau, M., Kahle, K. T., Poncer, J. C., & Lévi, S. (2017). GABAA receptor dependent synaptic inhibition rapidly tunes KCC2 activity via the Cl−-sensitive WNK1 kinase. *Nature Communications*, *8*(1), 1776. https://doi.org/10.1038/s41467-017-01749-0

Hu, H., Gan, J., & Jonas, P. (2014). Fast-spiking, parvalbumin^{+} GABAergic interneurons: From cellular design to microcircuit function. *Science*, *345*(6196), 1255263. https://doi.org/10.1126/science.1255263

Huang, H., Song, S., Banerjee, S., Jiang, T., Zhang, J., Kahle, K. T., Sun, D., & Zhang, Z. (2019). The WNK-SPAK/OSR1 Kinases and the Cation-Chloride Cotransporters as Therapeutic Targets for Neurological Diseases. *Aging and Disease*, *10*(3), 626. https://doi.org/10.14336/AD.2018.0928

Huber, R., Felice Ghilardi, M., Massimini, M., & Tononi, G. (2004). Local sleep and learning. *Nature*, *430*(6995), 78–81. https://doi.org/10.1038/nature02663

Hyde, T. M., Lipska, B. K., Ali, T., Mathew, S. V., Law, A. J., Metitiri, O. E., Straub, R. E., Ye, T., Colantuoni, C., Herman, M. M., Bigelow, L. B., Weinberger, D. R., & Kleinman, J. E. (2011). Expression of GABA Signaling Molecules KCC2, NKCC1, and GAD1 in Cortical Development and Schizophrenia. *Journal of Neuroscience*, *31*(30), 11088–11095. https://doi.org/10.1523/JNEUROSCI.1234-11.2011

Illsley, N. P., & Verkman, A. S. (1987). Membrane chloride transport measured using a chloride-sensitive fluorescent probe. *Biochemistry*, *26*(5), 1215–1219. https://doi.org/10.1021/bi00379a002

Inglefield, J. R., & Schwartz-Bloom, R. D. (1999). Using confocal microscopy and the fluorescent indicator, 6-methoxy-N-ethylquinolinium iodide, to measure changes in intracellular chloride. *Methods in Enzymology*, *307*, 469–481. https://doi.org/10.1016/s0076-6879(99)07028-7

James, N. R., & O'Neill, J. S. (2025). Circadian Control of Protein Synthesis. *BioEssays*, *47*(3), e202300158. https://doi.org/10.1002/bies.202300158

Jayaraman, S., Biwersi, J., & Verkman, A. S. (1999). Synthesis and characterization of dual-wavelength Cl^{-} -sensitive fluorescent indicators for ratio imaging. *American Journal of Physiology-Cell Physiology*, *276*(3), C747–C757. https://doi.org/10.1152/ajpcell.1999.276.3.C747

Jia, F., Yue, M., Chandra, D., Homanics, G. E., Goldstein, P. A., & Harrison, N. L. (2008). Isoflurane Is a Potent Modulator of Extrasynaptic GABAA Receptors in the Thalamus. *The Journal of Pharmacology and Experimental Therapeutics*, *324*(3), 1127–1135. https://doi.org/10.1124/jpet.107.134569

Jones, J. R., Simon, T., Lones, L., & Herzog, E. D. (2018). SCN VIP Neurons Are Essential for Normal Light-Mediated Resetting of the Circadian System. *The Journal of Neuroscience*, *38*(37), 7986–7995. https://doi.org/10.1523/JNEUROSCI.1322-18.2018

Jones, M. V., & Harrison, N. L. (1993). Effects of volatile anesthetics on the kinetics of inhibitory postsynaptic currents in cultured rat hippocampal neurons. *Journal of Neurophysiology*, *70*(4), 1339–1349. https://doi.org/10.1152/jn.1993.70.4.1339

Kahle, K. T., Merner, N. D., Friedel, P., Silayeva, L., Liang, B., Khanna, A., Shang, Y., Lachance-Touchette, P., Bourassa, C., Levert, A., Dion, P. A., Walcott, B., Spiegelman, D., Dionne-Laporte, A., Hodgkinson, A., Awadalla, P., Nikbakht, H., Majewski, J., Cossette, P., … Rouleau, G. A.

(2014). Genetically encoded impairment of neuronal KCC 2 cotransporter function in human idiopathic generalized epilepsy. *EMBO Reports*, *15*(7), 766–774. https://doi.org/10.15252/embr.201438840

Kahle, K. T., & Staley, K. (2008). Altered Neuronal Chloride Homeostasis and Excitatory GABAergic Signaling in Human Temporal Lobe Epilepsy. *Epilepsy Currents*, *8*(2), 51–53. https://doi.org/10.1111/j.1535-7511.2008.00235.x

Kaila, K. (1994). Ionic basis of GABAA receptor channel function in the nervous system. *Progress in Neurobiology*, *42*(4), 489–537. https://doi.org/10.1016/0301-0082(94)90049-3

Kaila, K., Lamsa, K., Smirnov, S., Taira, T., & Voipio, J. (1997). Long-lasting GABA-mediated depolarization evoked by high-frequency stimulation in pyramidal neurons of rat hippocampal slice is attributable to a network-driven, bicarbonate-dependent K+ transient. *The Journal of Neuroscience: The Official Journal of the Society for Neuroscience*, *17*(20), 7662–7672.

Kaila, K., Price, T. J., Payne, J. A., Puskarjov, M., & Voipio, J. (2014). Cation-chloride cotransporters in neuronal development, plasticity and disease. *Nature Reviews Neuroscience*, *15*(10), 637–654. https://doi.org/10.1038/nrn3819

Kaila, K., & Voipio, J. (1987). Postsynaptic fall in intracellular pH induced by GABA-activated bicarbonate conductance. *Nature*, *330*(6144), 163–165. https://doi.org/10.1038/330163a0

Kandel, E. R., Koester, J. D., Mack, S. H., & Siegelbaum, S. A. (2021). *Principles of Neural Science, Sixth Edition* (6° edizione). McGraw-Hill Education / Medical.

Kaneko, H., Putzier, I., Frings, S., Kaupp, U. B., & Gensch, T. (2004). Chloride Accumulation in Mammalian Olfactory Sensory Neurons. *The Journal of Neuroscience*, *24*(36), 7931–7938. https://doi.org/10.1523/JNEUROSCI.2115-04.2004

Kapur, J., & Coulter, D. A. (1995). Experimental status epilepticus alters gamma-aminobutyric acid type A receptor function in CA1 pyramidal neurons. *Annals of Neurology*, *38*(6), 893–900. https://doi.org/10.1002/ana.410380609

Karoly, P. J., Rao, V. R., Gregg, N. M., Worrell, G. A., Bernard, C., Cook, M. J., & Baud, M. O. (2021). Cycles in epilepsy. *Nature Reviews Neurology*, *17*(5), 267–284. https://doi.org/10.1038/s41582-021-00464-1

Kennelly, K. P., Wallace, D. M., Holmes, T. M., Hankey, D. J., Grant, T. S., O'Farrelly, C., & Keegan, D. J. (2011). Preparation of Pre-Confluent Retinal Cells Increases Graft Viability In Vitro and In Vivo: A Mouse Model. *PLoS ONE*, *6*(6), e21365. https://doi.org/10.1371/journal.pone.0021365

Kerlin, A. M., Andermann, M. L., Berezovskii, V. K., & Reid, R. C. (2010). Broadly Tuned Response Properties of Diverse Inhibitory Neuron Subtypes in Mouse Visual Cortex. *Neuron*, *67*(5), 858–871. https://doi.org/10.1016/j.neuron.2010.08.002

Kim, E., Yoo, S.-H., & Chen, Z. (2022). *Circadian stabilization loop: The regulatory hub and therapeutic target promoting circadian resilience and physiological health*. *F1000research*.

Klett, N. J., & Allen, C. N. (2017). Intracellular Chloride Regulation in AVP+ and VIP+ Neurons of the Suprachiasmatic Nucleus. *Scientific Reports*, *7*(1), 10226. https://doi.org/10.1038/s41598-017-09778-x

Klett, N. J., Cravetchi, O., & Allen, C. N. (2022). Long-Term Imaging Reveals a Circadian Rhythm of Intracellular Chloride in Neurons of the Suprachiasmatic Nucleus. *Journal of Biological Rhythms*, *37*(1), 110–123. https://doi.org/10.1177/07487304211059770

Krapf, R., Berry, C. A., & Verkman, A. S. (1988). Estimation of intracellular chloride activity in isolated perfused rabbit proximal convoluted tubules using a fluorescent indicator. *Biophysical Journal*, *53*(6), 955–962. https://doi.org/10.1016/S0006-3495(88)83176-X

Kuner, T., & Augustine, G. J. (n.d.). *A Genetically Encoded Ratiometric Neurotechnique Indicator for Chloride: Capturing Chloride Transients in Cultured Hippocampal Neurons*.

Kuner, T., & Augustine, G. J. (2000). *A Genetically Encoded Ratiometric Neurotechnique Indicator for Chloride: Capturing Chloride Transients in Cultured Hippocampal Neurons*.

Lambert, T. J. (2019). FPbase: A community-editable fluorescent protein database. *Nature Methods*, *16*(4), 277–278. https://doi.org/10.1038/s41592-019-0352-8

Lee, H. H. C., Walker, J. A., Williams, J. R., Goodier, R. J., Payne, J. A., & Moss, S. J. (2007). Direct Protein Kinase C-dependent Phosphorylation Regulates the Cell Surface Stability and Activity of the Potassium Chloride Cotransporter KCC2. *Journal of Biological Chemistry*, *282*(41), 29777–29784. https://doi.org/10.1074/jbc.M705053200

LeGates, T. A., Fernandez, D. C., & Hattar, S. (2014). Light as a central modulator of circadian rhythms, sleep and affect. *Nature Reviews Neuroscience*, *15*(7), 443–454. https://doi.org/10.1038/nrn3743

Leonzino, M., Busnelli, M., Antonucci, F., Verderio, C., Mazzanti, M., & Chini, B. (2016). The Timing of the Excitatory-to-Inhibitory GABA Switch Is Regulated by the Oxytocin Receptor via KCC2. *Cell Reports*, *15*(1), 96–103. https://doi.org/10.1016/j.celrep.2016.03.013

Letzkus, J. J., Wolff, S. B. E., Meyer, E. M. M., Tovote, P., Courtin, J., Herry, C., & Lüthi, A. (2011). A disinhibitory microcircuit for associative fear learning in the auditory cortex. *Nature*, *480*(7377), 331–335. https://doi.org/10.1038/nature10674

Li, P., Fu, X., Smith, N. A., Ziobro, J., Curiel, J., Tenga, M. J., Martin, B., Freedman, S., Cea-Del Rio, C. A., Oboti, L., Tsuchida, T. N., Oluigbo, C., Yaun, A., Magge, S. N., O'Neill, B., Kao, A., Zelleke, T. G., Depositario-Cabacar, D. T., Ghimbovschi, S., … Liu, J. S. (2017). Loss of CLOCK Results in Dysfunction of Brain Circuits Underlying Focal Epilepsy. *Neuron*, *96*(2), 387-401.e6. https://doi.org/10.1016/j.neuron.2017.09.044

Lillis, K. P., Kramer, M. A., Mertz, J., Staley, K. J., & White, J. A. (2012). Pyramidal cells accumulate chloride at seizure onset. *Neurobiology of Disease*, *47*(3), 358–366. https://doi.org/10.1016/j.nbd.2012.05.016

Lim, L., Mi, D., Llorca, A., & Marín, O. (2018). Development and Functional Diversification of Cortical Interneurons. *Neuron*, *100*(2), 294–313. https://doi.org/10.1016/j.neuron.2018.10.009

Liu, B., Li, Y., Ma, W., Pan, C., Zhang, L. I., & Tao, H. W. (2011). Broad Inhibition Sharpens Orientation Selectivity by Expanding Input Dynamic Range in Mouse Simple Cells. *Neuron*, *71*(3), 542–554. https://doi.org/10.1016/j.neuron.2011.06.017

Llorca, A., & Deogracias, R. (2022). Origin, Development, and Synaptogenesis of Cortical Interneurons. *Frontiers in Neuroscience*, *16*, 929469. https://doi.org/10.3389/fnins.2022.929469

Lodovichi, C., Ratto, G. M., Trevelyan, A. J., & Arosio, D. (2022). Genetically encoded sensors for Chloride concentration. *Journal of Neuroscience Methods*, *368*, 109455. https://doi.org/10.1016/j.jneumeth.2021.109455

Lüscher, B. P., Vachel, L., Ohana, E., & Muallem, S. (2020). Cl^- as a bona fide signaling ion. *American Journal of Physiology-Cell Physiology*, *318*(1), C125–C136. https://doi.org/10.1152/ajpcell.00354.2019

Mendelson, W. B., Guthrie, R. D., Frederick, G., & Jed Wyatt, R. (1974). The flower pot technique of Rapid Eye Movement (REM) sleep deprivation. *Pharmacology Biochemistry and Behavior*, *2*(4), 553–556. https://doi.org/10.1016/0091-3057(74)90018-5

Nagoshi, E., Saini, C., Bauer, C., Laroche, T., Naef, F., & Schibler, U. (2004). Circadian Gene Expression in Individual Fibroblasts. *Cell*, *119*(5), 693–705. https://doi.org/10.1016/j.cell.2004.11.015

Nyuyki, K. D., Maloumby, R., Reber, S. O., & Neumann, I. D. (2012). Comparison of corticosterone responses to acute stressors: Chronic jugular vein versus trunk blood samples in mice. *Stress*, *15*(6), 618–626. https://doi.org/10.3109/10253890.2012.655348

Okabe, A., Yokokura, M., Toyoda, H., Shimizu-Okabe, C., Ohno, K., Sato, K., & Fukuda, A. (2003). Changes in chloride homeostasis-regulating gene expressions in the rat hippocampus following amygdala kindling. *Brain Research*, *990*(1–2), 221–226. https://doi.org/10.1016/S0006-8993(03)03528-5

Onorato, I., Tzanou, A., Schneider, M., Uran, C., Broggini, A. C., & Vinck, M. (2025). Distinct roles of PV and Sst interneurons in visually induced gamma oscillations. *Cell Reports*, *44*(3), 115385. https://doi.org/10.1016/j.celrep.2025.115385

Pack, A. I., Galante, R. J., Maislin, G., Cater, J., Metaxas, D., Lu, S., Zhang, L., Smith, R. V., Kay, T., Lian, J., Svenson, K., & Peters, L. L. (2007). Novel method for high-throughput phenotyping of sleep in mice. *Physiological Genomics*, *28*(2), 232–238. https://doi.org/10.1152/physiolgenomics.00139.2006

Pakan, J. M., Lowe, S. C., Dylda, E., Keemink, S. W., Currie, S. P., Coutts, C. A., & Rochefort, N. L. (2016). Behavioral-state modulation of inhibition is context-dependent and cell type specific in mouse visual cortex. *eLife*, *5*, e14985. https://doi.org/10.7554/eLife.14985

Paredes, J. M., Idilli, A. I., Mariotti, L., Losi, G., Arslanbaeva, L. R., Sato, S. S., Artoni, P., Szczurkowska, J., Cancedda, L., Ratto, G. M., Carmignoto, G., & Arosio, D. (2016). Synchronous Bioimaging of Intracellular pH and Chloride Based on LSS Fluorescent Protein. *ACS Chemical Biology*, *11*(6), 1652–1660. https://doi.org/10.1021/acschembio.6b00103

Partch, C. L., Green, C. B., & Takahashi, J. S. (2014). Molecular architecture of the mammalian circadian clock. *Trends in Cell Biology*, *24*(2), 90–99. https://doi.org/10.1016/j.tcb.2013.07.002

Payne, J. A., Rivera, C., Voipio, J., & Kaila, K. (2003). Cation-chloride co-transporters in neuronal communication, development and trauma. *Trends in Neurosciences*, *26*(4), 199–206. https://doi.org/10.1016/S0166-2236(03)00068-7

Pfeffer, C. K., Xue, M., He, M., Huang, Z. J., & Scanziani, M. (2013). Inhibition of inhibition in visual cortex: The logic of connections between molecularly distinct interneurons. *Nature Neuroscience*, *16*(8), 1068–1076. https://doi.org/10.1038/nn.3446

Piala, A. T., Moon, T. M., Akella, R., He, H., Cobb, M. H., & Goldsmith, E. J. (2014). Chloride Sensing by WNK1 Involves Inhibition of Autophosphorylation. *Science Signaling*, *7*(324). https://doi.org/10.1126/scisignal.2005050

Piatkevich, K. D., Hulit, J., Subach, O. M., Wu, B., Abdulla, A., Segall, J. E., & Verkhusha, V. V. (2010). Monomeric red fluorescent proteins with a large Stokes shift. *Proceedings of the National Academy of Sciences*, *107*(12), 5369–5374. https://doi.org/10.1073/pnas.0914365107

Polack, P.-O., Friedman, J., & Golshani, P. (2013). Cellular mechanisms of brain state–dependent gain modulation in visual cortex. *Nature Neuroscience*, *16*(9), 1331–1339. https://doi.org/10.1038/nn.3464

Pouille, F., Marin-Burgin, A., Adesnik, H., Atallah, B. V., & Scanziani, M. (2009). Input normalization by global feedforward inhibition expands cortical dynamic range. *Nature Neuroscience*, *12*(12), 1577–1585. https://doi.org/10.1038/nn.2441

Pracucci, E., Graham, R., Alberio, L., Nardi, G., Cozzolino, O., Pillai, V., Saieva, L., Walsh, D., Landi, S., Zhang, J., Trevelyan, A. J., & Ratto, G.-M. (2021). *Circadian rhythm in cortical chloride homeostasis underpins variation in network excitability* (p. 2021.05.12.443725). https://doi.org/10.1101/2021.05.12.443725

Pracucci, E., Graham, R. T., Alberio, L., Nardi, G., Cozzolino, O., Pillai, V., Pasquini, G., Saieva, L., Walsh, D., Landi, S., Zhang, J., Trevelyan, A. J., & Ratto, G.-M. (2023). Daily rhythm in cortical chloride homeostasis underpins functional changes in visual cortex excitability. *Nature Communications*, *14*(1), 7108. https://doi.org/10.1038/s41467-023-42711-7

Quiroga, R. Q., Nadasdy, Z., & Ben-Shaul, Y. (2004). Unsupervised Spike Detection and Sorting with Wavelets and Superparamagnetic Clustering. *Neural Computation*, *16*(8), 1661–1687. https://doi.org/10.1162/089976604774201631

Reimer, J., Froudarakis, E., Cadwell, C. R., Yatsenko, D., Denfield, G. H., & Tolias, A. S. (2014). Pupil Fluctuations Track Fast Switching of Cortical States during Quiet Wakefulness. *Neuron*, *84*(2), 355–362. https://doi.org/10.1016/j.neuron.2014.09.033

Rinehart, J., Maksimova, Y. D., Tanis, J. E., Stone, K. L., Hodson, C. A., Zhang, J., Risinger, M., Pan, W., Wu, D., Colangelo, C. M., Forbush, B., Joiner, C. H., Gulcicek, E. E., Gallagher, P. G., & Lifton, R. P. (2009). Sites of regulated phosphorylation that control K-Cl cotransporter activity. *Cell*, *138*(3), 525–536. https://doi.org/10.1016/j.cell.2009.05.031

Rivera, C., Voipio, J., Payne, J. A., Ruusuvuori, E., Lahtinen, H., Lamsa, K., Pirvola, U., Saarma, M., & Kaila, K. (1999). *The K+/ClÐ co-transporter KCC2 renders GABA hyperpolarizing during neuronal maturation*. *397*.

Rivera, C., Voipio, J., Thomas-Crusells, J., Li, H., Emri, Z., Sipilä, S., Payne, J. A., Minichiello, L., Saarma, M., & Kaila, K. (2004). Mechanism of activity-dependent downregulation of the neuron-specific K-Cl cotransporter KCC2. *The Journal of Neuroscience: The Official Journal of the Society for Neuroscience*, *24*(19), 4683–4691. https://doi.org/10.1523/JNEUROSCI.5265-03.2004

Russell, J. M. (2000). *Sodium-Potassium-Chloride Cotransport*. *Physiological Reviews*.

Saha, S., Prakash, V., Halder, S., Chakraborty, K., & Krishnan, Y. (2015). A pH-independent DNA nanodevice for quantifying chloride transport in organelles of living cells. *Nature Nanotechnology*, *10*(7), 645–651. https://doi.org/10.1038/nnano.2015.130

Schmidt-Wilcke, T., Fuchs, E., Funke, K., Vlachos, A., Müller-Dahlhaus, F., Puts, N. A. J., Harris, R. E., & Edden, R. A. E. (2018). GABA—from Inhibition to Cognition: Emerging Concepts. *The Neuroscientist*, *24*(5), 501–515. https://doi.org/10.1177/1073858417734530

Siddique, S. A., Tamilselvan, T., Vishnupriya, M., & Balamurugan, E. (2018). Evaluation of behavior and endocrinological changes after REM sleep deprivation-induced mania-like behavior in mice. *Sleep and Biological Rhythms*, *16*(4), 375–385. https://doi.org/10.1007/s41105-018-0166-6

Sohya, K., Kameyama, K., Yanagawa, Y., Obata, K., & Tsumoto, T. (2007). GABAergic Neurons Are Less Selective to Stimulus Orientation than Excitatory Neurons in Layer II/III of Visual Cortex, as Revealed by *In Vivo* Functional Ca^{2+} Imaging in Transgenic Mice. *The Journal of Neuroscience*, *27*(8), 2145–2149. https://doi.org/10.1523/JNEUROSCI.4641-06.2007

Somogyi, P., Freund, T. F., & Cowey, A. (1982). The axo-axonic interneuron in the cerebral cortex of the rat, cat and monkey. *Neuroscience*, *7*(11), 2577–2607. https://doi.org/10.1016/0306-4522(82)90086-0

Song, S., Miller, K. D., & Abbott, L. F. (2000). Competitive Hebbian learning through spike-timing-dependent synaptic plasticity. *Nature Neuroscience*, *3*(9), 919–926. https://doi.org/10.1038/78829

Staley, K. J., Soldo, B. L., & Proctor, W. R. (1995). Ionic Mechanisms of Neuronal Excitation by Inhibitory $GABA_A$ Receptors. *Science*, *269*(5226), 977–981. https://doi.org/10.1126/science.7638623

Stangherlin, A. (2023). Ion dynamics and the regulation of circadian cellular physiology. *American Journal of Physiology-Cell Physiology*, *324*(3), C632–C643. https://doi.org/10.1152/ajpcell.00378.2022

Stangherlin, A., Watson, J. L., Wong, D. C. S., Barbiero, S., Zeng, A., Seinkmane, E., Chew, S. P., Beale, A. D., Hayter, E. A., Guna, A., Inglis, A. J., Putker, M., Bartolami, E., Matile, S., Lequeux, N., Pons, T., Day, J., van Ooijen, G., Voorhees, R. M., … O'Neill, J. S. (2021). Compensatory ion transport buffers daily protein rhythms to regulate osmotic balance and cellular physiology. *Nature Communications*, *12*(1), 6035. https://doi.org/10.1038/s41467-021-25942-4

Stein, V., & Nicoll, R. A. (2003). GABA generates excitement. *Neuron*, *37*(3), 375–378. https://doi.org/10.1016/s0896-6273(03)00056-4

Subach, O. M., Vlaskina, A. V., Agapova, Y. K., Dorovatovskii, P. V., Nikolaeva, A. Y., Ivashkina, O. I., Popov, V. O., Piatkevich, K. D., Khrenova, M. G., Smirnova, T. A., Boyko, K. M., & Subach, F. V. (2021). LSSmScarlet, dCyRFP2s, dCyOFP2s and CRISPRed2s, Genetically Encoded Red Fluorescent Proteins with a Large Stokes Shift. *International Journal of Molecular Sciences*, *22*(23), 12887. https://doi.org/10.3390/ijms222312887

Sulis Sato, S., Artoni, P., Landi, S., Cozzolino, O., Parra, R., Pracucci, E., Trovato, F., Szczurkowska, J., Luin, S., Arosio, D., Beltram, F., Cancedda, L., Kaila, K., & Ratto, G. M. (2017). Simultaneous two-photon imaging of intracellular chloride concentration and pH in mouse pyramidal neurons in vivo. *Proceedings of the National Academy of Sciences of the United States of America*, *114*(41), E8770–E8779. https://doi.org/10.1073/pnas.1702861114

Tasic, B., Menon, V., Nguyen, T. N., Kim, T. K., Jarsky, T., Yao, Z., Levi, B., Gray, L. T., Sorensen, S. A., Dolbeare, T., Bertagnolli, D., Goldy, J., Shapovalova, N., Parry, S., Lee, C., Smith, K., Bernard, A., Madisen, L., Sunkin, S. M., … Zeng, H. (2016). Adult mouse cortical cell taxonomy revealed by single cell transcriptomics. *Nature Neuroscience*, *19*(2), 335–346. https://doi.org/10.1038/nn.4216

Tononi, G., & Cirelli, C. (2006). Sleep function and synaptic homeostasis. *Sleep Medicine Reviews*, *10*(1), 49–62. https://doi.org/10.1016/j.smrv.2005.05.002

Tremblay, R., Lee, S., & Rudy, B. (2016). GABAergic Interneurons in the Neocortex: From Cellular Properties to Circuits. *Neuron*, *91*(2), 260–292. https://doi.org/10.1016/j.neuron.2016.06.033

Tucker, T. R., & Fitzpatrick, D. (2006). Luminance-Evoked Inhibition in Primary Visual Cortex: A Transient Veto of Simultaneous and Ongoing Response. *The Journal of Neuroscience*, *26*(52), 13537–13547. https://doi.org/10.1523/JNEUROSCI.3723-06.2006

Tutol, J. N., Kam, H. C., & Dodani, S. C. (2019). Identification of mNeonGreen as a pH-Dependent, Turn-On Fluorescent Protein Sensor for Chloride. *ChemBioChem*, *20*(14), 1759–1765. https://doi.org/10.1002/cbic.201900147

Tutol, J. N., Peng, W., & Dodani, S. C. (2019). Discovery and Characterization of a Naturally Occurring, Turn-On Yellow Fluorescent Protein Sensor for Chloride. *Biochemistry*, *58*(1), 31–35. https://doi.org/10.1021/acs.biochem.8b00928

Tyzio, R., Cossart, R., Khalilov, I., Minlebaev, M., Hübner, C. A., Represa, A., Ben-Ari, Y., & Khazipov, R. (2006). Maternal Oxytocin Triggers a Transient Inhibitory Switch in GABA Signaling in the Fetal Brain During Delivery. *Science*, *314*(5806), 1788–1792. https://doi.org/10.1126/science.1133212

Veit, J., Hakim, R., Jadi, M. P., Sejnowski, T. J., & Adesnik, H. (2017). Cortical gamma band synchronization through somatostatin interneurons. *Nature Neuroscience*, *20*(7), 951–959. https://doi.org/10.1038/nn.4562

Verkman, A. S., Sellers, M. C., Chao, A. C., Leung, T., & Ketcham, R. (1989). Synthesis and characterization of improved chloride-sensitive fluorescent indicators for biological applications. *Analytical Biochemistry*, *178*(2), 355–361. https://doi.org/10.1016/0003-2697(89)90652-0

Vyazovskiy, V. V., Olcese, U., Lazimy, Y. M., Faraguna, U., Esser, S. K., Williams, J. C., Cirelli, C., & Tononi, G. (2009). Cortical Firing and Sleep Homeostasis. *Neuron*, *63*(6), 865–878. https://doi.org/10.1016/j.neuron.2009.08.024

Wachter, R. M., & James Remington, S. (1999). Sensitivity of the yellow variant of green fluorescent protein to halides and nitrate. *Current Biology*, *9*(17), R628–R629. https://doi.org/10.1016/S0960-9822(99)80408-4

Wachter, R. M., Yarbrough, D., Kallio, K., & Remington, S. J. (2000). Crystallographic and energetic analysis of binding of selected anions to the yellow variants of green fluorescent protein 1 1Edited by D. C. Rees. *Journal of Molecular Biology*, *301*(1), 157–171. https://doi.org/10.1006/jmbi.2000.3905

Wagner, S., Castel, M., Gainer, H., & Yarom, Y. (1997). GABA in the mammalian suprachiasmatic nucleus and its role in diurnal rhythmicity. *Nature*, *387*(6633), 598–603. https://doi.org/10.1038/42468

Wang, Y., Toledo-Rodriguez, M., Gupta, A., Wu, C., Silberberg, G., Luo, J., & Markram, H. (2004). Anatomical, physiological and molecular properties of Martinotti cells in the somatosensory cortex of the juvenile rat. *The Journal of Physiology*, *561*(1), 65–90. https://doi.org/10.1113/jphysiol.2004.073353

Wardle, R. A., & Poo, M. (2003). Brain-derived neurotrophic factor modulation of GABAergic synapses by postsynaptic regulation of chloride transport. *The Journal of Neuroscience: The Official Journal of the Society for Neuroscience*, *23*(25), 8722–8732.

Watson, B. O., Levenstein, D., Greene, J. P., Gelinas, J. N., & Buzsáki, G. (2016). Network Homeostasis and State Dynamics of Neocortical Sleep. *Neuron*, *90*(4), 839–852. https://doi.org/10.1016/j.neuron.2016.03.036

Weaver, D. R. (1998). The Suprachiasmatic Nucleus: A 25-Year Retrospective. *Journal of Biological Rhythms*, *13*(2), 100–112. https://doi.org/10.1177/074873098128999952

Weiss, S. A. (2023). Chloride ion dysregulation in epileptogenic neuronal networks. *Neurobiology of Disease*, *177*, 106000. https://doi.org/10.1016/j.nbd.2023.106000

Welsh, D. K., Yoo, S.-H., Liu, A. C., Takahashi, J. S., & Kay, S. A. (2004). Bioluminescence Imaging of Individual Fibroblasts Reveals Persistent, Independently Phased Circadian Rhythms of Clock Gene Expression. *Current Biology*, *14*(24), 2289–2295. https://doi.org/10.1016/j.cub.2004.11.057

Woodin, M. A., Ganguly, K., & Poo, M. (2003). Coincident pre- and postsynaptic activity modifies GABAergic synapses by postsynaptic changes in Cl- transporter activity. *Neuron*, *39*(5), 807–820. https://doi.org/10.1016/s0896-6273(03)00507-5

Xia, H., Zhan, Y., Wang, L., & Wang, X. (2024). Exploring the interplay between circadian rhythms and prostate cancer: Insights into androgen receptor signaling and therapeutic opportunities. *Frontiers in Cell and Developmental Biology*, *12*, 1421204. https://doi.org/10.3389/fcell.2024.1421204

Yamada, J., Okabe, A., Toyoda, H., Kilb, W., Luhmann, H. J., & Fukuda, A. (2004). Cl- uptake promoting depolarizing GABA actions in immature rat neocortical neurones is mediated by NKCC1. *The Journal of Physiology*, *557*(Pt 3), 829–841. https://doi.org/10.1113/jphysiol.2004.062471

Yu, X., Franks, N. P., & Wisden, W. (2021). Brain Clocks, Sleep, and Mood. In O. Engmann & M. Brancaccio (Eds.), *Circadian Clock in Brain Health and Disease* (Vol. 1344, pp. 71–86). Springer International Publishing. https://doi.org/10.1007/978-3-030-81147-1_5

Zajac, M., Chakraborty, K., Saha, S., Mahadevan, V., Infield, D. T., Accardi, A., Qiu, Z., & Krishnan, Y. (2020). What biologists want from their chloride reporters – a conversation between chemists and biologists. *Journal of Cell Science*, *133*(2), jcs240390. https://doi.org/10.1242/jcs.240390

Zeng, A., & O'Neill, J. S. (2022). Using ALLIGATORs to Capture Circadian Bioluminescence. In G. Solanas & P.-S. Welz (Eds.), *Circadian Regulation* (Vol. 2482, pp. 125–135). Springer US. https://doi.org/10.1007/978-1-0716-2249-0_8

Zhang, J., Gao, G., Begum, G., Wang, J., Khanna, A. R., Shmukler, B. E., Daubner, G. M., de los Heros, P., Davies, P., Varghese, J., Bhuiyan, M. I. H., Duan, J., Zhang, J., Duran, D., Alper, S. L., Sun, D., Elledge, S. J., Alessi, D. R., & Kahle, K. T. (2016). Functional kinomics establishes a critical node of volume-sensitive cation-Cl− cotransporter regulation in the mammalian brain. *Scientific Reports*. https://doi.org/10.1038/srep35986

7. List of Publications

1) ***Giacomo Pasquini**, Tanja Kunej.* **A Map of the microRNA Regulatory Networks Identified by Experimentally Validated microRNA-Target Interactions in Five Domestic Animals: Cattle, Pig, Sheep, Dog, and Chicken.** OMICS: A Journal of Integrative Biology, 2019.

2) *Enrico Pracucci*, Robert Grahm*, Laura Alberio*, Gabriele Nardi*, Olga Cozzolino, Vinoshene Pillai,* ***Giacomo Pasquini**, Luciano Saieva, Darren Walsh, Silvia Landi, Jinwei Zhang, Andrew J. Trevelyan, Gian-Michele Ratto.* **Daily rhythm in cortical chloride homeostasis underpins functional changes in visual cortex excitability.** Nature Communications, 2023.

3) *Roberto Frau, Luca Concas, Giulia Braccagni, Francesco Traccis, Caterina Branca, Sara Salviati, Valeria Serra, Eleonora Corridori, Gabriele Nardi,* ***Giacomo Pasquini**, Silvia Landi, Michele Santoni, Paolo Follesa, Federico Brandalise, Monica Puligheddu, Miriam Melis, Gian Michele Ratto, Simona Scheggi, Marco Bortolato.* **Sleep deprivation impairs information processing via dysregulation of chloride homeostasis in the prefrontal cortex.** Submitted to BioRxiv and Nature Communications.

4) ***Giacomo Pasquini***, Melissa Santi*, Simone Giubbolini*, Andrew Beale, Marco Brondi, Irene Carrozzo, Alberto Egidi, Gabriele Nardi*, Erko Chala Beyene, Hanako Tsushima Semini, Marta Stancampiano, Anna Fassio, Silvia Landi, Claudia Lodovichi, Rachel Edgar, John O'Neill, Daniele Arosio, Gian Michele Ratto.* **A novel fluorescent sensor reveals mechanisms of cellular inhibition.** Under preparation.

*These authors contributed equally